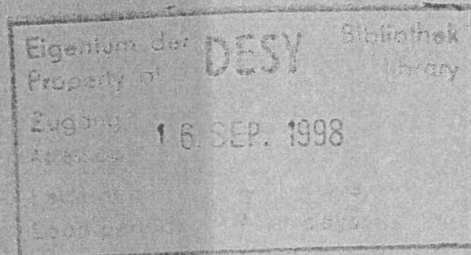# DEUTSCHES ELEKTRONEN-SYNCHROTRON

X1998-01399

Study of Exclusive Electroproduction of ρ^0 Mesons at Low Q^2 Using the ZEUS Beam Pipe Calorimeter at HERA

by

T. Monteiro

NOTKESTRASSE 85 - 22607 HAMBURG

Study of exclusive electroproduction of ρ^0 mesons at low Q^2 using the ZEUS Beam Pipe Calorimeter at HERA

by

Teresa Monteiro

Study of exclusive electroproduction of ρ^0 mesons at low Q^2 using the ZEUS Beam Pipe Calorimeter at HERA

Dissertation
zur Erlangung des Doktorgrades
des Fachbereichs Physik der
Universität Hamburg

vorgelegt von
Teresa Monteiro
aus Setúbal, Portugal

Hamburg
1998

Para a Ana e para o Josué.

Abstract

The reaction $ep \to e\rho^0 p(\rho^0 \to \pi^+\pi^-)$ is studied in the previously unexplored transition region of non-perturbative to perturbative QCD, for photon virtuality Q^2 between 0.25 and 0.85 GeV^2. The range covered in photon-proton center of mass energy W_{γ^*p} is between 20 and 90 GeV, and $|t| < 0.6$ GeV^2, where t is the squared four-momentum transfered at the proton vertex. For this study, an electromagnetic calorimeter covering positron scattering angles between 17 and 35 mrad was constructed and installed in the ZEUS detector at the HERA collider in 1995.

The $\pi^+\pi^-$ invariant mass distribution in the ρ^0 region is investigated. The differential cross section $d\sigma^{\gamma^*p \to \pi^+\pi^- p}/d|t|$ and its dependence on W_{γ^*p} (shrinkage) are studied. The spin density matrix elements are measured and the ratio of longitudinal to transverse cross section is extracted. The ρ^0 production cross section is determined as a function of W_{γ^*p} and Q^2. These results are found to be largely consistent with phenomenological models of soft hadronic interactions.

Zusammenfassung

Die Reaktion $ep \to e\rho^0 p(\rho^0 \to \pi^+\pi^-)$ wird in der vormals noch nicht erreichbaren Übergangsregion von der nicht-perturbativen zur perturbativen QCD bei Photonvirtualitäten Q^2 zwischen 0,25 und 0,85 GeV^2 untersucht. Die Schwerpunktsenergie des Photon-Proton-Systems W_{γ^*p} liegt zwischen 20 und 90 GeV und $|t| < 0,6$ GeV^2, wobei t das Betragsquadrat des am Protonvertex ausgetauschten Viererimpulses ist. Für diese Untersuchungen wurde 1995 im ZEUS-Detektor am HERA-Beschleuniger ein elektromagnetisches Kalorimeter installiert, das Positronstreuwinkel im Bereich zwischen 17 und 35 mrad erfaßt.

Die Verteilung der invarianten Masse des $\pi^+\pi^-$-Systems wird im Bereich der ρ^0 Masse untersucht. Der differentielle Wirkungsquerschnitt $d\sigma^{\gamma^*p \to \pi^+\pi^- p}/d|t|$ und seine Abhängigkeit von W_{γ^*p} wird studiert. Die Elemente der Spin-Dichte-Matrix werden gemessen, sowie das Verhältnis des longitudinalen zum transversalen Wirkungsquerschnitt. Der Wirkungsquerschnitt der ρ^0 Produktion wird als Funktion von W_{γ^*p} und Q^2 untersucht. Die Ergebnisse sind in guter Übereinstimmung mit phänomenologischen Modellen der weichen hadronischen Wechselwirkungen.

Contents

List of Figures

List of Tables

Chapter 1

Introduction

The first unambiguous evidence of existence of the ρ^0 meson (1961)[1] was obtained in bubble chamber experiments.

The ρ^0 is the lightest of the vector mesons, particles which share the interesting feature of carrying the same quantum numbers as the photon. This means that vector mesons, and the ρ^0 in particular, can couple directly to photons, and play an important role in γ-hadron collisions [2].

Through a series of successful phenomenological approaches, namely the vector meson dominance model and Regge theory, ρ^0 production in photon-hadron collisions has been shown to be intimately connected not only to inclusive γp scattering, but also to inclusive hadron-hadron processes. This is particularly interesting since $\gamma p \rightarrow \rho^0 p$ is one of the simplest processes that can be studied in photon-hadron interactions.

These phenomenological models, often referred to as 'soft models', have been able to describe an extensive list of results obtained in hadron-hadron collisions. In addition, they describe equally well the results of photon-hadron fixed target experiments at center of mass energies $W_{\gamma p}$ up to $W_{\gamma p} \sim 20$ GeV^2, in a range of photon virtuality Q^2 from photoproduction ($Q^2 = 0$) up to a few GeV. These results show cross sections that depend weakly on the center of mass energy and a steep exponential dependence of the differential cross section in t, where t is the squared four-momentum transfered at the hadronic vertex (the latter is similar to properties of optical diffraction).

During the late 80's the storage ring HERA, a unique facility which provides collisions between 820 GeV protons and 27.5 GeV electrons (or positrons) at a center of mass energy of 300 GeV, was constructed at DESY (*Deutsches Elektronen-Synchrotron*, Hamburg).

One of the many subjects that can be studied at HERA is the exclusive electroproduction of ρ^0 mesons, $ep \rightarrow e\rho^0 p$. The HERA lepton beam can be viewed as a source of interacting

---

[1] A brief historical review of vector mesons can be found in [9]

[2] Shortly before the discovery of the ρ^0, Sakurai had predicted the existence of such particles, in the context of the theory of photon-hadron interactions [88].

virtual photons, γ^*, in which case the reaction above can be directly related to that of $\gamma^* p \to \rho^0 p$. The advent of HERA has therefore allowed the study of photon-proton interactions in a new kinematic regime, spanning over a much wider range of $W_{\gamma^* p}$ and Q^2.

The photoproduction of light vector mesons at HERA has been studied in detail, and found to exhibit similar characteristics as the low energy results.

However, HERA has also been a rich source of data at high Q^2 values, providing stringent tests of Quantum Chromodynamics, QCD, the theory of strong interaction.

With increasing Q^2, where the partonic structure of the proton becomes relevant, the methods of perturbative QCD (pQCD) become applicable. Models based on pQCD, so-called 'hard models', predict a rise of the cross section with energy significantly stronger than that predicted by soft ones. In the hard models, the cross section for light vector meson production depends on the square of the gluon density in the proton, which was measured at HERA to rise at low x_{Bj} (where x_{Bj} is the fraction of the proton momentum carried by the struck parton). For a fixed Q^2 value, low x_{Bj} corresponds to high $W_{\gamma^* p}$, therefore these models predict a steep dependence of the cross section on the energy. Recent experimental results on light vector meson production at HERA indicate that in the deep inelastic scattering region (DIS, $Q^2 \gtrsim 4$ GeV^2) the predictions of soft models fail and that the cross section for these reactions becomes consistent with perturbative QCD calculations where the interaction is viewed as a colorless two gluon exchange.

ZEUS is a multipurpose detector for physics at HERA, taking data since June 1992. Its region of coverage in Q^2 has been recently extended by the installation of a small angle electromagnetic calorimeter, the Beam Pipe Calorimeter (BPC). The construction, running and calibration of the BPC are described in this thesis.

The BPC, which allows the study of ρ^0 production in the region $0.25 < Q^2 < 0.85$ GeV^2, can bring significant contributions to the understanding of the transition between the regime where soft models are successful to that where the calculations of pQCD can be applied.

This thesis reports on the study of ρ^0 production $ep \to e\rho^0 p(\rho^0 \to \pi^+\pi^-)$ at an intermediate range of photon virtuality between photoproduction and deep inelastic scattering, using the new ZEUS component, the BPC.

A large scale experiment like ZEUS is a collaborative effort, whose success requires contributions from many people. My main contributions during my time as a PhD. student in the ZEUS experiment have been: participation in the mechanical construction of the BPC; responsibility for the test of the BPC photomultiplier tubes and determination of the their operating high voltages; monitoring of the data quality of the ZEUS main calorimeter and its sub-components, including the BPC; maintenance of the BPC during the data taking period; responsibility for the determination of the online vertex-by-timing of ZEUS; responsibility for the implementation and maintenance of the BPC reconstruction software; development of the calibration techniques used in the BPC, and calibration of the detector in the 95 data taking period;and the analysis of ρ^0 production with the

BPC.

The organization of this thesis is as follows:

An overview of vector meson production, existing models for this process and their regions of applicability is given.

The ZEUS experiment is then introduced, covering in particular the new BPC used in the analysis. The reconstruction of the BPC data, its performance in a test beam and the calibration of the device are described. The kinematical reconstruction and the criteria used to select ρ^0 elastic events is presented in chapter 6 and efficiency corrections and background estimates are presented in chapter 7. In chapter 8 the sources of systematic uncertainties are discussed. In chapter 9 the results on the cross section measurements and dependencies on $M_{\pi\pi}$, t, $W_{\gamma^* p}$ and Q^2 and presented, and the ρ^0 angular decay distributions are discussed; finally, the conclusions of this study are given.

Chapter 2

Vector meson production in ep collisions at HERA

This chapter discusses the theory of the production of vector mesons in ep collisions at HERA. First, the relevant kinematical variables are introduced, and the general formulations of the inclusive ep process is presented. Then, the relationship between ep and $\gamma^* p$ cross sections, and the hadronic character of the photon are addressed. The production of vector mesons both in the photoproduction regime and at high virtuality of the photon are discussed, including a brief overview of the existing theoretical and phenomenological models for this process. Finally, the vector meson decay angular distributions, and the information they provide on the photon spin density matrix are discussed.

2.1 Kinematical variables

The scattering of positrons and protons can be described, to first order, by the exchange of a gauge boson: in neutral current interactions the intermediate boson is either a γ^* or a Z^0, while in charged current interactions it is a $W^\pm$, and the incoming positron is converted into a (anti-)neutrino. In the following only events with a positron in the final state, i.e. neutral current interactions, are considered; at the values of momentum transfer of this analysis these can be interpreted in terms of one-photon-exchange [1] (figure 2.1). It is conventional to describe the scattering of positrons on protons by the Mandelstam variable s, the ep center of mass energy squared:

$$s = (p+k)^2 \simeq 4E_e E_p, \tag{2.1}$$

where E_e and E_p are the electron and proton beam energies, and any pair of the following Lorentz scalars Q^2, y, $W_{\gamma^* p}$, x_{Bj} and ν:

- The virtuality (four-momentum squared) of the photon:

$$Q^2 = -q^2 = -(k-k')^2 \simeq 2E_e E_{e'}(1 + \cos\theta_{e'}), \tag{2.2}$$

---
[1]The effects of the charge of the incoming lepton for these events are negligible. Therefore the words electron and positron are used here without distinction.

where $E_{e'}$ is the energy of the outgoing electron, and $\theta_{e'}$ is the electron scattering angle, defined with respect to the direction of the proton beam.

- The relative energy transfer from the positron to the proton (in the proton rest frame):

$$y = \frac{p.q}{p.k} \simeq 1 - \frac{E_{e'}}{E_e}\frac{1 - \cos\theta_{e'}}{2}. \tag{2.3}$$

- The center-of-mass energy squared of the $\gamma^* p$ system:

$$W_{\gamma^* p}^2 = (q+p)^2 \simeq sy - Q^2. \tag{2.4}$$

- The x-Bjorken scaling variable:

$$x_{Bj} = \frac{Q^2}{2p.q} \simeq \frac{Q^2}{sy}, \tag{2.5}$$

which can be interpreted as the fraction of the proton four-momentum carried by the struck quark.

- The energy transfer from the positron to the proton (in the proton rest frame):

$$\nu = \frac{p.q}{m_p} \simeq \frac{Q^2}{2m_p x_{Bj}}. \tag{2.6}$$

In these expressions terms proportional to the proton and electron masses have been neglected, and the lepton and proton beams have been assumed to be collinear. In addition, the study of elastic ρ^0 production $ep \to e\rho^0 p(\rho^0 \to \pi^+\pi^-)$ requires the introduction of a few more variables:
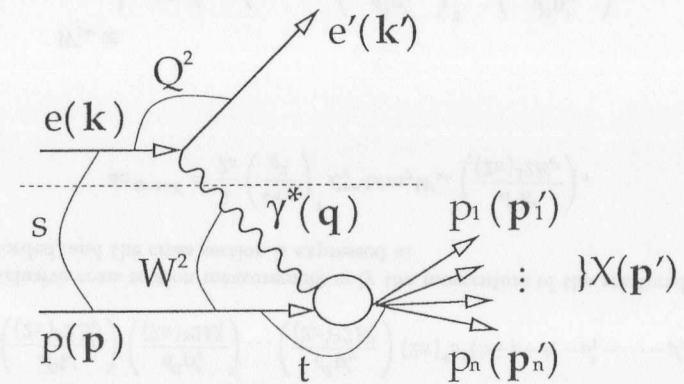
Figure 2.1: Kinematics of ep scattering: neutral current (γ^*) exchange. The ep collision can be seen as a $\gamma^* p$ collision (below dashed line), with the lepton beam emitting the photon.

- The Mandelstam variable t, the negative squared momentum transfer at the proton vertex :

$$t = (p - p')^2 \simeq (\mathbf{p_X}(\rho^0) + \mathbf{p_X}(e'))^2 + (\mathbf{p_Y}(\rho^0) + \mathbf{p_Y}(e'))^2 \qquad (2.7)$$

where p' is the momentum of the outgoing proton, and the subscripts X and Y denote the transverse components of the momenta with respect to the direction of the proton beam.

- The invariant mass of the two ρ^0 decay pions, $M_{\pi\pi}$.

- The angles describing the decay of the ρ^0 (described in detail in section 2.7).

2.2   The electron-proton cross section

Before addressing the production of vector meson in ep collisions, it is useful to discuss the inclusive ep cross section ($ep \to eX$), where all the accessible final states X and possible outgoing momenta are included [2].

The total ep cross section is defined as:

$$d\sigma^{ep \to eX} = \frac{|\mathcal{M}|^2 dQ}{F}, \qquad (2.8)$$

where $\mathcal{M}$ is the matrix element between initial and final state, containing the dynamical features of the process, dQ is the Lorentz invariant phase space available for the outgoing particles, and F is the incident flux.

For a collinear collision between particles A and B, the flux is given by

$$F = 4\sqrt{(p_A \cdot p_B)^2 - m_A^2 m_B^2}, \qquad (2.9)$$

which, in high energy collisions, reduces to $F \approx 2s$.

The matrix element for a particular final state X is

$$\langle |\mathcal{M}|^2 \rangle = \left(\frac{4\pi\alpha}{q^2}\right)^2 \mathcal{L}_e^{\mu\nu} \mathcal{K}_{\mu\nu}(X), \qquad (2.10)$$

where $\alpha = 1/137$ is the electromagnetic coupling constant, and the leptonic tensor

$$\mathcal{L}_e^{\mu\nu} = 2\{k^\mu k'^\nu + k^\nu k'^\mu - g^{\mu\nu}(k.k')\}, \qquad (2.11)$$

averaged over the spin of the incoming lepton and summed over the spin of the outgoing ones, describes the positron vertex, and $\mathcal{K}_{\mu\nu}$ is the unknown tensor describing the subprocess $\gamma^* p \to X$ at the hadronic vertex, which depends on $q = (k - k')$, on p and on the various outgoing momenta $p'_1, p'_2, ..., p'_n$

---

[2]Throughout this section the positron mass, which would appear in terms $\propto m_e/Q^2$, is neglected, since in the domain under study $m_e \ll Q^2$.

The phase space factor is

$$dQ = \left(\frac{d^3\mathbf{k}'}{(2\pi)^3 2E_{e'}}\right)\left(\frac{d^3\mathbf{p}'_1}{(2\pi)^3 2E'_1}\right) \cdots \left(\frac{d^3\mathbf{p}'_n}{(2\pi)^3 2E'_n}\right)(2\pi)^4 \delta^4(k+p-k'-p'_1-\cdots-p'_n). \qquad (2.12)$$

In an inclusive cross section measurement only the momentum of the scattered electron k' is recorded, and the cross section is expressed as

$$d\sigma^{ep \to eX} = \frac{1}{2s}\left(\frac{4\pi\alpha}{q^2}\right)^2 \mathcal{L}_e^{\mu\nu} 4\pi m_p W_{\mu\nu} \left(\frac{d^3\mathbf{k}'}{(2\pi)^3 2E_{e'}}\right), \qquad (2.13)$$

where

$$W_{\mu\nu} \equiv \qquad (2.14)$$

$$\frac{1}{4\pi m_p}\sum_X \int \cdots \int \mathcal{K}_{\mu\nu}(X)\left(\frac{d^3\mathbf{p}'_1}{(2\pi)^3 2E'_1}\right)^2 \cdots \left(\frac{d^3\mathbf{p}'_n}{(2\pi)^3 2E'_n}\right) \times$$
$$(2\pi)^4 \delta^4(k + p - k' - p'_1 - \cdots - p'_n).$$

$\sum_X$ denotes averaging over initial proton spin states as well as summing over final states. The tensor $W_{\mu\nu}$ can be rewriten in terms of the electromagnetic current j_μ:

$$W_{\mu\nu} = \qquad (2.15)$$
$$\frac{1}{4\pi m_p}\sum_X \langle X \mid j_\mu \mid p \rangle \langle p \mid j_\nu \mid X \rangle^* (2\pi)^4 \delta^4(k + p - k' - p'_1 - \cdots - p'_n).$$

Since $d^3\mathbf{k}' = |\mathbf{k}'|^2 d|\mathbf{k}'| d\Omega$ and $|\mathbf{k}'| = E_{e'}$, and $dy\, dQ^2 = (E_{e'}/\pi)dE_{e'}d\Omega$

$$\frac{d^2\sigma^{ep \to eX}}{dy\, dQ^2} = \frac{1}{2s}\left(\frac{4\pi\alpha}{q^2}\right)^2 \mathcal{L}_e^{\mu\nu} 4\pi m_p W_{\mu\nu} \frac{1}{4(2\pi)^2}. \qquad (2.16)$$

In the inelastic process $E_{e'}$ is not kinematically determined by E_e and $\theta_{e'}$, since the system of outgoing particles at the hadronic vertex are no longer constrained to have the mass of the proton.

$W_{\mu\nu}$ is a general second rank tensor, but its antisymmetric terms may be ignored since their contribution to the cross section vanishes due to $\mathcal{L}_e^{\mu\nu}$ being symmetric; the current conservation at the hadronic vertex requires $q^\mu W_{\mu\nu} = q^\nu W_{\mu\nu} = 0$, therefore $W_{\mu\nu}$ can be expressed in terms of two *structure functions*, W_1 and W_2, that depend on two independent scalars (Q^2 and y are a common choice):

$$W_{\mu\nu} = W_1\left(\frac{q_\mu q_\nu}{q^2} - g_{\mu\nu}\right) + \frac{W_2}{m_p^2}\left[p_\mu - \left(\frac{q.p}{q^2}\right)q_\mu\right]\left[p_\nu - \left(\frac{q.p}{q^2}\right)q_\nu\right]. \qquad (2.17)$$

Rewriting equation 2.16 using equations 2.11 and 2.17,

$$\frac{d^2\sigma^{ep \to eX}}{dy\,dQ^2} = \tag{2.18}$$

$$\frac{1}{2s}\frac{16\pi^2\alpha^2}{Q^4}4\pi m_p\left[2W_1Q^2 + W_2\frac{s^2}{m_p^2}\left(1 - y - \frac{x_{Bj}ym_p^2}{s}\right)\right]\frac{1}{4(2\pi)^2}$$

$$= \frac{4\pi\alpha^2}{Q^4}\left[yx_{Bj}F_1(y,Q^2) + \frac{1}{y}(1-y)F_2(y,Q^2)\right],$$

where the proton structure functions F_1 and F_2

$$F_1(y,Q^2) = m_pW_1(y,Q^2), \tag{2.19}$$

$$F_2(y,Q^2) = \nu W_2(y,Q^2), \tag{2.20}$$

have been introduced; once again the lepton mass was neglected, and, in the last expression, terms proportional to m_p/s were also ignored.

2.3   The virtual photon-proton cross section

Although HERA provides collisions between electrons and protons, most studies at HERA can be reduced to the understanding of what happens in the lower vertex of figure 2.1, when a (virtual) photon interacts with the proton. In fact, the ep and γ^*p cross sections can be directly related, and HERA data can be used to study photon-proton interactions, with the role of the lepton beam being simply to provide the interacting photon.

In the scattering of a real photon, with (transverse) polarization ε and an unpolarized proton target, the photon energy (in the proton rest frame) is given by $\nu \equiv K =| \mathbf{K} |$, with $q = (\nu, \mathbf{K})$. This cross section can therefore be written as:

$$\sigma_i^{\gamma p \to X} = \frac{4\pi^2\alpha}{K}\varepsilon_i^{\mu*}\varepsilon_i^{\nu}W_{\mu\nu}, \tag{2.21}$$

where ε_i is the polarization vector of the photon with helicity i. The invariant mass of the final state is

$$W_{\gamma p}^2 = (p + q)^2 = m_p^2 + 2m_pK. \tag{2.22}$$

With real photons, the two transverse polarizations of the incident photons have to be summed. To extend this cross section to virtual photons, the fact that the polarization states are not limited to two has to be considered, since they can also have a longitudinal component. The polarization vectors of virtual photons, taking $\mathbf{K}$ along the Z-axis , are:

Transverse polarization: $\varepsilon_{\pm 1} = \frac{1}{\sqrt{2}}(0, 1, \pm i, 0)$ (2.23)

Longitudinal polarization: $\varepsilon_0 = \frac{1}{Q^2}\left(\sqrt{\nu^2 + Q^2}, 0, 0, \nu\right).$ (2.24)

In addition, the flux of virtual photons is not a uniquely defined concept, contrary to the case of real particles where it was given by $4m_pK$. A conventional choice is to require the momentum K of the virtual photon to be equal to the energy of a real photon needed to give the same center-of-mass energy, i.e. to continue to satisfy equation 2.22. This is known as the Hand convention [58]:

$$K_{Hand} = \frac{-Q^2 + 2m_p\nu}{2m_p} = \nu\left(1 - x_{Bj}\right). \tag{2.25}$$

In the limit $q^2 \to 0$ this expression reduces to $K_{Hand} = \nu$, as it should for real photons. (other approach to the flux of virtual photons can be found in [48].)

Using equation 2.17 together with the polarization vectors 2.23 and 2.24, the transverse and longitudinal cross section are, respectively,

$$\sigma_T^{\gamma^*p \to X} = \frac{1}{2}\left(\sigma_{-1}^{\gamma^*p \to X} + \sigma_{+1}^{\gamma^*p \to X}\right) = \frac{4\pi^2\alpha}{K_{Hand}}W_1(\nu,Q^2), \tag{2.26}$$

$$\sigma_L^{\gamma^*p \to X} = \sigma_0^{\gamma^*p \to X} = \frac{4\pi^2\alpha}{K_{Hand}}\left[\left(1 + \frac{\nu^2}{Q^2}\right)W_2(\nu,Q^2) - W_1(\nu,Q^2)\right] \tag{2.27}$$

Typically, in γ^*p scattering at small Q^2, x_{Bj} is small and $K_{Hand} \approx \nu$. Also $1 + \nu/(Q)^2 \approx \nu/Q^2$, yielding

$$\sigma_T^{\gamma^*p \to X} = \frac{4\pi^2\alpha}{\nu}W_1(\nu,Q^2) = \frac{4\pi^2\alpha}{m_p\nu}F_1(\nu,Q^2), \tag{2.28}$$

$$\sigma_L^{\gamma^*p \to X} = \frac{4\pi^2\alpha}{\nu}\left(\frac{\nu^2}{Q^2}W_2(\nu,Q^2) - W_1(\nu,Q^2)\right) = \frac{4\pi^2\alpha}{Q^2}F_2(\nu,Q^2) - \frac{4\pi^2\alpha}{m_p\nu}F_1(\nu,Q^2). \tag{2.29}$$

where the structure functions from 2.19 were used. Inverting these relations, and inserting them in equation 2.18 yields:

$$\frac{d^2\sigma^{ep \to eX}}{dy\,dQ^2} = \frac{\alpha}{2\pi}\frac{1}{Q^2}\frac{1 + (1-y)^2}{y}\left[\sigma_T^{\gamma^*p \to X}(y,Q^2) + \frac{2(1-y)}{1 + (1-y)^2}\sigma_L^{\gamma^*p \to X}(y,Q^2)\right] \tag{2.30}$$

which is known as the Equivalent Photon Expression (EPE).

By the same arguments, also elastic ρ^0 production at HERA can be expressed in terms of the process $\gamma^*p \to \rho^0p$:

$$\frac{d^2\sigma^{ep \to e\rho^0p}}{dy\,dQ^2} = \frac{\alpha}{2\pi}\frac{1}{Q^2}\frac{1 + (1-y)^2}{y}\left[\sigma_T^{\gamma^*p \to \rho^0p}(y,Q^2) + \frac{2(1-y)}{1 + (1-y)^2}\sigma_L^{\gamma^*p \to \rho^0p}(y,Q^2)\right] \tag{2.31}$$

2.4   The hadronic character of the photon

Equation 2.31 above relates the $ep \to e\rho^0p$ cross section to the $\gamma^*p \to \rho^0p$ cross section. The latter reaction in real photoproduction has been extensively studied at fixed target

experiments and is usually interpreted in terms of the hadronic character of the photon [3].

The results of photoproduction experiments revealed a number of similarities between photon-hadron interactions and hadron-hadron ones, namely a weak energy dependency of the cross section above ~ 3 GeV (see figure 2.2), secondary particles with limited transverse momenta ('soft' interactions), and an imaginary forward amplitude [68, 80].

In the phenomenological interpretation of this data the photon is regarded as being a kind of hadron part of the time; in this picture, the features of photon-hadron interactions should be similar to those of hadron hadron interactions, except that the cross sections are smaller than the hadronic ones by approximately the magnitude of the fine structure constant (an old rule-of-thumb says that one can estimate photon cross sections crudely by multiplying the corresponding pion cross section by α/π [102]).

Intuitively, this can be understood by noticing that the photon propagating in free space can, according to Heisenberg's uncertainty principle, fluctuate into a virtual hadronic state which has the same quantum numbers as the photon. The photon is always making transitions back and forth between a bare photon, and a hadron, and the interaction with the proton can be regarded as trapping the photon in its hadronic state.

If the hadron into which the photon fluctuates is a a vector meson of mass M_V, the time allowed for this fluctuation is of the order of

$$t_f \approx \frac{2K}{Q^2 + M_V^2},\tag{2.32}$$

in the proton rest frame, with the photon four-momentum $q = (\nu, \mathbf{K})$ and $K = |\mathbf{K}|$; in the case of a real photon, the previous expression is simply $2K/M_V^2$.

If during this time t_f the virtual particle can travel a distance much larger than the nucleon size (~ 1 fm), i.e. if its Q^2 and the vector meson mass are small enough, the resulting interaction may look like a hadronic one.

The models based in the above picture ('soft models') will be described in the next section. In perturbative QCD based models of γ^*p interactions a very similar picture holds. The photon couples to a $q\bar{q}$ pair and the interaction can be seen as trapping the photon in this $q\bar{q}$ state. The predictions of perturbative QCD models are, however, very different from the soft models with regard to the cross section behavior, and will be discussed in section 2.6.

2.5   Soft models for vector mesons production

Like inclusive photoproduction, also the elastic photoproduction of light vector mesons (VM) $\gamma p \rightarrow VMp$ follows the main features of hadronic interactions (compare figures 2.2 and 2.6) with a slow rise of the cross section with energy, and an exponential falloff of the differential cross section which is large at $t = 0$ (forward peak) and decreases rapidly with t, $d\sigma/d|t| \propto e^{-b|t|}$. These characteristics, long known at low center-of-mass energies (see [9] for a review on measurements previous to 1978, [114] for an extensive

---

[3]The symbol γ^* is used below referring generically to photons, both real and virtual. Whenever only real photons apply, the symbol γ is used.

list of references), have also been observed in photoproduction of light vector mesons at HERA [106, 53, 107, 109, 114] and can be described by the models below.

2.5.1   Vector meson Dominance Model (VDM)

The Vector meson Dominance Model (VDM) [9, 70] is a model based on the ideas outlined in section 2.4. It attempts to explain the features of photon-hadron interactions by describing the photon $|\gamma^*\rangle$ as a superposition of two states: a bare photon $|\gamma_B^*\rangle$ and a small hadronic component $\sqrt{\alpha}\,|h\rangle$:

$$|\gamma^*\rangle = \sqrt{(Z_3)}\,|\gamma_B^*\rangle + \sqrt{\alpha}\,|h\rangle\tag{2.33}$$

where Z_3 is a normalization factor. The probability of finding the photon in the hadronic state is small, but large hadron-hadron cross sections make the hadronic component dominant at low Q^2. Since $|h\rangle$ should have the same quantum numbers as the photon ($J^{PC} = 1^{--}; Q = S = B = 0$), and the vector mesons ρ^0, ω and ϕ, which meet this requirement, are copiously produced in photoproduction, it is plausible that these VM supply very important contributions to the cross section. The Vector meson Dominance Model is based on the hypothesis that these three vector mesons are the only hadronic constituents of the photon, and that the bare photon component does not participate in hadronic interactions. According to this model:
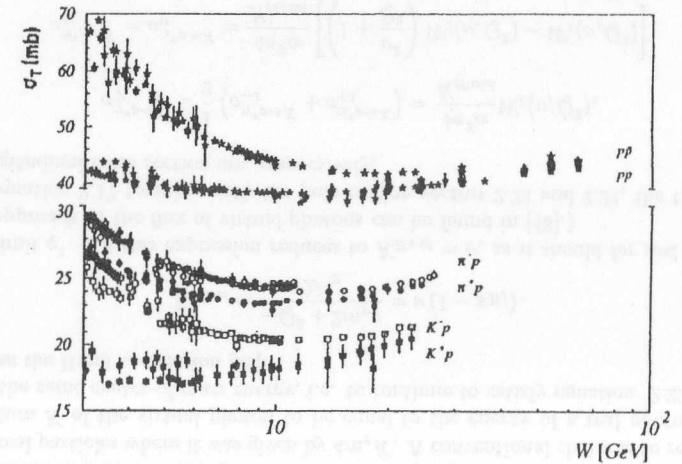
Figure 2.2: Hadron-hadron cross sections from [51].

$$\sqrt{\alpha} \mid h\rangle = \sum_{V=\rho,\omega,\phi} \frac{1}{f_V} \frac{M_V^2}{M_V^2 + Q^2} \mid V\rangle \tag{2.34}$$

where the coupling constants f_V can be determined, for example, from e^+e^- collisions [4], and can be found in [80].

VDM is based on Sakurai's theory of strong interactions mediated by vector fields, and the formulation of Sakurai [89] is closely followed in this section.

According to VDM, expression 2.34 relates the electromagnetic matrix element for $\gamma^* p \to X$, $\langle X \mid j_\mu \mid p\rangle$ of equation 2.15, to the corresponding matrix element for $Vp \to X$, $\langle X \mid J_\mu^V \mid p\rangle$ via

$$\langle X \mid j_\mu \mid p\rangle = \frac{1}{1 + \frac{M_V^2}{Q^2}} \frac{1}{f_V} \langle X \mid J_\mu^V \mid p\rangle \tag{2.35}$$

where J_μ^V stands for the current density of the vector meson field.

Both j and J^V can be separated into components perpendicular ($\perp$) and parallel ($\parallel$) to the virtual photon/vector meson three-momentum. The transverse and longitudinal cross sections of photons and vector mesons are then represented as

$$\sigma_T^{\gamma^* p \to X} = \frac{4\pi^2\alpha}{K} \sum_X \mid \langle X \mid j_\perp \mid p\rangle \mid^2 \frac{1}{4\pi m_p}(2\pi)^4 \delta^4(p+q-p') \tag{2.36}$$

$$\sigma_L^{\gamma^* p \to X} = \frac{4\pi^2\alpha}{K} \frac{Q^2}{\nu^2} \sum_X \mid \langle X \mid j_\parallel \mid p\rangle \mid^2 \frac{1}{4\pi m_p}(2\pi)^4 \delta^4(p+q-p') \tag{2.37}$$

$$\sigma_T^{Vp \to X} = \frac{\pi}{K} \sum_X \mid \langle X \mid J_\perp^V \mid p\rangle \mid^2 \frac{1}{4\pi m_p}(2\pi)^4 \delta^4(p+q-p') \tag{2.38}$$

$$\sigma_L^{Vp \to X} = \frac{\pi}{K} \frac{M_V^2}{\nu^2} \sum_X \mid \langle X \mid J_\parallel^V \mid p\rangle \mid^2 \frac{1}{4\pi m_p}(2\pi)^4 \delta^4(p+q-p') \tag{2.39}$$

VDM makes the hypothesis that $\sum_X \mid \langle X \mid J_{\perp,\parallel}^V \mid p\rangle \mid^2$ varies very little with Q^2. Therefore, using the previous expressions, the Q^2 dependence of the $\gamma^* p$ cross section in the VDM model can be explicitly written as

$$\sigma_T^{\gamma^* p \to X}(W_{\gamma^* p}, Q^2) = \sum_{V=\rho,\omega,\phi} \frac{4\pi\alpha}{f_V^2} \left(\frac{1}{1+\frac{Q^2}{M_V^2}}\right)^2 \sigma_T^{Vp \to X}(W_{\gamma^* p}), \tag{2.40}$$

and

$$\sigma_L^{\gamma^* p \to X}(W_{\gamma^* p}, Q^2) \doteq \sum_{V=\rho,\omega,\phi} \frac{4\pi\alpha}{f_V^2} \left(\frac{1}{1+\frac{Q^2}{M_V^2}}\right)^2 \frac{Q^2}{M_V^2} \xi_V \sigma_T^{Vp \to X}(W_{\gamma^* p}) \tag{2.41}$$

ξ_V is the ratio of the longitudinal to the transverse $Vp \to X$ cross section and it is $\mathcal{O}(1)$.

---

[4]In the reaction $e^+e^- \to \gamma^* \to V \to hadrons$ the partial width of the resonance is related to f_V by $\Gamma = (\alpha^2/3)(4\pi/f_V^2)M_V$.

The extension of this model to include other states than ρ^0, ω and ϕ in $\mid h\rangle$ is known as the Generalized Vector meson Dominance Model (GVD) [32].

For exclusive ρ^0 production $\gamma^* p \to \rho^0 p$, formulae 2.40 and 2.41 reduce (assuming no off-diagonal terms) to

$$\sigma_T^{\gamma^* p \to \rho^0 p}(W_{\gamma^* p}, Q^2) = \frac{4\pi\alpha}{f_\rho^2} \left(\frac{1}{1+\frac{Q^2}{M_\rho^2}}\right)^2 \sigma_T^{\rho^0 p \to \rho^0 p}(W_{\gamma^* p}), \tag{2.42}$$

and

$$\sigma_L^{\gamma^* p \to \rho^0 p}(W_{\gamma^* p}, Q^2) = \frac{4\pi\alpha}{f_\rho^2} \left(\frac{1}{1+\frac{Q^2}{M_\rho^2}}\right)^2 \frac{Q^2}{M_\rho^2} \xi_\rho \sigma_T^{\rho^0 p \to \rho^0 p}(W_{\gamma^* p}) \tag{2.43}$$

In this model $R(Q^2) = \sigma_L^{\gamma^* p \to \rho^0 p}/\sigma_T^{\gamma^* p \to \rho^0 p} = Q^2/M_\rho^2 \xi_\rho$, where ξ_ρ can be determined experimentally either through the Q^2 dependence of $\sigma_T^{\gamma^* p \to \rho^0 p} + \sigma_L^{\gamma^* p \to \rho^0 p}$, or through an helicity analysis of ρ^0 production.

2.5.2   Regge Phenomenology

Regge phenomenology, which attempts to describe the asymptotic behavior of strong interactions, was developed in the context of hadron-hadron interactions, but due to the analogy presented above, it applies equally to photon-hadron collisions and in particular to elastic ρ^0 production.

Theorems on the total cross section

Before presenting Regge's phenomenological model, three theorems must be introduced:

- The optical theorem:

  The optical theorem (see e.g. [81]) relates the total cross section for a process $AB \to X$ to the imaginary part of the forward elastic scattering amplitude:

$$\sigma^{AB \to X}(s) = \frac{1}{s} Im(\mathcal{A}(s, t=0)) \tag{2.44}$$

  with the elastic scattering amplitude $\mathcal{A}$ normalized to

$$\frac{d\sigma^{AB \to AB}}{d|t|} = \frac{1}{16\pi s^2} \mid \mathcal{A}(s, t) \mid^2 . \tag{2.45}$$

  s is the square of the center of mass energy of the relevant process (in $\gamma^* p$ collisions $s \equiv W_{\gamma^* p}^2$, note different definition of s compared to previous section).

- Pomeranchuk's theorem:

  Pomeranchuk's theorem is a prediction from quantum field theory [62] that is supported by the data:

$$\sigma_{s \to \infty}^{AB \to X}(s) = \sigma_{s \to \infty}^{\bar{A}B \to X}(s). \tag{2.46}$$

Moreover, this theorem states that the cross section at high energies should also become isospin independent.

• Froissart bound:

The Froissart bound (see e.g. [23]) states that

$$\sigma_{s \to \infty}^{AB \to X}(s) \leq \frac{1}{m_\pi^2} \ln^2(s). \tag{2.47}$$

i.e. as s tends to infinity, the total cross section can grow at most as $ln^2(s)$. At the energies presently available, this limit is still far from being saturated.

The Regge model describes hadronic interactions in terms of particles exchanged in the t-channel [23] (see figure 2.3). For the process $AB \to CD$, s is the square of the center of mass energy, and t is related to the scattering angle. However, particle exchange proceeds through the t-channel $A\bar{C} \to \bar{B}D$ and in this case t gives the energy and s gives the t-channel scattering angle θ_t (the roles of s and t are interchanged). Crossing relations tell us that the s and t-channel processes have a common scattering amplitude, with t and s in different domains (see figure 2.4).

The scattering amplitude $\mathcal{A}$ can be decomposed into a t-channel partial wave series

$$\mathcal{A}(s,t) = \sum_{l=0}^{\infty} (2l+1) \mathcal{A}_l(t) P_l(\cos \theta_t) \tag{2.48}$$
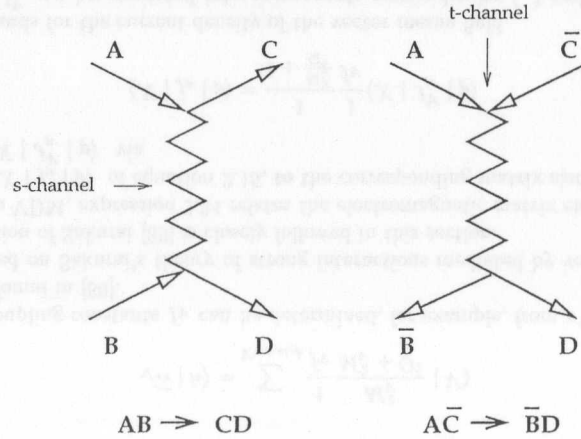
Figure 2.3: s-channel and t-channel picture.

where P_l are the Legendre polynomials, and each amplitude $\mathcal{A}_l$ is identified with a 'propagator' term for an exchanged particle of angular momentum l and mass m_l, with all the suitable quantum numbers:

$$\mathcal{A}_l(t) = \frac{\Gamma(t)}{t - m_l^2}, \tag{2.49}$$

where $\Gamma(t)$ is the decay width of the particle of mass m_l. Extending the scattering amplitude to the complex l plane, using Cauchy's theorem, and noting that even and odd contributions to expression 2.48 are separated due to parity conservation in strong interactions, $\mathcal{A}$ can be rewritten as

$$\mathcal{A}(s,t) = \frac{1}{2i} \int dl (2l+1) \frac{\Gamma_l(t)}{t - m_l^2} \frac{e^{i\pi l} + \mathcal{S}}{2 \sin \pi l} P_l(\cos \theta_t). \tag{2.50}$$

The signature $\mathcal{S} = \pm 1$ for even/odd angular momentum states.
The Chew-Frautschi plots (spin versus mass m_l^2, see figure 2.5) show that particles and resonances of a given isospin and strangeness (and even/odd angular momentum) align along a trajectory $l = \alpha(m_l^2)$, which relates angular momentum and mass, and can be expanded around t

$$\alpha(t) \simeq \alpha(m_l^2) + \frac{d\alpha(t)}{dt}(t - m_l^2) = l + \alpha'(t - m_l^2), \tag{2.51}$$
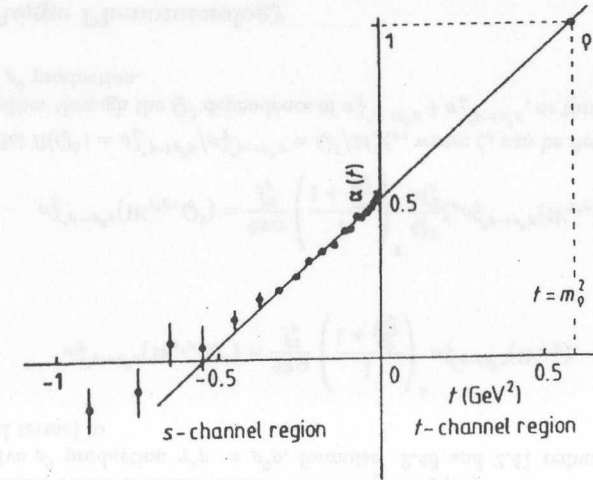
Figure 2.4: The ρ^0 trajectory, and the values of $\alpha(t)$ $(t < 0)$ obtained in $\pi^- p \to \pi^+ n$, from [23].
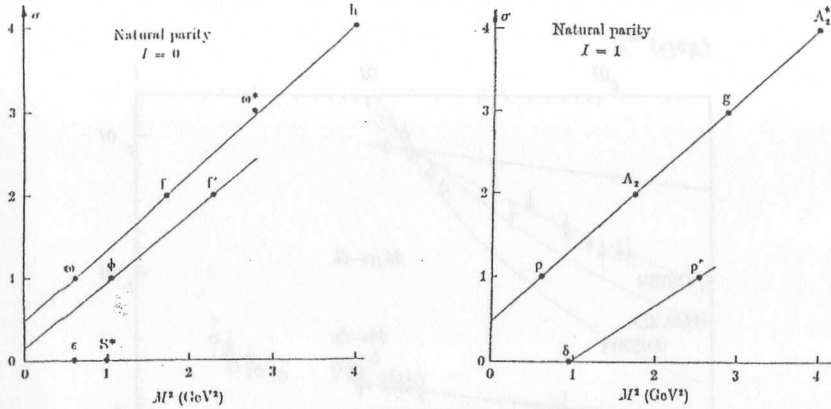
Figure 2.5: Chew-Frautschi plot of meson Regge trajectories, from [23].

where α' denotes the slope of the function $\alpha(t)$. Replacing $t - m_l^2$ by $\frac{1}{\alpha'}(\alpha(t) - l)$ and using Cauchy's theorem at the pole $\alpha(t) = l$,

$$\mathcal{A}(s,t) = -\pi \frac{e^{i\pi\alpha(t)} + \mathcal{S}}{2\sin\pi\alpha(t)}(2\alpha(t)+1)\Gamma_l(t)\alpha' P_l(\cos\theta_t) \tag{2.52}$$

Considering that

$$P_{l_{s\to\infty}}(\cos\theta_t) \simeq e^{-i\pi\alpha(t)}(\cos\theta_t)^{\alpha(t)}, \tag{2.53}$$

and that for elastic scattering of particles A and B

$$\cos\theta_t = 1 + \frac{2st}{(t-m_A^2-m_B^2)^2 - 4m_B^2 t} \stackrel{s\to\infty}{=} s \tag{2.54}$$

one concludes:

$$\rho \equiv \frac{Re(\mathcal{A})}{Im(\mathcal{A})} \stackrel{s\to\infty}{=} -\frac{\cos\pi\alpha + \mathcal{S}}{\sin\pi\alpha}, \tag{2.55}$$

and

$$\mathcal{A}(s,t) \stackrel{s\to\infty}{=} \beta(t)\left(\frac{s}{s_0}\right)^{\alpha(t)}, \tag{2.56}$$

where s_0 is a constant. Using the last expression and the optical theorem 2.44, the energy dependence of total cross section is found to be

$$\sigma^{AB\to X} \propto s^{\alpha(0)-1}. \tag{2.57}$$

In addition, rewriting equation 2.51 as

$$\alpha(t) = \alpha(0) + \alpha' t, \tag{2.58}$$

and using expressions 2.45 and 2.56, the Regge prediction for the elastic differential cross section can be inferred:

$$\frac{d\sigma^{AB\to AB}}{d|t|} = \beta(t)^2\left(\frac{s}{s_0}\right)^{2(\alpha(t)-1)} = \beta(t)^2\left(\frac{s}{s_0}\right)^{2(\alpha(0)-1)} e^{2\alpha' t \ln s/s_0} \tag{2.59}$$

If the observed exponential dependence of the cross section in t referred in the beginning section 2.5 is introduced, $\beta(t)^2 \propto e^{-b_0|t|}$,

$$\frac{d\sigma^{AB\to AB}}{d|t|} = \left(\frac{s}{s_0}\right)^{2(\alpha(0)-1)} e^{-b_0|t|-2\alpha'|t|\ln(s/s_0)} = \left(\frac{s}{s_0}\right)^{2(\alpha(0)-1)} e^{-b(s)|t|}, \tag{2.60}$$

with $b(s) = b_0 + 2\alpha' \ln(s/s_0)$. This last expression is an important prediction of Regge theory, the shrinkage (or sharpening) of the forward t peak as the logarithm of the energy increases.

Integrating the differential cross section $d\sigma^{AB\to AB}/d|t|$ over t, the energy dependence for an elastic process yields

$$\sigma^{AB\to AB} \propto \frac{s^{2(\alpha(0)-1)}}{b(s)} \tag{2.61}$$

Since in the framework on the VDM model the energy (and t) dependence of the reaction $\gamma^* p \to \rho^0 p$ is directly given by the dependence of the elastic hadronic interaction $\rho^0 p \to \rho^0 p$ (see equations 2.42 and 2.43), the predictions of expressions 2.60 and 2.61 also hold in the case of exclusive ρ^0 production.

Donnachie and Landshoff parameterizations

According to the previous discussion, the high energy behavior of the total hadronic cross section is fixed by the Regge trajectory with the highest intercept $\alpha(0)$ in the Chew-Frautschi plots, which has $\alpha_\rho(0) = 0.44$ [81] (see figure 2.5). Therefore, the Regge model expects $\sigma^{AB\to X} \propto s^{-\frac{1}{2}}$. This is in conflict with the observations of a slow rise of the total hadron-hadron (and photon-hadron) cross section with energy (see figures 2.2 and 2.6). To solve this discrepancy, a hypothetical exchanged particle, the Pomeron $\mathbb{P}$, was introduced. This 'object' has the quantum numbers of the vacuum, and the intercept of its trajectory at $t = 0$ is $\alpha_{\mathbb{P}}(0) > 1$.

A possible QCD picture of the Pomeron is that it represents multiple gluon exchange.

A multitude of total hadron-hadron reactions can be successfully fitted by a sum of effective pure Regge exchange (sometimes referred as Reggeon) and Pomeron exchange:

$$\sigma^{hh\to X} = As^\epsilon + Bs^{-\eta} \tag{2.62}$$

where A and B are, respectively, the Pomeron and Reggeon contributions. Donnachie and Landshoff [35] have determined the parameters ϵ and η to be

$$\epsilon = 0.0808(\alpha_{\mathbb{P}(0)} = 1.0808) \text{ and } \eta = 0.4525(\alpha_\rho(0) = 0.5475).$$

More recently Cudell et al. performed a more complete fit [26], the best estimate yielding $\epsilon = 0.096^{+0.012}_{-0.009}$, but with good results for values of ϵ in the range [0.07,0.11]. A Pomeron which leads to values of ϵ in this range is also known as the 'soft' Pomeron. Donnachie and Landshoff have also fitted the t dependence of pp and $\bar{p}p$ cross sections according to 2.60, and obtained $\alpha'_{\mathbb{P}} = 0.25 \text{ GeV}^{-2}$ [33].

It should be noted that the energy behavior of the cross sections described by the Pomeron cannot prevail at increasingly higher energies, due to partial wave unitarity (Froissart bound of 2.47). So, eventually, at high enough energies, multi-Pomeron exchange will dominate, and the superposition of such higher order effects will prevent the violation of this limit.

It is also interesting that the dominance of Pomeron exchange at high energies leads to
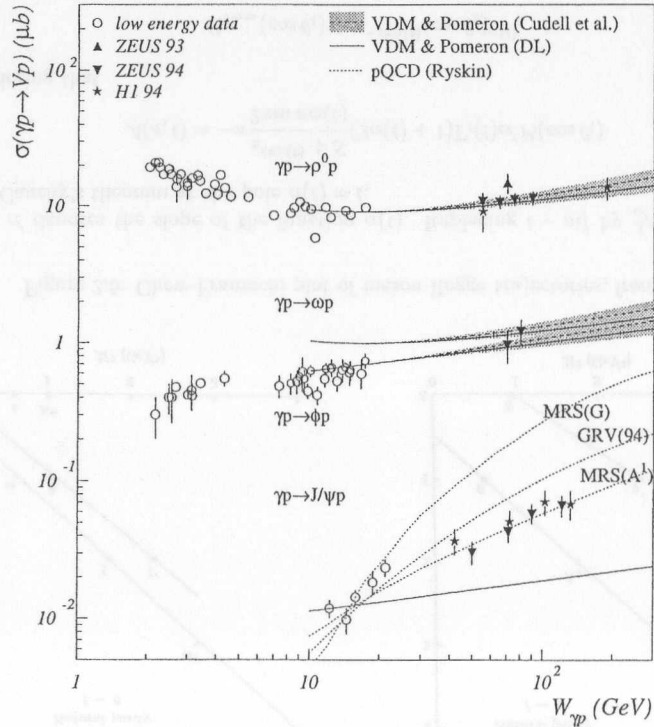
the behavior of cross sections consistent with Pomeranchuk's theorem 2.46.

As in the case of the Regge theory, the features of the Pomeron exchange should also apply to vector meson production. Figure 2.6 shows vector meson photoproduction measurements compared to the predictions of Donnachie and Landshoff, and Cudell et al. . The light vector mesons (ρ^0, ω and ϕ) exhibit the features predicted by the soft Pomeron over a wide range of energies.

However, J/Ψ photoproduction at HERA [52, 104, 55, 110], shows a much steeper dependence of the cross section on the energy, indicating that the Regge picture described above does not apply to this process. In addition, there are hints [105, 54, 108, 112, 56, 57] that, in the high Q^2 regime, the rise of the cross section with $W_{\gamma^* p}$ for light vector mesons is inconsistent with the prediction made by models based on the soft Pomeron exchange. The understanding of these processes requires different approaches such as perturbative QCD[5], discussed in the next section.

2.6 Perturbative QCD models for vector meson production

In order for a process to be calculable via perturbative QCD (pQCD) the value of the running coupling constant α_S must be small. This means the process has to contain a scale (in Deep Inelastic Scattering (DIS) the scale is usually taken to be Q^2) which is large enough so that $\alpha_S(Q^2) \ll 1$. In leading order,

$$\alpha_S(Q^2) = \frac{12\pi}{(33 - 2n_f) \ln(Q^2/\Lambda^2)} \quad (2.63)$$

where Λ is a confinement scale, not predicted by the theory, but expected to be somewhere in the range 0.1-0.5 GeV, and n_f is the number of flavors. Setting $\Lambda = 0.2$ GeV, and $n_f = 3$, one obtains $\alpha_s(0.25 \text{ GeV}) \simeq 3$, $\alpha_s(1 \text{ GeV}) \simeq 0.4$ and $\alpha_s(10 \text{ GeV}) \simeq 0.2$ (in the last case Q^2 is above the charm threshold, and $n_f = 4$)

It is therefore reasonable to expect that, at high enough Q^2, pQCD based models may describe $\gamma^* p \to \rho^0 p$.

Most of these models separate the photon-proton interaction into three stages in time:

- The photon oscillates into a $q\bar{q}$ pair.

- The $q\bar{q}$ pair interacts with the proton. The colorless exchange that takes place is treated as a perturbative two gluon, or gluon ladder exchange.

- The $q\bar{q}$ pair combines into a vector meson.

In general, the pQCD calculations predict only the longitudinal part of the cross section, which is expected to dominate in their region of applicability.

Figure 2.6: Cross section for vector meson photoproduction in fixed target experiments and at HERA [99].

---

[5]Also some non-perturbative QCD inspired models try to predict the properties of vector meson production at high Q^2. A list of such models can be found in [24].

The longitudinal differential vector meson production cross section at $t = 0$ given by one of the models presented below (Brodsky et al.),

$$\frac{d\sigma_L^{\gamma^* p \to V p}}{dt}\bigg|_{t=0} = \frac{A}{Q^6}\alpha_S^2(Q^2)\left|\left(1 + \frac{i\pi}{2}\frac{d}{d\ln x_{Bj}}\right)xg(x_{Bj}, Q^2)\right|^2, \qquad (2.64)$$

where A is a constant that depends on the vector meson wave function, helps to illustrate the main predictions shared by pQCD models:

- The cross section is related to the square of the gluon density in the proton xg.

- The $W_{\gamma^* p}$ dependence of the longitudinal cross section is
  $\sigma^{\gamma^* p \to V p}(W_{\gamma^* p}) \propto [\alpha_S(Q^2)xg(x_{Bj}, Q^2)]^2 \simeq W_{\gamma^* p}$
  but depends somewhat upon the x_{Bj} range covered.

- The Q^2 dependence of the longitudinal cross section is $(Q^2)^{-3}$, modified by $[\alpha_S(Q^2)xg(x_{Bj}, Q^2)]^2$, leading to an effective power $(Q^2)^n$ with $n \simeq 2 - 2.5$ which depends slightly on the x_{Bj} range.

- The t and $W_{\gamma^* p}$ dependences of the cross section are decoupled, so no shrinkage is expected. In addition, the transverse size of the $q\bar{q}$ system is assumed to be small, so that the t dependence of the cross section is mainly determined by the proton size, $d\sigma/d|t| \propto e^{-b|t|}$ with $b \simeq 5$ GeV^2 for all vector mesons.

- The ratios of the vector meson production cross sections are given by the charges of the constituent quarks, assuming flavor independent production mechanisms, for example $\sigma(\phi)/\sigma(\rho^0) = 2/9$ (consistent with high Q^2 data [108, 57]).

Some of the pQCD models are briefly presented below. HERA data will hopefully soon provide means of discriminating among them.

2.6.1   Ryskin et al.

Just before HERA started data-taking, Ryskin suggested that the hard scale needed for perturbative calculations of exclusive production of J/Ψ could be supplied by the mass of this heavy vector meson, regardless of the Q^2 of the interaction. This model [86], which uses a leading-log $1/x_{Bj}$ approximation (LLA($1/x_{Bj}$)), predicts a rise in the cross section with the square of the strong coupling constant times the square of the gluon density, evaluated at the effective values of Q^2 and x_{Bj} of:

$$\bar{q}^2 = \frac{M_V + Q^2}{4} \qquad (2.65)$$

$$x_{Bj}^- = \frac{M_V + Q^2}{W^2} \qquad (2.66)$$

It has successfully described the diffractive photoproduction of J/Ψ at HERA [52, 104, 55, 110], which shows an energy dependence of the cross section much steeper than expected from a soft process (see figure 2.6). However, once extended to light vector mesons, even at moderate Q^2, the scale $\bar{q}^2$ in the Ryskin model is still significantly lower than that of other models described below.

2.6.2   Brodsky et al.

The perturbative model introduced by Brodsky et al [16] expresses the forward differential cross section of leptoproduction of vector mesons in terms of the light-cone $q\bar{q}$ wave function of the vector meson and the gluon distribution of the proton. The double-leading-log approximation (DLLA) is used. The model is valid for the production of light vector mesons, provided that the kinematic region satisfy the conditions $W^2/M_V^2 \gg 1$, $W^2/Q^2 \gg 1$ and $|t| \ll Q^2$. Its results are equivalent to those of the Ryskin model when a simple non-relativistic pair of quarks is assumed for the vector meson.

2.6.3   Frankfurt et al.

Frankfurt et al. [44] have made similar calculations to Brodsky et al. , but used a LLA(Q^2) approximation, including contributions by the sea quarks of the nucleon. The authors discuss the predictions of pQCD, quantifying their kinematical limits of validity, the production of excited states of vector mesons and the restoration of flavor symmetry. In addition, the model reveals the important role of quark Fermi motion within the vector meson.

2.6.4   Martin et al.

The models presented above make only perturbative calculations of VM production by longitudinal photons. Martin et al. [73] have addressed the behavior of σ_T, and the relative contribution of longitudinal and transverse component to the total cross section versus Q^2 based on the open production of light $q\bar{q}$ pairs and parton-hadron duality. Again, the predictions are made in terms of gluon densities and account for the observed deviations of $R(Q^2) = \sigma_L^{\gamma^* p \to \rho^0 p}/\sigma_T^{\gamma^* p \to \rho^0 p}$ from linearity at high Q^2.

2.6.5   Bartels et al., Forshaw et al.

The works of Bartels et al. [8] and Forshaw et al. [42] discuss the the possibility of the hard scale required for pQCD calculations being supplied by the momentum transfer t at the proton vertex. Recent studies at high t at HERA [111] are consistent with this hypothesis.

2.7   Vector meson decay angular distributions

ρ^0 production allows the study of the polarization of the vector meson, which can be inferred from the angular distributions of the decay into two pions [22].

The definition of the decay angles depends on the choice of reference system. Three reference systems, which differ in the choice of the spin-quantization axis (Z-axis) commonly used [9] are shown in figure 2.7; depending on the production mechanism, the ρ^0 may be aligned with one of these systems, in which case the angular distribution description is simplified: In the following the *helicity system* is used. This system, where the Z-axis is opposite to the direction of the recoil proton in the overall $\gamma^* p$ center of mass frame,

is convenient in case of *s-channel helicity conservation* (SCHC, i.e. the vector meson retains the helicity of the photon: helicity zero mesons are produced only by longitudinally polarized photons, and helicity one mesons by transversely polarized photons). The Y-axis is given by the normal to the production plane defined by the cross product of the three-momenta of the ρ^0 and of the virtual photon. This system is adopted as there are experimental evidences of SCHC in ρ^0 production [7, 64, 19].

Other choices of reference frames include the *Adair system*, where the Z-axis is along the direction of the incident photon in the overall $\gamma^* p$ center of mass frame, convenient in case of *spin independence* in the s-channel system, and the *Gottfried-Jackson system*, where the Z-axis is the direction of the incident photon in the ρ^0 rest frame, convenient in case of *t-channel helicity conservation*.

Once the reference frame has been chosen, the decays can be characterized using three planes, as in figure 2.8:

- The *scattering plane*, defined by the scattered lepton and the virtual photon.

- The *production plane*, defined by the photon and the vector meson momenta.

- The *decay plane*, defined by the decay particles (pions, in the case of ρ^0).

with the decay angles θ_h, ϕ_h and Φ_h being:

- θ_h, the polar angle of the π^+ in the ρ^0 rest frame;

- ϕ_h, the azimuthal angle of the π^+ in the ρ^0 rest frame (it coincides with the angle between the ρ^0 production and the decay planes);

- Φ_h, the angle between the production plane and the scattering plane.
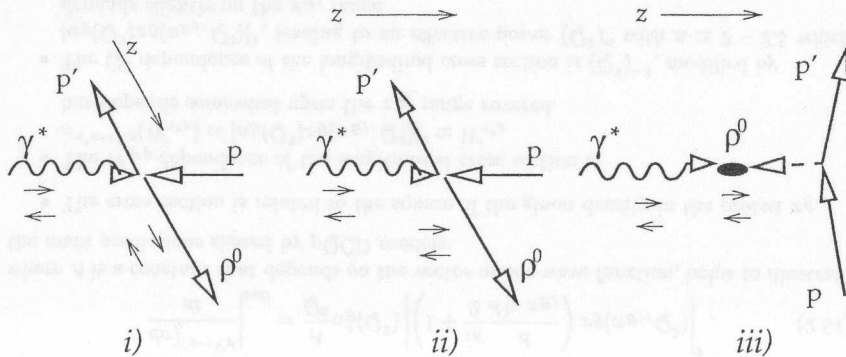
Figure 2.7: Schematic diagram indicating the preferred reference frames for the study of the ρ^0 decay angles depending on the process: *i)* Helicity system: helicity conservation; *ii)* Adair system: conservation of spin direction; *iii)* Gottfried-Jackson system: no spin transfer in the t-channel (dashed line showing t-channel exchange). Adapted from [9].

In certain cases it is also of use to define the polarization angle $\Psi_h = \phi_h - \Phi_h$.

Using the formalism of [90], and assuming that the incoming proton is unpolarized and that its final state polarization is not detected the normalized three-dimensional angular distribution can be expressed as a function of 15 independent elements

$$
\begin{aligned}
W^{unpol}(\cos\theta_h, \phi_h, \Phi_h) = \qquad\qquad (2.67)\\
\frac{3}{4\pi}\Big[\frac{1}{2}(1 - r_{00}^{04}) + \frac{1}{2}(3r_{00}^{04} - 1)\cos^2\theta_h - \sqrt{2}Re(r_{00}^{04})\sin 2\theta_h \cos\phi_h - \\
r_{1-1}^{04}\sin^2\theta_h \cos 2\phi_h - \varepsilon\cos 2\Phi_h\{r_{11}^1\sin^2\theta_h + r_{00}^1\cos^2\theta_h - \\
\sqrt{2}Re(r_{10}^1)\sin 2\theta_h \cos\phi_h - r_{1-1}^1\sin^2\theta_h \cos 2\phi_h\} - \\
\varepsilon\sin 2\Phi_h\{\sqrt{2}Im(r_{10}^2)\sin 2\theta_h \sin\phi_h + Im(r_{1-1}^2)\sin^2\theta_h \sin 2\phi_h\} + \\
\sqrt{2\varepsilon(1+\varepsilon)}\cos\Phi_h\{r_{11}^5\sin^2\theta_h + r_{00}^5\cos^2\theta_h - \\
\sqrt{2}Re(r_{10}^5)\sin 2\theta_h \cos\phi_h - r_{1-1}^5\sin^2\theta_h \cos 2\phi_h\} + \\
\sqrt{2\varepsilon(1+\varepsilon)}\sin\Phi_h\{\sqrt{2}Im(r_{10}^6)\sin 2\theta_h \sin\phi_h + Im(r_{1-1}^6)\sin^2\theta_h \sin 2\phi_h\}\Big]
\end{aligned}
$$

where ε is given by (see [58, 48])

$$
\varepsilon = \frac{2(1-y)}{(1 + (1-y)^2)} \qquad\qquad (2.68)
$$
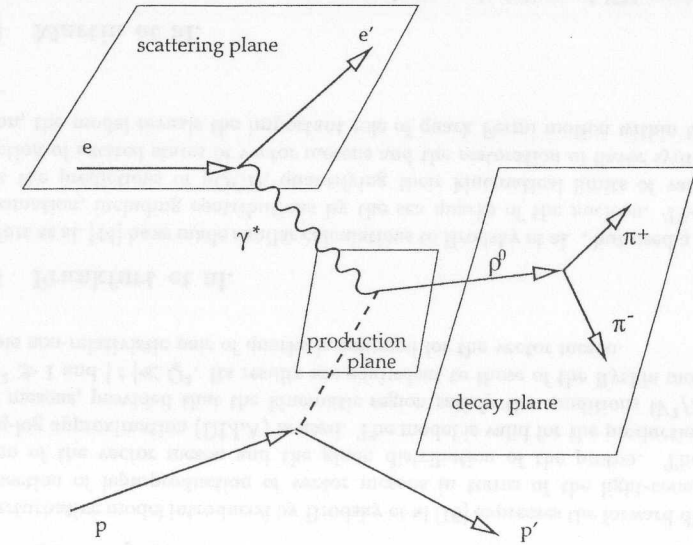
Figure 2.8: Schematic diagram of the planes that define the angles θ_h, ϕ_h and Φ_h used in the analysis of the ρ^0 decay angular distributions (helicity frame).

and $\varepsilon > 0.995$ in this analysis [6]

The quantities r_{mn}^i, r_{mn}^{04} are linear combinations of the vector meson spin density matrix elements $\rho(V)_{mn}^i$ (i=0,1,2,4,5,6):

$$r_{mn}^{04} = \frac{\rho_{mn}^0 + \varepsilon R \rho_{mn}^4}{1 + \varepsilon R}, \tag{2.69}$$

$$r_{mn}^i = \frac{\rho_{mn}^i}{1 + \varepsilon R} \quad i = 1, 2, \tag{2.70}$$

$$r_{mn}^i = \frac{\sqrt{R} \rho_{mn}^i}{1 + \varepsilon R} \quad i = 5, 6, \tag{2.71}$$

where R is the ratio of the elastic ρ^0 production cross section for longitudinal photons to that for transverse photons (see below); the subscripts m and n run over the possible helicity states -1, 0 and +1. The superscript 0 represents the unpolarized part, 1 and 2 describe transverse photons with linear polarization. The superscript 4 represents the longitudinal contribution, and 5 and 6 refer to interference terms between transverse and longitudinal polarizations. Since R is not known, the contributions from the matrix elements ρ_{mn}^0 and ρ_{mn}^4 can not be separated unless measurements at different ε, i.e. at different scattering angle for fixed Q^2 and W_{γ^*p} are performed.

In case of SCHC, most elements in equation 2.67 reduce to zero. The only non-vanishing ones in this case are r_{00}^{04}, r_{1-1}^1, $Im(r_{1-1}^2)$, $Re(r_{10}^5)$ and $Im(r_{10}^6)$, and, furthermore, these elements are related to each other:

$$r_{1-1}^1 = -Im(r_{1-1}^2), \tag{2.72}$$

$$Re(r_{10}^5) = -Im(r_{10}^6), \tag{2.73}$$

simplifying equation 2.67 to

$$W^{unpol}(\cos\theta_h, \Psi_h) = \tag{2.74}$$
$$\frac{3}{4\pi}[\frac{1}{2}(1 - r_{00}^{04}) + \frac{1}{2}(3r_{00}^{04} - 1)\cos^2\theta_h \varepsilon r_{1-1}^1 \sin^2\theta_h \cos 2\Psi_h -$$
$$2\sqrt{\varepsilon(1+\varepsilon)} Re(r_{10}^5) \sin 2\theta_h \cos\Psi_h]$$

If, in addition, the reaction proceeds via t-channel exchange of particle (or particles) with pure natural parity $(P = (-1)^J)$, a new relation holds:

$$r_{1-1}^1 = \frac{1}{2}(1 - r_{00}^{04}) \tag{2.75}$$

and one can rewrite the angular distribution as

---

[6]The additional terms to equation 2.67 arising from transverse polarization of the electron beam contain both a factor m_e/Q^2 and a factor $(1 - \varepsilon)$, and can safely be neglected in this study.

$$W^{unpol}(\cos\theta_h, \Psi_h) = \tag{2.76}$$
$$\frac{3}{8\pi}\frac{1}{1 + \varepsilon R}[\sin^2\theta_h(1 + \varepsilon\cos 2\Psi_h) + 2\varepsilon R\cos^2\theta_h -$$
$$\sqrt{2R\varepsilon(1+\varepsilon)}\cos\delta\sin 2\theta_h\cos\Psi_h]$$

where the parameter δ is the relative phase between the longitudinal and transverse amplitudes ($\cos\delta = -\sqrt{(8)}\frac{1+\varepsilon R}{\sqrt{R}}Re(r_{10}^5)$), and the value of R, the ratio of the elastic ρ^0 production cross section for longitudinal photons to that for transverse photons is given by

$$R = \frac{\sigma_L^{\gamma^*p \to \rho^0 p}}{\sigma_T^{\gamma^*p \to \rho^0 p}} = \frac{r_{00}^{04}}{\varepsilon(1 - r_{00}^{04})}. \tag{2.77}$$

(The last expression is valid under SCHC, independent of the parity of the exchange.)

2.8　Classification of the γ^*p sub-processes

Finally, it is useful to classify the sub-processes of the γ^*p interaction according to their final state (see figure 2.9):

- Diffractive processes

  Diffractive interactions [45, 46] are those where the scattering of the particles is peripheral, and there is no quantum number exchange involved. In analogy with optics (therefore the name diffraction), the diffractive scattering of the particles can, in a naive model, be approximated by the absorption of a quantum mechanical wave by a black disk, where the cross section depends only on the impact parameter (the distance between the particles orthogonally to the collision plane).

  In diffractive interactions, only a small amount of energy or momentum is exchanged, so the final particles continue to move with momenta close to those of the initial ones. This causes the rapidity [7] distribution of the final state particles to be grouped in two regions, corresponding to the incoming particles; this is used to experimentally identify diffractive events (events with a *rapidity gap*). Diffractive events can be either elastic or dissociative:

  - elastic diffraction

    It is customary to call the process $\gamma^*p \to Vp$ elastic (or exclusive) scattering [8].

    Naively one could think of elastic Compton scattering $\gamma^*p \to \gamma p$ as the photon-hadron counterpart of elastic hadron-hadron scattering. But, while the Compton process comprises a small fraction of the total γ^*p cross section, the elastic

---

[7]The rapidity y is defined as $y = 1/2\ln[(E + p_L)/(E - p_L)]$ where E is the energy of the particle and p_L its longitudinal momentum.

[8]Some authors prefer the name *Quasi-elastic*.

part of the cross section in hadron-hadron collisions accounts, typically, for $\sim 20\%$ of the total cross section. However, VM production in photon-hadron interactions can be considered an elastic process in the VDM model framework (described in section 2.5.1), and its contribution to $\sigma^{\gamma p \to X}$ is of the same magnitude of $(\sigma^{hh \to hh})/(\sigma^{hh \to X})$ in hadronic collisions.

— diffractive dissociation

Inelastic or dissociative scattering occurs when either the proton or the photon (or both) are allowed to break up into final states of higher mass but retaining the same quantum numbers as the incoming particles:

* proton dissociation: $\gamma^* p \to V N$
* photon dissociation: $\gamma^* p \to X p$
* double dissociation: $\gamma^* p \to X N$

• Non-diffractive
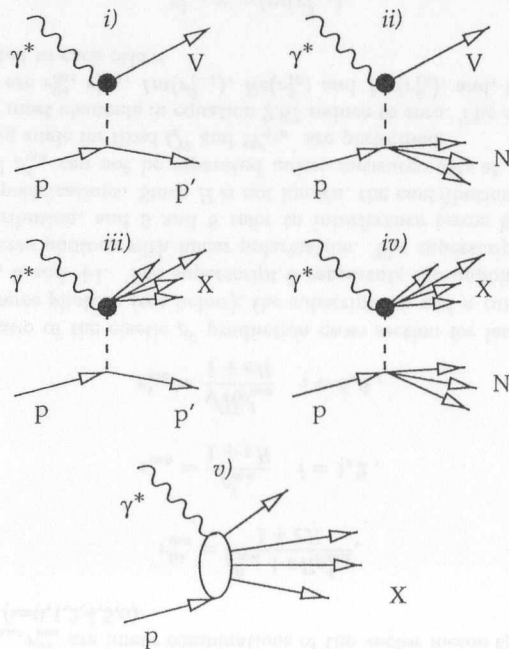
Figure 2.9: $\gamma^* p$ sub-processes: *i)* elastic (or exclusive) diffraction; *ii)* proton dissociative diffraction; *iii)* photon dissociative diffraction; *iv)* double dissociative diffraction; *v)* non-diffractive process.

The remaining interactions are called non-diffractive. The final state particles are distributed without large rapidity gaps.

Chapter 3

The HERA collider and the ZEUS detector

In this chapter the HERA collider and the ZEUS detector are described. These have been extensively described elsewhere [101, 103], therefore only characteristics or components relevant for the present analysis will be addressed in some detail.

3.1 The HERA collider

The **H**adron **E**lektron **R**ing **A**nlage **HERA** was constructed at DESY (*Deutsches Elektronen-Synchrotron*, Hamburg) during the late 80's. It is a unique facility, consisting of two storage rings of 6.3 km of circumference, 10-30 m underground and providing collisions between 820 GeV protons and 27.5 GeV electrons[1] (center of mass energy: ~ 300 GeV), probing electron and quark substructure to distances down to a few 10^{-18} cm, not accessible by fixed target experiments.

Since 1992, the HERA beams have been colliding head-on in two interaction regions occupied by the ZEUS and H1 experiments.

In addition, two fixed target experiments, HERMES and HERA-B, profit from the HERA beams.

HERMES, operating since 1995, studies the spin structure of nucleons by scattering longitudinally polarized electrons in polarized gas targets. Spin rotators, installed before and after the HERMES experimental hall, rotate the natural transverse polarization of the electron beam [94].

HERA-B (under installation) will use wire targets on the halo of the proton beam to produce B mesons and study $\mathcal{CP}$ violation in the $B^0 \bar{B}^0$ system.

The acceleration of the beams up to full energies is done in several steps (see figure 3.1). The injection of electrons begins in a 450 MeV linear accelerator (LINAC); these then fill the storage ring PIA, from which they are transfered, as a single bunch, into DESY II, where they are accelerated to 7 GeV. Each bunch is then injected into PETRA, until 70

---

[1]Since 1994 HERA operates with positrons instead of electrons. This has improved the lifetime of the lepton beam, allowing HERA to deliver higher luminosities [30]. In 1998 HERA will resume the operation with electrons. In the following the term electron is generically used for electrons and/or positrons.
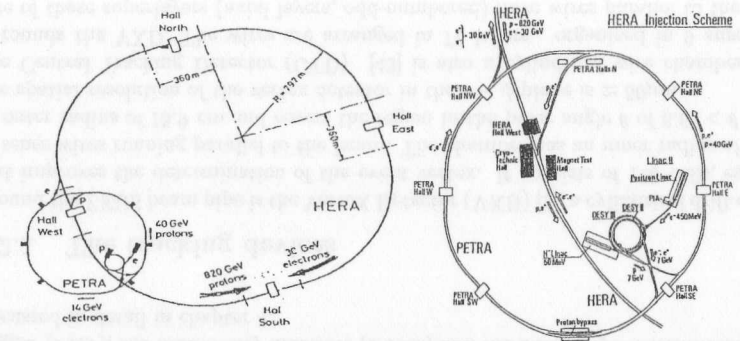
Figure 3.1: The HERA accelerator and its pre-accelerator complex.

Parameter	Design Values		Typical value in 1995	
	e^+	p	e^+	p
Energy	30 GeV	820 GeV	27.5 GeV	820 GeV
Center of mass energy	314 GeV		300 GeV	
Current	58 mA	160 mA	30 mA	55 mA
Injection energy	14 GeV	40 GeV	12 GeV	40 GeV
Injection time	15 min	20 min	45 min	60 min
Number of bunches	210		174+15	174+6
Bunch crossing time	96 ns			
Horizontal beam size at IP	0.30 mm	0.27 mm	0.24 mm	0.19 mm
Vertical beam size at IP	0.06 mm	0.09 mm	0.06 mm	0.06 mm
Longitudinal beam size at IP	0.8 cm	11 cm	0.8 cm	11 cm
Specific luminosity	$3.9 \cdot 10^{29}$ cm^{-2} s^{-1} A^{-2}		$5.0 \cdot 10^{29}$ cm^{-2} s^{-1} A^{-2}	
Instantaneous luminosity	$1.7 \cdot 10^{31}$ cm^{-2} s^{-1}		$4.3 \cdot 10^{30}$ cm^{-2} s^{-1}	
Integrated luminosity	35 pb^{-1}/year		12.5 pb^{-1}/year	
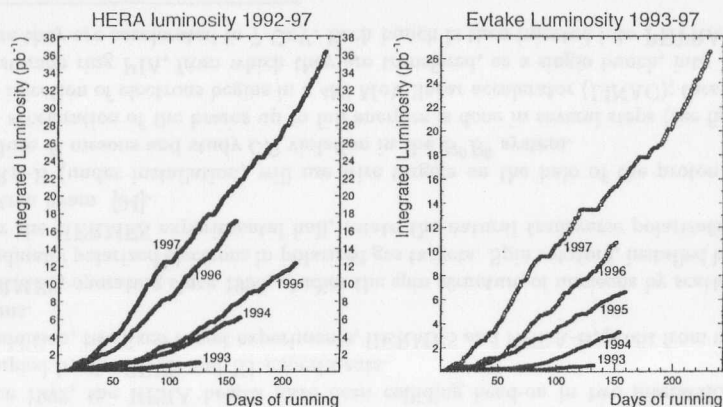
Figure 3.2: The integrated luminosity *i)* delivered by HERA and *ii)* collected by the ZEUS detector in the period 1993 to 1997.

bunches are accumulated and accelerated to 14 GeV. HERA is filled at this energy, with a total of 210 bunches (nominal values). The acceleration of protons starts with H^- ions accelerated up to 50 MeV in a LINAC These ions are then stripped, and injected into the storage ring DESY III. Here the protons, in bunches already spaced by 96 ns, are accelerated to 7 GeV. As for the positrons, the protons are injected into PETRA until 70 bunches are accumulated, and then accelerated to 40 GeV for injection to HERA.

The HERA running conditions in 1995 are summarized in table 3.1. While the limitations on the electron beam energy arise from the power dissipated by synchrotron radiation, the maximum proton beam energy is determined by the bending field of the dipole magnets. Figure 3.2 shows the integrated luminosity *i)* delivered by HERA and *ii)* collected by the ZEUS detector in the period 1993 to 1997, clearly showing a performance improvement every year.

3.2   Overview of the ZEUS experiment

The ZEUS collaboration, which includes over 400 physicists from a dozen countries, built and runs a powerful and versatile detector at HERA, which has been taking data since June 1992.

As in many high-energy physics experiments, the ZEUS detector uses mainly two complementary approaches to analyze the particles resulting from *ep* collisions: surrounding the interaction point, the tracking detectors trace the charged particles as they bend in a magnetic field; then, an outer layer of calorimeters, covering nearly the entire solid angle, determine the energy of charged and neutral particles by stopping them and measuring the total energy deposited in the material. Several smaller components of the ZEUS
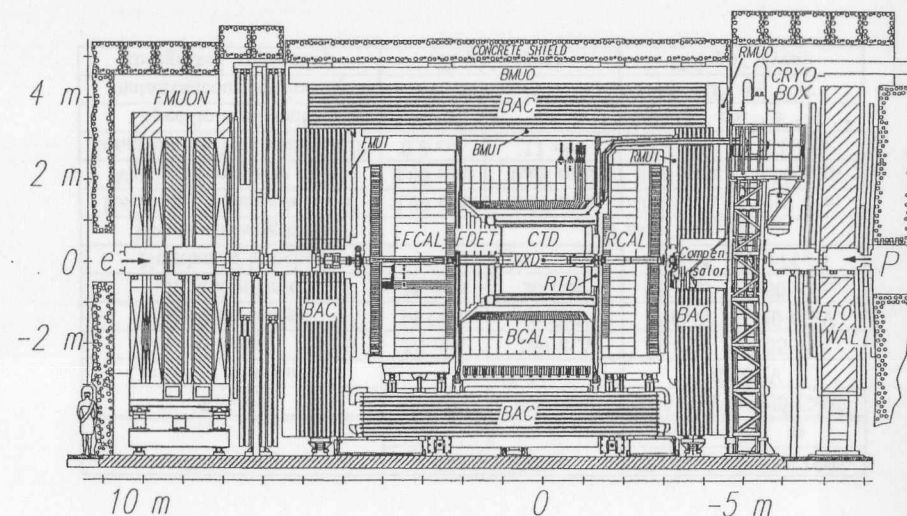
Figure 3.3: CAD drawing of ZEUS detector in ($X - Z$ projection).

detector help in the characterization of the events.

The components of the ZEUS detector which are important for this analysis are the tracking devices (the VerteX Detector VXD, the Central Tracking Detector CTD and the Rear Tracking detectors RTD), the uranium CALorimeter (CAL), the Proton Remnant Tagger (PRT), the Luminosity monitors (LUMI) and the Beam Pipe Calorimeter (BPC), discussed in detail in chapter 4.

3.2.1   The tracking devices

Around the ZEUS beam pipe is the VerteX Detector (VXD) [2], a cylindrical drift chamber that improves the determination of the event vertex. It consists of 120 cells, each with 12 sense wires running parallel to the beam. The chamber has an inner radius of 9.9 cm, an outer radius of 15.9 cm and covers the region in the polar angle θ of $8.6° < \theta < 165°$. The spatial resolution of the vertex detector in the $r - \phi$ plane is $\simeq 50\mu m$.

The Central Tracking Detector (CTD) [43] is also a cylindrical wire chamber, which surrounds the VXD. The wires are arranged in 72 layers , organized in 9 *superlayers*. Five of these superlayers (axial layers, odd-numbered) have wires parallel to the Z-axis, while the other four (stereo) superlayers are tilted by a small angle ($\simeq 5°$) whose value is chosen such that the resolution in polar and azimuthal angle is almost equal. In total, the CTD is equipped with 4608 sense wires, readout by flash analogue to digital converters (FADC). The wires of the axial superlayers 1, 3 and 5 are instrumented with Z-by-timing electronics, which determine the Z vertex coordinate by measuring the time of arrival of the pulses at the two ends of each wire. This information is used in the trigger. The CTD

measures more than $2\ m$ in length, and its origin is shifted by 25 cm towards the forward region with respect to the ZEUS nominal interaction point covering the angular range $15° < \theta < 164°$; it has a radius of about 80 cm. The CTD achieves a spatial resolution in $r - \phi$ of 190 μm, and of about 1 mm in Z (3 cm by Z-by timing) . The large solenoidal magnetic field around these inner tracking detectors provide precise transverse momentum measurements, reaching, for full length tracks, $\sigma(p_T)/p_T \simeq 0.005 p_T \oplus 0.016$ (where p_T is in GeV).

The Rear Tracking Detector (RTD) [14] is a planar drift chamber, located at the rear end of the CTD and extending the ZEUS inner tracking system. It consists of three layers of drift cells, perpendicular to the beam axis, each having six sense wires. The layers are mounted such that the wires have orientations $0°$, $60°$ and $-60°$ with respect to the horizontal. The RTD covers the polar region $160° < \theta < 170°$.

3.2.2   The uranium-scintillator calorimeter

The main calorimeter of the ZEUS detector [4], is a high resolution sampling calorimeter, built of alternating layers of depleted uranium plates (3.3 mm thick) and plastic scintillator (2.6 mm thick). The readout is performed via wavelength shifter bars and photomultiplier tubes.

This uranium CALorimeter (CAL) surrounds the inner tracking detectors and consists of three separate structures (forward, barrel and rear calorimeters) which, together, cover 99.6% of solid angle around the interaction point. The uranium/scintillator ratio was tuned so that it has equal response to electrons and hadrons (compensating calorimeter). The Forward CALorimeter (FCAL), in the proton direction, covers the range $2.5° < \theta < 36.7°$ (pseudorapidity [2] region $4.3 > \eta > 1.1$); the Barrel CALorimeter (BCAL) surrounds the central detector region, $36.7° < \theta < 129.1°$ (pseudorapidity region $1.1 > \eta > -0.75$); the Rear CALorimeter (RCAL), in the electron direction, covers the angular region $129.1° < \theta < 176.5°$ (pseudorapidity region $-0.75 > \eta > -3.8$) - small overlaps in the angular region covered were neglected.

Each of these calorimeters consists of modules (24 for FCAL and RCAL, 32 for BCAL), which are subdivided transversely into towers and longitudinally into one electromagnetic section (EMC) and one (in RCAL) or two (in FCAL and BCAL) hadronic sections (HAC). The ratio of electromagnetic energy (deposited in EMC) to hadronic energy (deposited in HAC) provides a means of separation between electrons and hadrons.

Each EMC section has a depth of 25 radiation lengths, usually enough to contain electromagnetic showers, or 1 interaction length, and is divided into sequential cells per tower. The HAC sections, with a total of 3 (RCAL) or 5 (FCAL and BCAL) interaction lengths, correspond to a single cell per tower.

The energy resolution of the calorimeter amounts to $\sigma(E)/E = 0.18(0.35)/\sqrt{(E)}$ (E in GeV) for electromagnetic (hadronic) particles.

Each calorimeter cell (there are a total of 5918 cells) is read out by two photomultiplier tubes, one for each side. While the energy sharing between different cells allows position reconstruction in one dimension, the position inside each cell is estimated by the double

[2]The pseudorapidity η is defined as $\eta = -\log[\tan(\theta/2)]$.

sided readout (in addition, if one photomultiplier tube, or a readout channel, fails, not all information on that cell is lost). The overall position resolution in the CAL is close to 1 cm.

The timing resolution is better than a nanosecond for energy deposits greater than 4 GeV. The CAL is calibrated daily to an accuracy of 1% using pedestal triggers, charge and light injection, as well as the signal arising from the uranium radioactivity.

3.2.3   The PRT

The Proton Remnant Tagger (PRT) [28] consists of 7 pairs of scintillator counters surrounding the beampipe, in the forward region, which detect particles scattered at very small angles, predominantly associated with the remnant of the proton. 2 pairs of counters (PRT1) are located at $Z = 5$ m and 5 pairs (PRT2) at $Z = 24$ m, tagging particles in the angular range $6 < \theta < 26$ mrad and $1.5 < \theta < 8$ mrad, respectively. In this analysis, only PRT2 is used, due to a small overlap between the PRT1 and the BPC operation in 1995. Each PRT2 counter consists of a 20 cm × 25 cm scintillator tile, of 10 mm thickness, attached to light guides and a photomultiplier tube. The counters in a pair are of equal shape and are placed one after the other, to cover the same area, in the proton beam direction. Each pair of counters is shielded on the outside by 4 mm lead, and each counter is covered, on the side facing the other scintillator in the pair, by a 1 mm lead foil. Requiring coinciding signals in a pair of counters allows the detection of high energy particles, while suppressing backgrounds. Each pair of counters roughly covers a quadrant of the ZEUS $X - Y$ plane, with the fifth counter covering a gap in acceptance due to a flange attached to the proton beampipe. All counter pairs are interleaved and shielded by lead.

3.2.4   The luminosity measurements

The experimental definition of integrated luminosity over a certain time period is

$$\mathcal{L}_{int} = N/\sigma \tag{3.1}$$

where N is the total number of events, for a specific process, which occurred during that time interval and σ is the cross section of the same process.

The luminosity of ep collisions at ZEUS is determined with the expression above, via the Bethe-Heitler bremsstrahlung process [13] $ep \to e\gamma p$, whose cross section is well known from QED calculations [60].

The photon flux from such process is measured in the LUMIG detector [5], a small lead-scintillator calorimeter, situated $Z = -106$ m, which is able to detect photons from ep interactions at $\theta_\gamma < 0.5$ mrad.

The total luminosity gated by the ZEUS experiments in the runs used in this analysis corresponds to 3.82 pb^{-1}, with an uncertainty of 1.1%.

3.2.5   The veto counters

The VetoWall (VW) is a 87 cm thick iron wall, sandwiched by two scintillator layers, located at $Z = 7.27$ m. It helps to shield the detector against products of proton beam gas interactions, and its timing information is used at the trigger level, as a veto.

The C5 counter is a small beam monitor, consisting of scintillators separated by lead sheets. It is located behind the BPC, and its timing information is used to reject proton beam gas interactions occurring between the VW and this counter.

3.2.6   Data acquisition system and trigger

The ZEUS detector is required to detect the products of *ep* collisions resulting from any of the 10^7 bunch crosses that occur per second. In addition, most of the signals observed by ZEUS originate from proton or electron beam gas events or cosmic rays, backgrounds which have much higher rates than that of *ep* interactions. In order to distinguish the interesting physics events and record them, a complex three-level trigger and data acquisition system, shown schematically in figure 3.4 has been developed. This allows the reduction of the input data stream from approximately 20 to 200 kHz (depending on beam conditions) to about 5 Hz, without major loss of physics events.

In general, every component of the ZEUS detector is read out independently and the corresponding data is stored in 10.4 MHz pipelines, while the local First Level Trigger (FLT) analyzes it and takes a decision about the quality of the event (25 cycles of 96 ns). The Global First Level Trigger (GFLT) collects the results of the individual FLT decisions of many components, and determines, with additional calculations, whether the event is likely to originate from a good *ep* collision (64 combinations of FLT results, the so-called FLT trigger slots, are tested). The GFLT decision whether to keep an event is sent back to all components 46 crossings (4.4 μs) after the bunch that produced that event.

If an event was accepted by the GFLT (the acceptance rate is about 800 Hz), then the data from each component are sent to local Second Level Triggers (SLT). Here more complicated operations are performed on the data, and each individual decision is then forwarded to the Global Second Level Trigger (GSLT). The GSLT has up to several milliseconds to process the results and issue a trigger decision. It vetoes more than 90% of all GFLT triggers, reducing the output rate to circa 60 Hz.

Once an event has been accepted by the GSLT it is given a GSLT decision number and the corresponding data are transfered to the Event Builder. This system combines and formats all the component data that carry the same GSLT number into a big data set (an *event*), and forwards it to the Third Level Trigger (TLT).

The TLT consists of a large processor farm, where a simplified version of the standard ZEUS reconstruction program runs. The TLT allows sophisticated and reliable filtering of events, which, when accepted, are then written to a magnetic tape, at a rate close to 5 Hz.
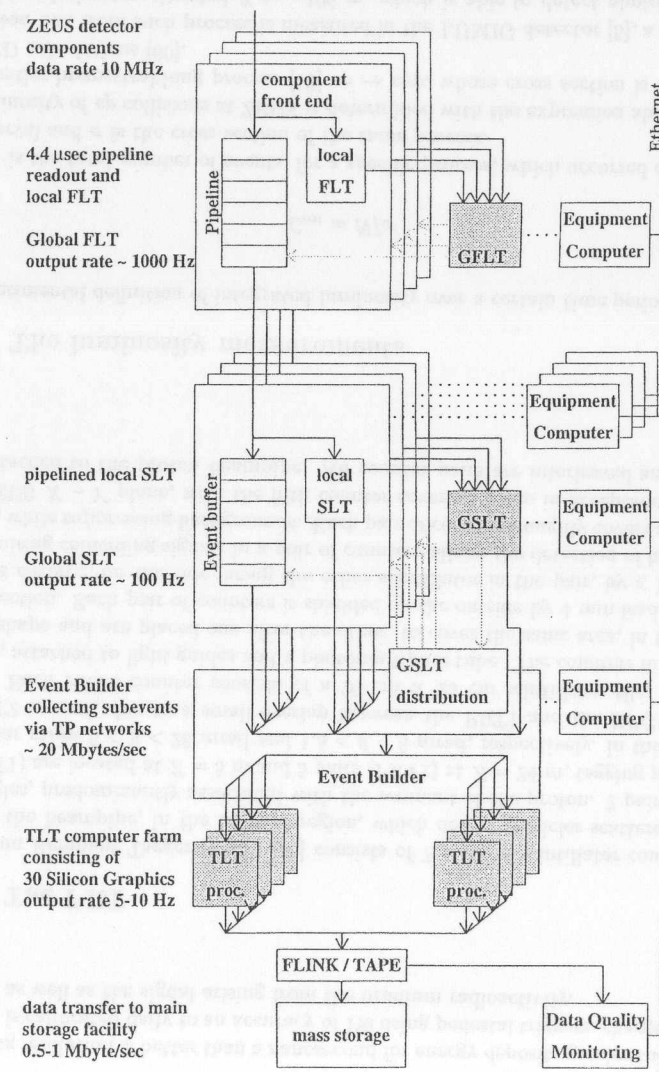
Figure 3.4: Schematic diagram of the ZEUS trigger and data acquisition system (from [82]).

Chapter 4

The Beam Pipe Calorimeter

This chapter discusses the Beam Pipe Calorimeter (BPC) design and construction. First, the requirements and constraints taken into account in the implementation of this new detector, during the Fall '94/Winter '95, are reviewed. Then the detector design and the BPC construction are addressed in detail. Finally, the initial tests of the detectors are briefly described.

4.1 General design considerations

The Beam Pipe Calorimeter, a small calorimeter installed in ZEUS during Spring '95, was intended to significantly enhance the coverage of the ZEUS detector for very low x_{Bj} and low Q^2 neutral current events, allowing measurements of the proton structure function $F_2(x_{Bj}, Q^2)$ with a very good accuracy in a regime previously not accessible at HERA [21, 113].

In the following the requirements on a calorimeter which achieves these physics goals are discussed.

The reviews [40, 3, 41] discuss in some detail the general concepts of calorimetry.

- Requirements on the energy and position resolution of the detector:

  The BPC characteristics should allow an accurate measurement of the proton structure function F_2 over a large range of x_{Bj} and Q^2.

  For such a measurement, the kinematical variables x_{Bj} and Q^2 are reconstructed from the scattered electron energy and angle as measured in the BPC (the *electron method* [96, 97]). In this case the following equations apply (with $\vartheta_{e'} = \pi - \theta_{e'}$):

$$x_{Bj} = \frac{E_e}{E_p} E'_e \frac{1 - \cos \vartheta_{e'}}{2E_e - E'_e(1 + \cos \vartheta_{e'})}, \tag{4.1}$$

$$Q^2 = 2E_e E'_e(1 - \cos \vartheta_{e'}). \tag{4.2}$$

Simple error propagation shows that when the angle $\vartheta_{e'}$ is small, the resolution of these two variables is related with the measured quantities in the following way:

$$\frac{\sigma_{x_{Bj}}}{x_{Bj}} = 2\frac{\sigma_{\vartheta_{e'}}}{\vartheta_{e'}} \oplus \frac{E_e}{E_e - E'_e} \frac{\sigma_{E'_e}}{E'_e} \tag{4.3}$$

$$\frac{\sigma_{Q^2}}{Q^2} = 2\frac{\sigma_{\vartheta_{e'}}}{\vartheta_{e'}} \oplus \frac{\sigma_{E'_e}}{E'_e} \tag{4.4}$$

where $\oplus$ stands for a sum in quadrature.

In the kinematic region covered by the BPC, assuming a typical accuracy in the position measurement of 1 mm [1], and for energy resolutions up to $\frac{30\%}{\sqrt{E'_e}}$ (energy in GeV), the Q^2 resolution stays within the range 3-6%, improving slightly with increasing energy and angle; however the x_{Bj} resolution is strongly limited by the energy resolution, particularly as $E'_e \to E_e$.

Figure 4.1 shows the fractional resolution on x_{Bj} as a function of x_{Bj}, for three values of Q^2, for three possible scenarios: $\frac{\sigma_{E'_e}}{E'_e} = \frac{5\%}{\sqrt{E'_e}}, \frac{15\%}{\sqrt{E'_e}}$ and $\frac{30\%}{\sqrt{E'_e}}$ (energy in GeV; a position resolution of 1 mm was assumed). The x_{Bj} resolution degrades rapidly with increasing x_{Bj} and to obtain a resolution on x_{Bj} of at least 50% up to values $x_{Bj} \sim 10^{-4}$ an energy resolution of the order of $15\%/\sqrt{E'_e}$ is required.

In general, the energy resolution of a calorimeter can be expanded as

[1]A 1 mm position accuracy corresponds to relative accuracies below 2% in the angular determination, given the BPC positioning described in the following and ignoring the contribution from the resolution of the vertex measurement by the central tracking chambers, which is negligible in most cases but in the case of events with no reconstructed vertex obviously dominates the angular resolution
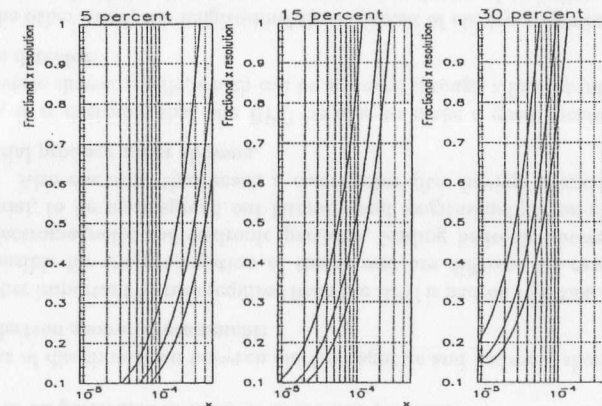
Figure 4.1: Fractional resolution on x_{Bj} as a function of x_{Bj} for Q^2=0.3, 0.5, 0.7 GeV^2 for the three energy resolutions considered (5,15 and 30%). In each case, Q^2=0.3 GeV^2 is the leftmost curve [21]

$$\frac{\sigma_E}{E} = \frac{A}{E} \oplus \frac{B}{\sqrt{E}} \oplus C. \qquad (4.5)$$

where $\oplus$ denotes a sum in quadrature.

The first term in expression 4.5 represents contributions which can be neglected at high energies, namely electronics noise; the second term accounts for the contributions by processes governed by Poisson statistics, and it is usually the dominant term: it includes sampling fluctuations, fluctuations in the number of photoelectrons produced in the photocathode of a PMT and photoelectron multiplication in the PMT dynodes (see section 4.2.3). The last term is an offset, which can be due, for example, to a faulty calibration or non-linearity of the detector.

A *homogeneous calorimeter*, made of a single material which acts simultaneously as absorber and active material (for example, heavy crystals like $PbWo_4$) can reach resolutions of $\sim 1\%/\sqrt{E}$ (E in GeV), dominated by the light yield. However, *sampling calorimeters*, where layers of absorber alternate with layers of active material, achieve typical resolutions, for a one radiation length sampling step, of $15\%/\sqrt{E}$ (E in GeV), due to the contribution from sampling fluctuations to the total resolution. These fluctuations depend on the frequency of shower sampling in the calorimeter, with, approximately

$$\left(\frac{\sigma_E}{E}\right)_{samp} \propto \frac{\sqrt{t_{samp}}}{\sqrt{E}} \qquad (4.6)$$

where t_{samp} is the sampling thickness measured in *radiation lengths* [2]. Therefore the energy resolution of a sampling calorimeter improves with decreasing sampling thickness.

The position resolution depends mainly on the density of the absorber, transverse segmentation and *sampling fraction* [3] of the calorimeter. A finely segmented ($< 1 \times 1$ cm) sampling calorimeter can achieve position resolutions better than 1 mm. The alignment of the calorimeter, and the reconstruction algorithm should also be such that the overall position bias is kept at the level of ~ 1 mm.

- Requirements on the linearity, uniformity and calibration of the detector:

  For a good structure function measurement, it is also necessary to ensure that the BPC response is linear and that it can be very accurately calibrated, guaranteeing, to a level better than 1%, a reliable determination of the absolute energy of incoming electrons and an uniform response over the covered area.

  Although tools and algorithms for calibration, and for ensuring the uniform response of the device can be developed for both crystal and sampling calorimeters (see section

---

[2]The radiation length of a material is defined as the length that an particle must travel in that medium to lose on average $1/e$ of its energy through radiation.

[3]The sampling fraction for a certain particle is the ratio of the energy deposited in the active layers of a calorimeter to total energy deposited in the detector by such a particle. This quantity depends on the particle type: $e^{\pm}, \mu^{\pm}, \pi$, etc. - details are discussed in [17]).

5.4.1), the first ones carry the risk of having impurities which increase the difficulty of the task: careful (and time consuming) tests and selection of the crystal samples have to be performed in order to avoid this problem.

- Means of discrimination between electromagnetic and hadronic showers; longitudinal electron shower containment:

  Another important feature required from the BPC is hadron rejection. The processes responsible for the propagation of the shower are different for cascades initiated by electromagnetic and hadronic particles, leading hadronic showers, in a dense material, to be more spread out laterally and longitudinally than electromagnetic ones. Also electrons that reach a calorimeter after having interacted with other material produce wider showers.

  Thus, it is desirable that the BPC be able to make a good measurement of the transverse shower profile, which can be achieved through a fine lateral segmentation of the detector.

  On the other hand, the longitudinal development of electromagnetic showers scales approximately if the distances are measured in terms of radiation lengths of the material in use, X_0, given approximately by $X_0 \sim 180 A/Z^2$ g/cm^2 (A: mass number (g), Z: atomic number), while in hadronic showers the equivalent quantity is the *absorption* or *interaction length* of the material, $\Lambda_0 \sim A/(N_A \sigma_i)$ (N_A: Avogadro number, σ_i: inelastic cross section).

  Therefore, a high density material with a short radiation length and a relatively large interaction length should be chosen to optimize the performance of the BPC. The detector should be deep enough so that it contains 27.5 GeV electromagnetic showers, but short in that hadronic deposits are negligible.

- Impact of transverse shower leakage and the *Molière radius*:

  Leakage of energy out of the calorimeter is another factor that causes fluctuations in the energy deposit of the shower, worsening the energy resolution of the device.

  In an electromagnetic shower, up to the *shower maximum* [4] the transverse shower width is smaller than a radiation length. Beyond that point multiple scattering becomes increasingly important, and the Molière radius r_M of the detector is used to characterize the dimension of the shower: roughly 95% of the shower energy is contained laterally within a radius $2r_M$, where $r_M \sim 7A/Z$ g/cm^2.

  A material with a short Molière radius, ensuring that the transversal shower spread is small, allows useful measurements to be made at impact points very close to the edge of the detector, maximizing its acceptance.

- Requirements on the calorimeter time response:

---

[4]The shower maximum is the the depth at which the shower has a maximum number of particles: $t_{max} \approx \ln(E_0/E_c)/\ln 2$ where E_0 is the initial energy and $E_c \approx 550/Z$ MeV is the critical energy of the medium, at which the ionization energy loss starts to dominate the loss by bremsstrahlung.

Because particles from proton beam gas interactions, which are an important background to the BPC inclusive measurements, reach the BPC at a different time than particles from *ep* interactions ($\Delta t \simeq 20$ ns), a good time measurement in the calorimeter is a powerful means of rejecting such events.

This is particularly crucial at the trigger level, where this background is responsible for energy deposits in the BPC at very high rates. Therefore it is desirable that the BPC and its readout achieve good timing resolutions.

- Restrictions due to the available space inside ZEUS:

Since the BPC was not originally planned in ZEUS, its design has to cope with the existing detectors, support structures and free spaces in the ZEUS detector.

Its purpose of extending the ZEUS acceptance to scattering angles $\vartheta_{e'}$ as small as possible places it naturally just behind the RCAL hole around the beam pipe, providing a continuous coverage with the main ZEUS detector.

The available space in this location is limited to roughly 15 cm $\times$ 15 cm $\times$ 30 cm on each side of the beam. This led to the design of two compact calorimeter modules, located one on each side of the beam pipe, and strongly constrained the geometry and overall dimensions of these devices, as well as of their readout system and support structures.

- Requirements on radiation hardness:

Due to the vicinity of the beam it could be anticipated that the BPC receives a high radiation dose over each data taking period. Thus, it is necessary for the detector to be reasonably radiation hard (measurements and details on the dosage received in '95 are presented in section 5.4.4).

- Presence of a magnetic field:

The BPC is located in a magnetic field (up to ~ 400 Gauss). Its design has to ensure that this will not affect the performance of the detector.

4.2   Detailed description of the BPC

4.2.1   Calorimeter modules

The considerations above, together with time and cost of the project, have defined the design of the Beam Pipe Calorimeter, whose implementation is described below.
The BPC consists of two electromagnetic sampling calorimeters, located one on each side of the beam pipe, along the X-axis, at $Z = -2937$ mm in the ZEUS coordinate system [5] (see figure 4.2 and 4.3).
The ZEUS beam pipe was modified in front of these two modules in order to have two low-mass aluminum windows (0.016 radiation length at $Z = -2498$ mm) which allow the

---

[5]The ZEUS right handed coordinate system is defined with the origin at the nominal interaction point, the Z-axis pointing in the proton beam direction, and the X-axis pointing horizontally towards the center of the HERA ring

electrons to exit the beam pipe and reach the BPC after transversing a minimal amount of inactive material. These two windows, asymmetric with respect to the beam line [6] define the region of acceptance of each detector module, the (*fiducial region*).
The two modules are called *BPC North* and *BPC South*. The BPC North is located on the positive ZEUS X-axis (north of the beam pipe), and the BPC South, a smaller module, is located in the negative X-axis. The modules are approximately centered around the $Y = 0$ position, and their edges sit at $X \sim +4$ cm and $X \sim -7$ cm respectively (see survey results 4.2.6 for details). The alignment is known to an accuracy of 0.5 mm and the distance between the two calorimeter modules is mechanically constrained with an uncertainty of less than 0.1 mm.
Each of these modules consists of twenty-six 3.5 mm thick tungsten alloy plates [7], the passive absorber, of density 18 g cm^{-3} and radiation length 3.87 mm, and dimensions 13.8 cm $\times$13 cm and 9.8 cm $\times$13 cm for BPC North and South respectively.
The tungsten layers alternate with the active layers, consisting of 7.9 $\pm$ 0.02 mm wide and 2.6 $\pm$ 0.1 mm thick scintillator strips (sometimes called *fingers*), placed side by side;

---

[6]The asymmetry of the BPC modules around $X = 0$ reflects the requirement that no direct or reflected synchrotron radiation from the electron beam hits either calorimeter.

[7]DENSIMET 18K, 94.5% tungsten and 5.5% nickel-copper binder, an easily machined material
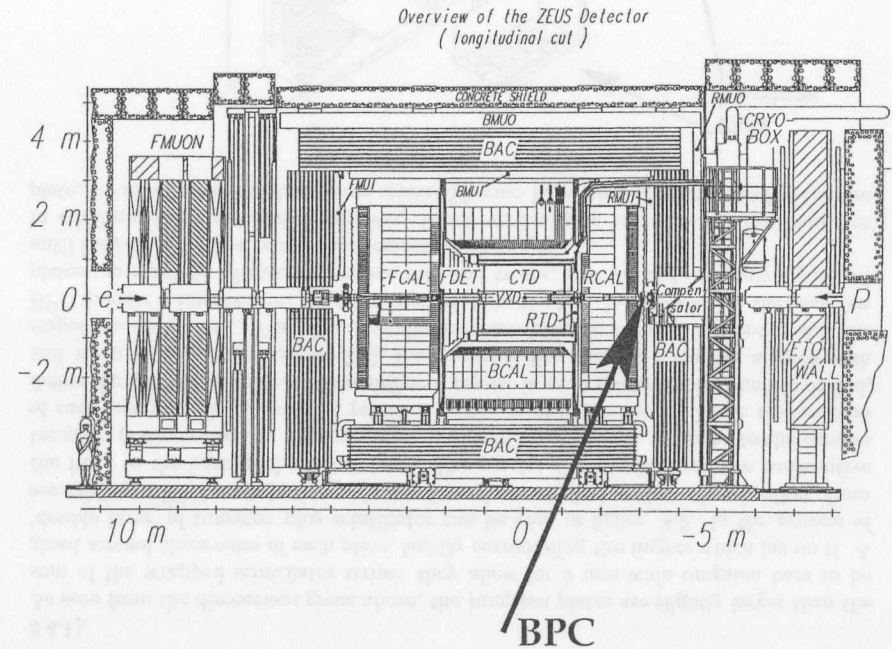
Figure 4.2: The BPC location inside the ZEUS detector.

the scintillator material (SCSN-38) consists of a polystyrene doped with two wave length shifting dyes, and its density and radiation length are, respectively, 1.03 g cm^{-3} and 42.0 cm. It has a relatively high light yield, a short decay time (2 ns), and good stability against aging and radiation [27].

The orientation of the scintillator strips alternate from layer to layer in the horizontal direction (odd numbered scintillator layers, counting from the front of BPC) and vertical direction (even numbered scintillator layers), as seen in figure 4.4.

The horizontal strips have a length of 120 mm for BPC North, and 88 mm for BPC South, and both modules contain 16 strips per each scintillator layer. The vertical strips have a length of 128 mm in both calorimeters, but while BPC North contains 15 fingers per layer, the BPC South has only 11.

Apart from the difference in dimensions, both modules have the same structure.

The vertically oriented fingers, which provide the X position measurement, are labeled NX1..NX15 (and SX1..SX11, for the South module), counting from the beam, while the horizontal ones are labeled NY1... NY16 (SY1...SY16), counting from the bottom.

Each set of tungsten plate plus scintillator layer corresponds to a thickness of 0.91 radiation lengths.

Each scintillator finger, finely polished, is wrapped in 27.5 μm thick aluminum foil, which, not only increases its light yield, but also decouples neighboring fingers. Between the aluminum foil and the scintillator strip there is an air gap: added to the strip width and the aluminum wrapping, it sums up to a nominal 8 mm finger width. The fingers are aluminized at one end and are read out at the other end, as described below.

Detailed studies on the scintillating material [96], testbeam and *in-situ* results (see sections 5.2.3 and 5.4.1) show that the attenuation length of the strips is large compared to the length of each finger (see figures 5.5 and 5.22). This effect, leading to a dependence of the energy measurement on the impact position, can be corrected offline (see section
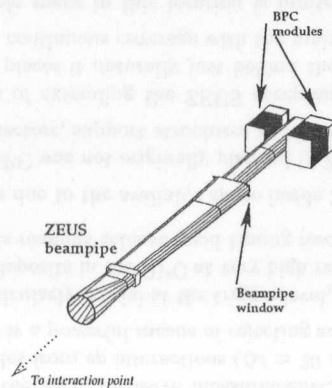
Figure 4.3: The BPC location around the beam pipe.

5.4.1).

As seen from the dimensions given above, the tungsten plates are slightly larger than the sum of the wrapped scintillator strips: they allow for 5 mm wide tungsten bars to be glued around three sides of each plate, tightly surrounding the fingers which lay on it. A 'double layer' of tungsten plus scintillator can be seen in figure 4.5. In the process of assembling a BPC module these 'double layers' are stacked on top of each other, from the front to the back of the calorimeter. The precise distance between two consecutive tungsten plates is fixed by high precision machined brass spacers, attached to the corners of each tungsten plate, avoiding pressure on the scintillator layers. These spacers also define the internal alignment of the different layers: in each spacer a round hole is drilled, and when all the layers are stacked, the corresponding holes are roughly aligned with respect to each other. Then four metallic rods are inserted through the holes, and the BPC module is inverted, bringing the front plate to the top. In this position the tungsten plates are carefully aligned to remove tilts and twists, and the rods strongly tightened until they do not allow relative movements of the parts.

In addition, there are narrow grooves, drilled vertically in the first and last tungsten plate, ~5 mm from each edge, where crystal Thermo-Luminescent Dosimeters (TLDs) are
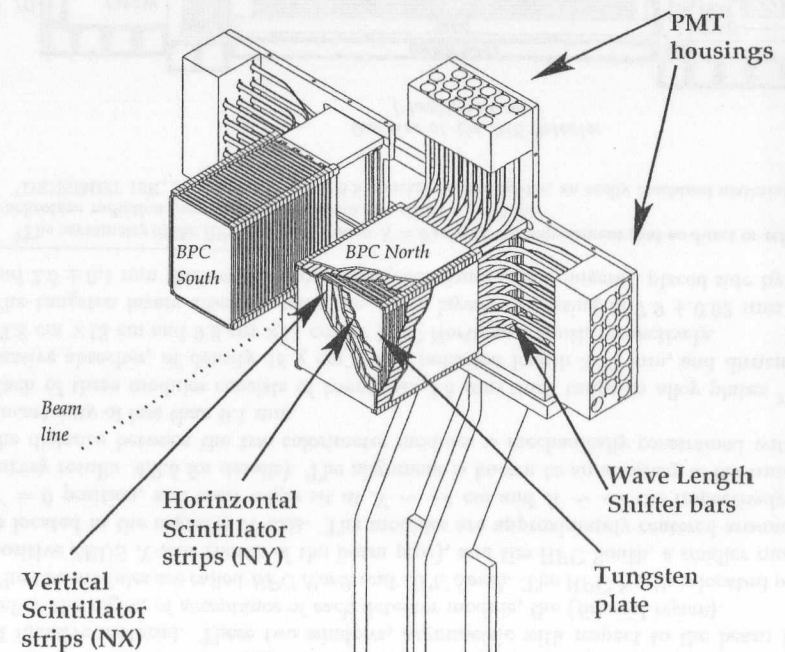
Figure 4.4: A CAD drawing of the BPC: the scintillator strip positioning, as well as the WLS readout can be seen in the figure.

inserted. These dosimeters, replaced several times during the data taking period, allow an estimate of the radiation dose received by the BPC (see section 5.4.4), measuring doses up to 3 kGy.

In general, the size of the BPC components and relevant distances are known to an accuracy of 0.1 mm.

4.2.2 Optical readout

Each scintillator strip is read out from one end, using Wave Length Shifter bars (WLS). These WLS are placed in the Z direction, along the edges of the scintillator strips, over two faces of each BPC module: X fingers read out from the top (bottom) face of the BPC North(South), and Y fingers read out in the face of each module furthest away from the beam. Each WLS bar is coupled to all the strips with the same X (or Y) position in consecutive layers; this scheme does not allow for longitudinal shower measurements.

The WLS are 7 mm wide and 2 mm thick bars of Polymethyl Methacrylate (PMMA) doped with a fluorescent dye and a UV absorbent, which cuts off wave lengths below 360 nm. A sample of the bars was scanned in a test bench, together with some scintillator fingers, to verify its optical properties [96]. The WLS materials is stable against radiation [27], it is easy to machine, and has a high light yield compared to similar materials.

This WLS material absorbs light in the range 400-480 nm, which overlaps with the emission spectrum of the scintillator material, extending from 380 to 450 nm, and re-emits the light around 480 nm, which corresponds to the wavelength region of highest response
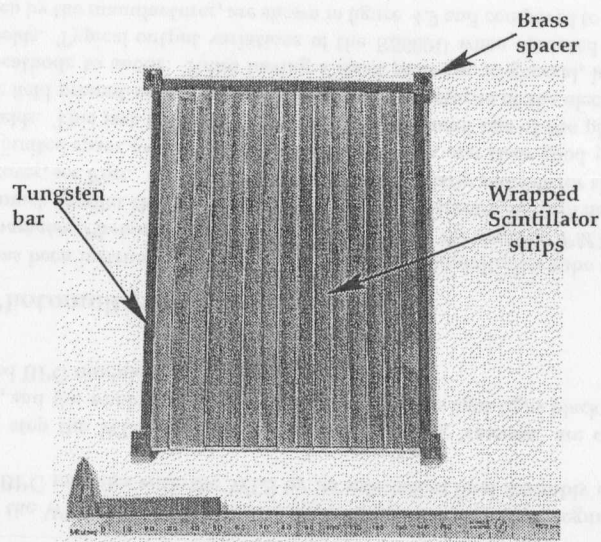
Figure 4.5: A double layer of tungsten plate plus scintillator fingers.

for the photomultiplier tubes in use (see next section).

An important consideration is that the use of WLS bars along the side of the BPC can introduce non-linearities in the energy response of the detector. Since the longitudinal position of the shower maximum depends on the energy of the incoming particle, the scintillator light is collected by the WLS at different effective depths, corresponding to a longer or shorter path in this material. Thus, the effect of the light attenuation inside the WLS depends on the energy of the particle hitting BPC.

This problem can be solved by choosing the optical density of the fluorescent dye such that only part of the light coming from a scintillator finger into a WLS bar is absorbed in the WLS. The longitudinal non-uniformity can be compensated by introducing reflection masks behind each WLS bar. These masks are obtained by printing a black dotted pattern on *Tyvek paper*[8], with a density of dots that changes from the front of BPC (higher reflectivity) to the back (lower reflectivity); in addition, the open end of each bar is aluminized. The longitudinal uniformity achieved over the WLS is 2%.

The WLS bars are kept mechanically aligned with the scintillator fingers and optically separated from each other by two rigid 'cassettes', corresponding to X and Y readout, and plastic spacers, which also ensure an air gap between the scintillator and the WLS material. After the last calorimeter layer, the WLS bars are bent at a 90° angle, with a 30 mm radius, transporting the light to the photomultiplier tubes. The bending causes a

---

[8]Tyvek paper is made of compressed spun polyethylene, it is a diffuse reflector with a very high UV reflectivity (comparable to aluminum foil).
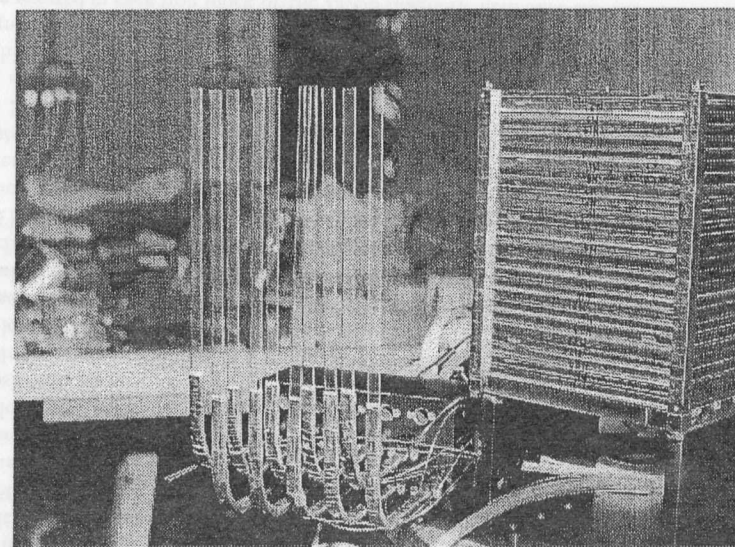
Figure 4.6: The BPC north module during assembly. The sandwich structure of the calorimeter as well as the WLS bars can be seen.

light loss in the WLS of the order of 10% when compared to straight segments.
One of the BPC modules with the WLS by its side before final assembly can be seen in figure 4.6.
In the final step the WLS bars, inside the corresponding 'cassette' are coupled to the calorimeter, and the whole module is carefully wrapped in light tight black Tedlar paper. Unassembled BPC module can be seen in figure 4.7.

4.2.3 Photomultiplier tubes

The BPC has been instrumented with a new type of photomultiplier tube (PMT). These tubes (*Hamamatsu Photonics* R5600U-03), advertised as *the smallest PMT in the world*, are indeed much smaller than the usual types (12 mm diameter, 15 mm height including insulation cover, see Figs. 4.8 and 4.10), and are particularly suitable for this calorimeter due to the limited space available around the beam pipe, and their good performance in magnetic fields. This last feature is mainly due to the small size of the photomultiplier. A magnetic field present near a tube will affect the trajectories of the electrons traveling from photocathode to anode. Tubes having a short path are, in general, less sensitive to magnetic fields. Typical output variations of the R5600U when operated in a magnetic field, as given by the manufacturer, are shown in figure 4.9 and compared to a conventional tube, Hamamatsu R647.

The R5600U-03 are 8-stage metal channel dynode photomultiplier tubes, supporting voltages up to 1000 V, with a typical current amplification of 3.10^5 at a supply voltage of 800
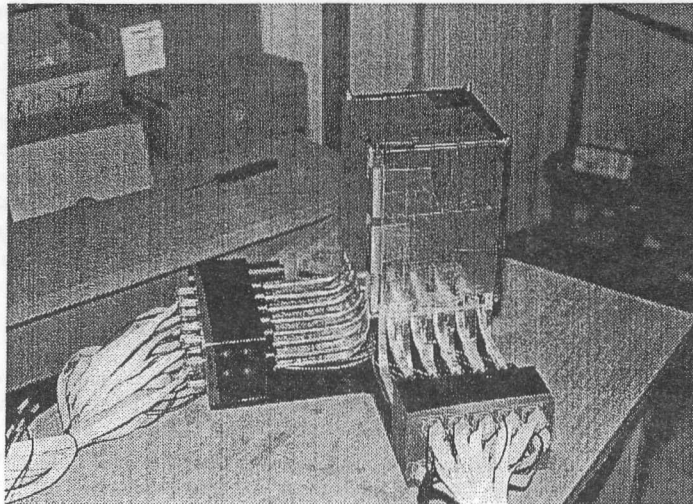
V. The photocathodes are made of a bialkali material, and the window is UV transparent, resulting in a spectral response range from ~ 185 nm (limited by the glass window) to ~ 650 nm (limited by the bialkali material), peaking at 350 to 500 nm. The *quantum efficiency*, defined as the ratio of the number of photoelectrons released in the cathode per incident photon, reaches approximately 20% at the peak wavelengths. The UV glass window was chosen for being more radiation resistant compared to the less expensive borosilicate glass: if exposed to the same dose of either ^{60}Co Gamma radiation, or 14 MeV Neutron radiation, of a wavelength ~ 300 nm, the UV glass suffers 1.5 to 2 times less loss of transmittance.

These PMT's also have a very fast response, with a typical rise time (time taken for the signal to rise from 10% to 90% of its maximum) of 0.65 ns, and a Full Width at Half Maximum (FWHM) of only a couple of nanoseconds. The transit time is ~ 5 ns at 800 V. The pulse linearity was measured by the manufacturer to be better than 1% up to output currents of 10 mA(typical), reaching a 5% deviation at ~ 30 mA. The anode dark currents are reported to be less than 1 nA at 800 V. However, under some conditions, *bursts* of dark pulses were observed during the testing of our PMT's (see below).

The BPC PMT's are located on the sides of the detectors inside two ARMCO magnetic iron shielding 'houses', one for X and one for Y strips readout. Their main purpose is to shield the PMT's from the high magnetic field that exists in the area, reducing the magnetic field around the PMT's from 400 Gauss to approximately 20 Gauss. The net force exerted in each iron block by the ZEUS magnetic field once the detector is in its final location was measured and found to be negligible. These boxes also serve as mechanical support for the WLS bars (and the lucite fibers described in section 4.2.3) and the PMT's. The housings can be seen in figure 4.7, and in more detail in figure 4.10; they are further away from the beampipe than the calorimeters, minimizing the exposure of the PMT's to radiation and to an even stronger magnetic field. To prevent possible short circuits, each

Figure 4.7: The finalized BPC North module before installation.
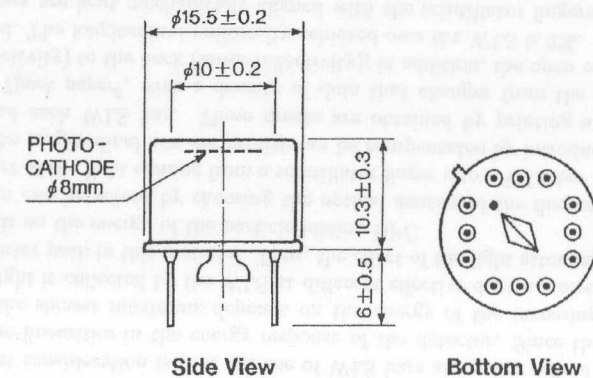
Figure 4.8: PMT cross section.

PMT is isolated from the iron through a PVC tube.

The mounting of the PMT inside the iron block guarantees that the orientation of the WLS with respect to the PMT's is uniform and optimal. Due to the dynode structure of the tubes, the overall light yield can vary by roughly 10% depending on the angular orientation between the PMT's with respect to the rectangular cross section of the WLS bars.

PMT testing

A series of systematic checks were made on each tube (seventy tubes in 1995, plus twenty in 1996) to study their performance.

The PMT's were placed, one by one, inside a light tight box. A yellowish Light Emitting Diode (LED-Hewlett Packard HP HMLA-DL00 Amber LED, $\lambda = 592$ nm) was placed in front of the PMT's to inject light, and it was driven with a square pulse with an amplitude ~ 3 V and width ~ 10 ns, generated by an Hewlett Packard pulse generator. The distance between the LED and the PMT was adjusted to make use of the full signal range accepted by the readout electronics, and it was kept at a fixed value throughout the testing of all samples. A reference PMT was also used to continuously monitor the light source stability.

For most tests the PMT output was sent to a LeCroy 2249A Analog to Digital Conversor (CAMAC module) which integrates the charge during a time τ determined by its input
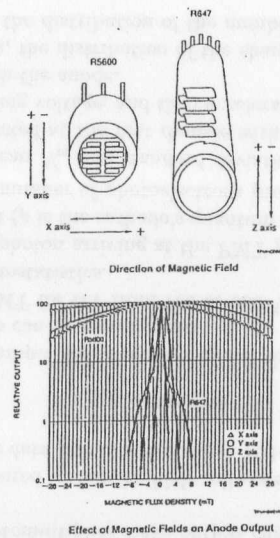
Figure 4.9: Relative response of a Hamamatsu R5600U-03 PMT in the presence of a magnetic field, compared to that of a conventional tube, Hamamatsu R647.

gate (in this case, 120ns, preceding the pulse by ~ 45 ns). The ADC data were read out with a VME-based OS9 processor (see figure 4.11). For each setting, this measurement was repeated 5000 times, and the results were stored by means of histograms which allow
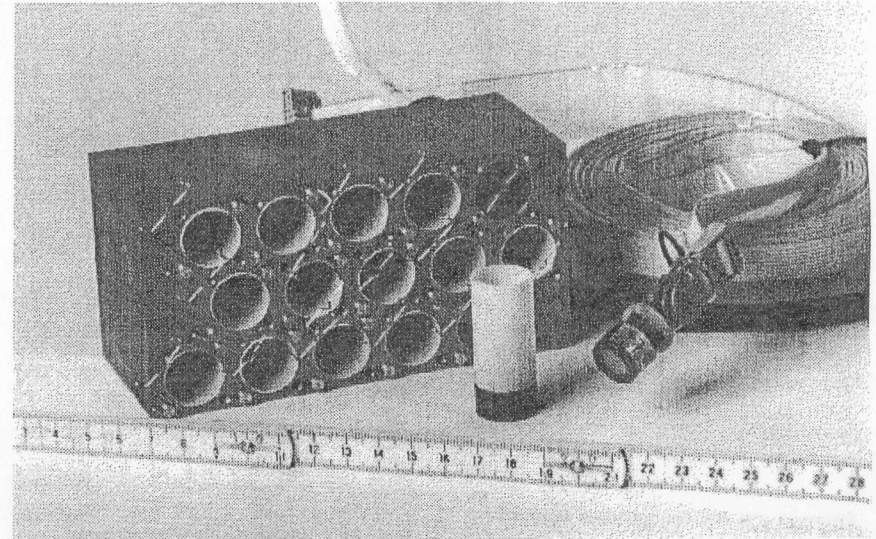
Figure 4.10: PMT housing.
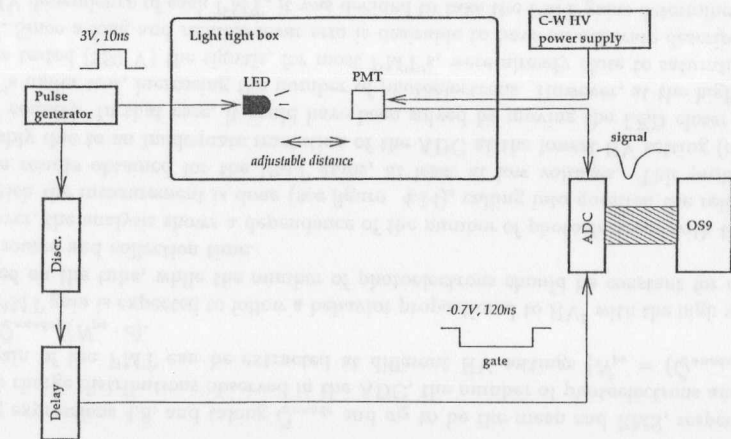
Figure 4.11: Schematics of the setup used in PMT testing.

the determination of the photomultiplier mean output charge, $\bar{Q}_{anode}$, and its spread σ_Q via Gaussian fits.

The output charge was measured versus the high voltage settings from HV=600 V to 950 V, in 50 V steps, and the data points in the range 700-900 V were fitted by the curve

$$\bar{Q}_{anode} = 10^a HV^b. \qquad (4.7)$$

Figure 4.12 shows, as an example, this curve for one of the PMT's under test.

A distribution of the b values can be seen in figure 4.13.

The absolute gain of each PMT for HV from 700 to 900 V was also estimated, based on the signal spread due to photostatistics.

In a simplified picture, each photon arriving at the PMT photocathode has a probability ρ of releasing a photoelectron (ρ is the cathode's quantum efficiency). For a large number of incident photons N_γ, the number of photoelectrons produced, $N_{pe} = N_\gamma \cdot \rho$, follows a Poisson distribution, with mean $\bar{N}_{pe}$ and standard deviation $\sqrt{\bar{N}_{pe}}$.

The photoelectrons are collected at the first dynode with a collection efficiency $\eta(HV)$, which depends on the operating voltage, and then accelerated and multiplied through the dynode chain until they reach the anode.

Neglecting other fluctuations, the distribution of the charges collected at the anode in a certain time interval follows the distribution of the number of photoelectrons created at the cathode:

$$\bar{Q}_{anode} \simeq \bar{N}_{pe} \cdot e \cdot G, \quad \sigma_Q \simeq \sqrt{\bar{N}_{pe}} \cdot e \cdot G, \qquad (4.8)$$

where e is the electron charge and the photomultiplier gain G depends on the HV applied to the PMT, and can be expressed in terms of the collection efficiency η and multiplication gain M: $G(HV) = \eta(HV) \cdot M(HV)$.
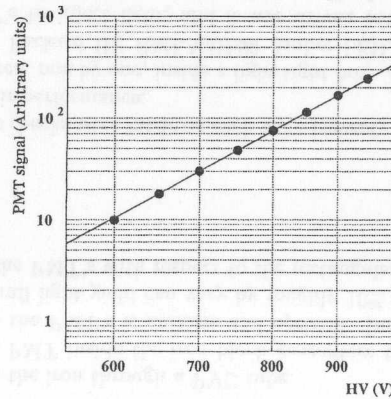
Using expressions 4.8, and taking $\bar{Q}_{anode}$ and σ_Q to be the mean and RMS, respectively, of the charge distributions observed in the ADC, the number of photoelectrons and then the gain of the PMT can be extracted at different HV settings ($\bar{N}_{pe} = (\bar{Q}_{anode}/\sigma_Q)^2$, $G = \bar{Q}_{anode}/(N_{pe} \cdot e)$).

The PMT gain is expected to follow a behavior proportional to HV^b with the high voltage applied on the tube, while the number of photoelectrons should be constant for a fixed light source and collection time.

However, the analysis shows a dependence of the number of photoelectrons with the HV at which the measurement is done (see figure 4.14), calling into question the reliability of the results obtained for the PMT gains, at least at low voltages. This problem is probably due to an inadequate resolution of the ADC at the lowest HV setting ($\sigma_Q \sim 1$ ADC counts). In that case, it could have been solved by moving the LED closer to the PMT's under test, increasing the number of photoelectrons. However, at the higher HV values tested (950 V) the signals, for most PMT's, were already close to saturating the ADC. Since a long and reliable lever arm is desirable to have an accurate description of the HV dependence of each PMT, it was decided to take the PMT gains determined from expressions 4.8 only as indicative values, and use the results of fits to expression 4.7 to characterize each PMT quantitatively. A database was built where the data from the individual PMT's were stored.

Since the PMT gain is proportional to HV^b, its stability depends on the HV stability through

$$\frac{\sigma_G}{G} = b \frac{\sigma_{HV}}{HV}. \qquad (4.9)$$

For a HV stable at a level better than 0.1% and typical values of b found in these tests, the PMT gain is expected to be stable at a level close to 0.5%.

Figure 4.12: PMT output charge versus HV supplied.
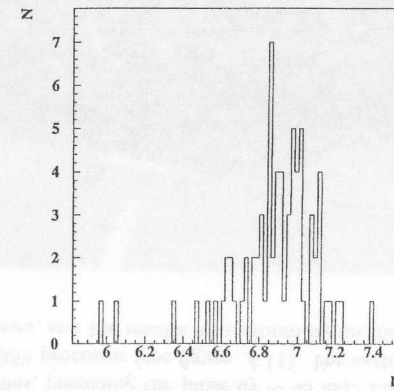
Figure 4.13: Parameter b for all PMT's under test.

The stability and reproducibility of the results was investigated, repeating the measurements several times during approximately 20 days for a small number of PMT's, four of which were kept continuously under 900 V in a light-tight container (monitored daily). The repetition of the measurements showed only variations compatible with the limited set-up stability (5%), with no systematic trends observed in the PMT response to light versus HV.

The transit time variation with HV was also measured, and found to be at the level of 1 ns over 300 V, compatible with the manufacturer's data.

A check using an oscilloscope was performed for each PMT at 700, 800, and 900 V; in this check the pulse shape for a stable light source was observed, the pulse height at each voltage registered, and noise, in the absence of any light, investigated. Most PMT's behave as expected with respect to pulse shape and pulse height. However, in the noise studies, some PMT's showed unexpected pulses, in a light tight environment, with typical rise and falling times of 1 to 2 ns and a total base width of $\sim$ 5 ns. In the following these pulses are referred to as 'dark pulses'. The dark pulses' amplitude varied from sample to sample from a few millivolts to over 100 mV, and their rate from a few Hertz to several hundred. It was also observed that, for a noisy PMT, the behavior of the dark pulse amplitude with the supplied HV followed that of the PMT gain. For each PMT, at each of the above mentioned voltages and with the help of the oscilloscope, the trigger threshold corresponding to a dark pulse rate of $\sim$ 1 Hz was determined, and, inversely, the rate of dark pulses for a trigger threshold of -10 mV was registered. The PMT's with more severe dark pulses were found to belong to the same production batch.

Using the dark pulse information, together with the other tests and gain measurements, a total of 70 PMT's (1995 batch) have been classified into three groups, according to the characteristics listed below:
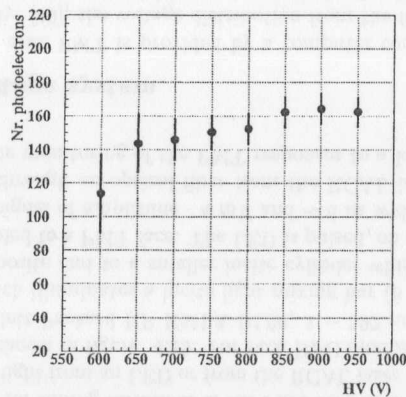
Figure 4.14: Number of photoelectrons determined from equation 4.8 for a sample PMT at different HV.

- Class C, 'bad tubes'

  - The parameters a or b of the PMT are systematically away from all other tested tubes (1 PMT).

  - Distinct non-linear behavior with HV (1 PMT).

  - Abnormal pulse shape (2 PMT's).

  - Dark pulses, at a 1 Hz rate, of amplitude greater than 10 mV at 700 V supply voltage, or greater than 80mV at 900 V (13 PMT's)

- Class B

  - Dark pulses, at a 1 Hz rate, of amplitude between 20 to 80 mV at 900 V supply voltage (16 PMT's).

- Class A, 'good tubes'

  - PMT's with dark pulses up to a maximum amplitude, at 1 Hz rate, of 20 mV at 900 V. These PMT's do not show any problem at 700 V (37 PMT's).

This classification allowed us to use the best PMT's in the channels of the BPC North which correspond to the fiducial area.

A description of the dark pulses' problem, together with some of the faulty photomultiplier tubes was sent back to Hamamatsu, where possible causes for this problem were investigated; the company believes the problem was in the process of deposition of the cathode's film, which has been improved, reducing significantly (or even eliminating) this fault in PMT's produced afterwards (this was confirmed with the same set of tests performed in an additional sample of 20 PMT's, received in 1996, all classified as good tubes according to the above criteria).

During the data taking period the PMT's were checked on a regular basis, both through the monitoring tools described below, and with dedicated studies during HERA operation breaks. These included the rate and amplitude measurements described above, and investigations of possible DC-offsets (using an Amperimeter with a high input resistor). After four months of running in ZEUS, five PMT's, previously classified as bad tubes, developed much wider dark pulses, of 20 to 200 μs, and amplitudes of the order of 10 mV, at a few hundred Hertz rate; the dark current versus HV for these PMT's showed a very steep rise around 750 V, eventually exceeding the output current limit of the HV power supply. This 'discharge effect' is believed to be associated with the previous dark pulse problem. The faulty PMT's (corresponding to strips NY16, SX10, SX11, SY6 and SY15), were replaced without loss of good quality data, and the features observed in ZEUS were reproduced in a test bench. At the end of the data taking period all PMT's underwent new tests, showing that the dark pulses had become more severe for almost all PMT's.

PMT monitoring tools

The BPC is equipped with a pulsed light calibration system that injects light into the PMT's by means of optical light fibers (lucite fibers). It is intended to monitor the gain of

each PMT, and check for timing variations of the PMT response. The optical fiber system is used both to inject light from an LED or from the RCAL laser calibration system [103], and is schematically shown in figure 4.15. For each BPC module, this system consists of an amber LED (Hewlett Packard HP HMLA-DL00, $\lambda = 592$ nm), located in one of the PMT iron boxes, which illuminates a lucite light mixing bar ($8 \times 8 \times 80$ mm^3); this bar is coupled on the opposite end to a smaller lucite cylinder which fans out into multiple light fibers, each coupled to a PMT face. The LED is pulsed, on special test runs and test triggers, by a stable signal of amplitude - 4 mV and ~ 6 ns width, and the same mixing bar can also be fed through an optical fiber from the RCAL laser distribution system. This system allows the monitoring of the PMT responses to a level of 1 to 2%.

4.2.4   High-voltage system

The high voltage for each PMT is provided by a computer controlled Cockroft-Walton type HV power supply [49]; the voltage distribution from the first to the last dynode is 1:1:1:1:1:1:1:0.5, and it is done at the HV power supply level, with the individual voltages sent to the PMT base [9] through a flat cable (see figure 4.16). This system supplies voltages in the range from 600 to 1000 V.

Some general advantages of using a Cockroft-Walton system are:

- It has a small power consumption (an order of magnitude less than a resistive base), thus producing less heat.

- It can be easily and safely controlled and operated, with a maximum external voltage of only 20 to 30 V.

---

[9]The PMT base contains only resistors and capacitors to match impedances
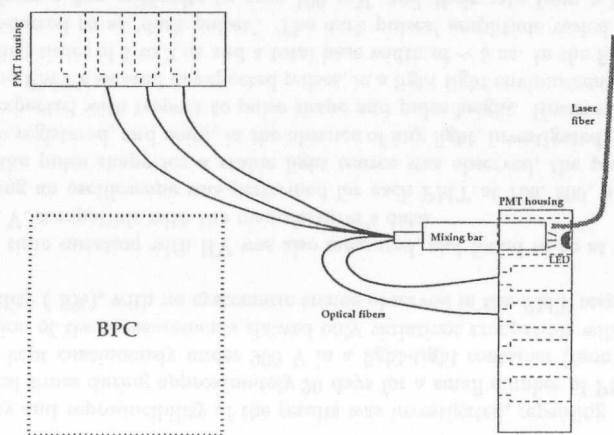
Figure 4.15: The light distribution system for monitoring BPC PMT's.

- The output voltage is stable to $< 0.1\%$.

- The PMT is protected against short circuits and exposure to light, as the maximum current supplied is low.

In the system used, the microprocessor that controls the HV allows the individual setting of each PMT voltage, in a *user-friendly* way, monitoring the stability of the voltages and of the current drawn by each channel. If one of the currents delivered exceeds a user programmable limit of 100 μA, this channel will turn off. Once a channel is off, the system will attempt to turn it back on, up to a number of attempts defined by software (10 times for the BPC).

The operating voltage of each PMT is set individually in order to equalize the response of all the channels (see section 4.3.1), and is in the range 600-800 V.

4.2.5   Further details on the BPC

The veto tiles

A veto tile, consisting of a 5 mm thick scintillator sheet enclosed by two 2 mm thick lead plates, and read out on both sides by WLS and PMT's, is placed behind each BPC module. These back tiles are intended as means to help separate electromagnetic from hadronic showers, but have not been used in the present analysis.

Each of the BPC modules, with the respective PMT iron blocks and back tile is mounted on a aluminum support structure, used to fix the calorimeters inside the ZEUS detector.
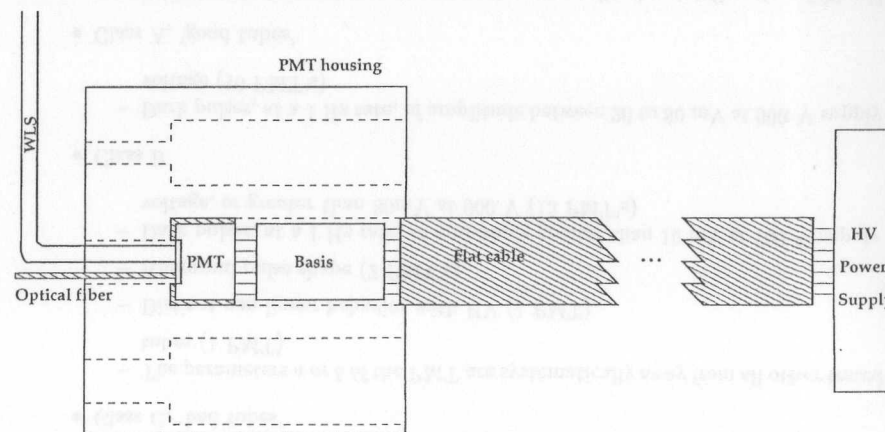
Figure 4.16: Schematic diagram of the PMT connections to the HV system.

As stressed above, the BPC is the result of a compromise between a device providing an adequate performance for the physics questions to be studied, and a reliable detector which could be implemented and its performance understood in a short time scale. Upgrades to this detector, namely the possibility to replace it by a crystal calorimeter, are under study. In addition, during '97 a silicon tracker was installed in front of the BPC fiducial region, allowing an improvement on the electron impact position measurement, as well as an accurate determination of each event vertex.

Only the BPC North has been used for physics analysis due to the very small acceptance of the other module, which, as originally planned, has been used exclusively for alignment purposes.

4.2.6   BPC alignment and survey

The BPC position in ZEUS (see figure 4.17) has been surveyed at the end of the 1995 data taking period.
This optical survey, which relies on existing reference marks on the ZEUS detector, has faced several technical difficulties, but its results, displayed on table 4.2.6, have been confirmed by an alignment using QED-Compton events, where an electron is found in one of the BPC modules, and a balancing photon in the other module [61]. This study can be performed due to the fact that the distance between both BPC modules is fixed
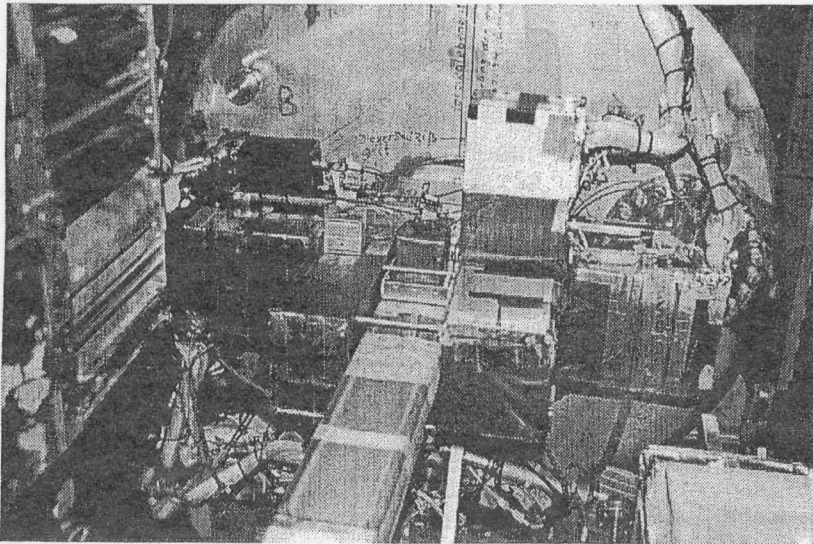
Figure 4.17: The two BPC modules after installation around the beam pipe

BPC	X_0^{BPC} (mm)	Y_0^{BPC} (mm)	Z_0^{BPC} (mm)
North	38.7	1.8	-2936.6
South	-74.7	1.4	-2936.8

Table 4.1: The BPC survey results: in the ZEUS coordinate system, X_0^{BPC} is the X displacement, from the origin, of the edge of the BPC closest to the beam, Y_0^{BPC} the Y displacement of the center of the face of the BPC, and Z_0^{BPC} the Z displacement of the BPC front face.

within 0.1 mm by four brass distance bars at the four corners of the module's face. The absolute position of the face of the calorimeters is known to 0.5 mm. The tilt between the BPC longitudinal axis and the horizontal plane is tuned to 6 mrad, matching the tilt between the nominal beam axis and the horizontal axis in ZEUS.

4.2.7   Readout electronics

The BPC uses the same readout electronics as the main ZEUS calorimeter, which takes phototube signals as input, and provides for charge and time as output. The readout system performs the following steps (for details refer to the ZEUS detector status report [103, 20]):

- shapes and amplifies the PMT signal;
- samples the signal in 96 ns intervals and stores the samples in a pipeline;
- buffers triggered events;
- digitizes the pulse samples;
- reconstructs the energy and time of the event.

The electronics for the BPC is physically split into *Analog Cards*, which are located close to the detector, in an area accessible only during maintenance breaks in the HERA machine, and the *Digital Cards*, sitting in the *Rucksack*, the main electronics housing of the ZEUS detector, outside the limited access area.
The readout of the BPC is administered centrally by the ZEUS Calorimeter Readout Control, providing the necessary clocks and levels to the Analog Cards, memory addresses to the Digital Cards, and controlling calibration and test runs.

Analog Cards

The Analog Cards sit in an EURO crate and each receives signals from 12 PMT's, through approximately 5 m of coaxial cable; they perform the first three functions listed above. After sampling, the pulse area can be derived from a weighted sum of the samples, while the time measurement is provided by ratios of samples. The cards are designed so that its calibration can take place *in-situ*, with a on-card precision charge injector connected to the input of each channel.

Digital Cards

The Digital Cards reside in VME crates, outside the ZEUS detector, ~ 50 m of cable away from the Analog Cards. Each one processes signals from 24 PMT's, digitizing the signal from the Analog Card, and, with the help of an on-board Digital Signal Processor (DSP), performs calculations based on the information from the samples and the stored calibration constants.

The BPC readout electronics, together with the main electronics from the main ZEUS calorimeter, is calibrated on a regular basis: programmable precision DC voltage and charge injection are used to measure gains and linearity and absolute charge scale of the readout. Test runs are performed daily, with a major *full electronics calibration* every week. Details on the tools available to monitor and calibrate the readout electronics, which is stable at a level of 0.1%, are given in [103].

The dynamic range of the readout was fixed by adjusting the PMT voltages so that the output from a PMT that saturates the electronics corresponds roughly to the maximum energy deposited in a single channel by an incoming electron of 35 GeV. After the analysis of the first sample of data collected by the detector some fine tuning was performed.

4.2.8   Trigger electronics

The task of the BPC First Level Trigger is to tag scattered electrons contained in the signal regions [10] of the BPC modules at a time compatible with an *ep* collision. Since the background which come in time with scattered electrons is expected to decrease as the energy increases (for example π^0s misidentified as the scattered electron), an energy threshold is required: this has to be a compromise between rejecting as much background as possible, and still being fully efficient for low energy electrons (10 GeV).

In the scheme adopted [84], this energy threshold is defined in terms of simple analog sums of several detector channels. For the BPC North (and South) these sums are defined as follows:

- NORTH (SOUTH) VERTICAL SUM: $N(S)V = \sum_{i=2}^{10(6)} N(S)X_i$

- NORTH (SOUTH) HORIZONTAL SUM: $N(S)H = \sum_{i=3}^{14} N(S)Y_i$

- NORTH (SOUTH) OUTER SUM: $N(S)O = \sum_{i=11(7)}^{15(11)} N(S)X_i + N(S)Y_1 + N(S)_2 + N(S)Y_{15} + N(S)Y_{16}$

- NORTH (SOUTH) INNER SUM: $N(S)I = N(S)X_1$

- NORTH (SOUTH) BACK TILE SUM: $N(S)B = \sum_{i=1}^{2} N(S)B_i$.

These sums are performed in six *Trigger Summing Card*, located close to the BPC Analog Cards, in a NIM crate. The charge coming from each PMT is split off, with $\sim 10\%$ taken by the trigger node, and the remaining going into the Analog Card. The BPC North energy signals (vertical and horizontal sums) are digitized using a four bit Flash Analog

---

[10]Signal regions are the areas that can be reached by electrons originating in an *ep* interaction and traversing the low-mass windows of the beam pipe.

to Digital Converter (FADC) while the calorimeter vetoes (North outer and inner sums) are digitized with only two bit accuracy. The remaining energy sums, on the veto tiles and the BPC South module, are tested against a maximum and a minimum threshold, using discriminators. The digitized energies, together with the timing digitized by fast Time to Digital Converters (TDC) of the signal regions, and the discriminator bits are passed to the ZEUS GFLT (for details refer to [96]). At the GFLT the above quantities and bits can be used to perform arithmetic and logical operations, allowing different first level trigger configurations (see appendix B). In 1995 no BPC information was used at the second or third level trigger.

4.3   First tests of the detector

4.3.1   Cobalt scans

After the construction of both BPC modules, they were scanned with a radioactive ^{60}Co source.

This procedure has several purposes:

- To ensure that every scintillator layer, in all BPC channels, shows a signal when energy is deposited.

- To allow a first (rough) equalization of the response of each BPC channel.

- To be used as a reference when compared to similar scans after the data taking in ZEUS, for aging and radiation damage investigations.
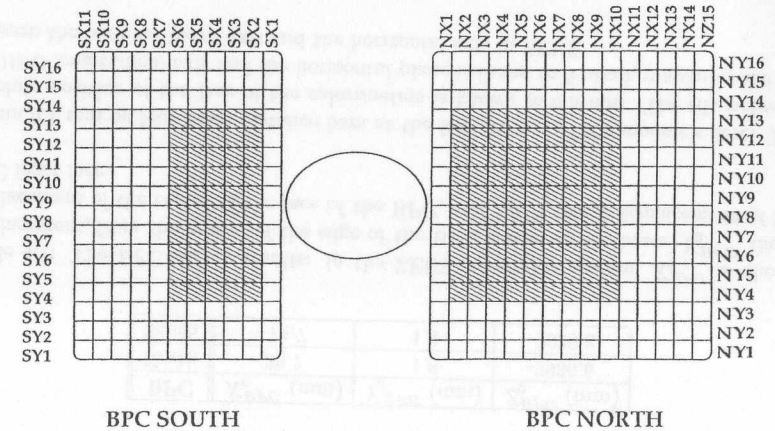
Figure 4.18: A schematic drawing of the BPC and its trigger regions.

The method consists in sliding the radioactive source along the mirrored end of each of the calorimeter channels, in the Z direction, while reading out the response of the calorimeter (integrated over some milliseconds).

The radioactive source is encapsulated inside a steel hull, which is hard soldered to a steel wire. This wire is moved mechanically by a stepper motor, controlling the source position. By means of a special plastic frame, attached to the face of the BPC, the wire is guided and the source movement is kept parallel to the scintillator fingers, at a constant distance from the detector.

As the source moves, from the back to the front of the calorimeter, the output from the corresponding channel is sampled.

The data acquisition is done through a PC, equipped with ADC cards, and dedicated software, performing an online pedestal correction, and storing the amplitude of each PMT signal versus the source position. Further details on the source scan procedure and data analysis can be found in [66].

Figure 4.19 shows the response of a BPC channel as the source moves from the back of the calorimeter to the front.

The variations of the signal correspond to the layer structure of the BPC: the response is maximal when the source is positioned in front of a scintillator finger, and decreases in
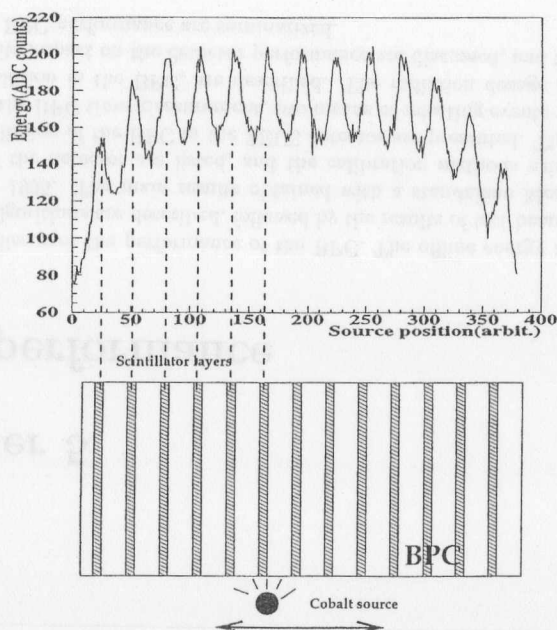
Figure 4.19: Schematics of the BPC cobalt scan.

front of the tungsten plates. If all the couplings are correct, thirteen peaks should be seen per channel, corresponding to the thirteen X (or Y) scintillator layers of the calorimeter (the lower amplitude observed for the first and last peaks is due to geometrical effects).

The average amplitude of the output signal for each channel is proportional to the energy response of that channel, and hence, by equalizing the output of the source scan, the responses of each channel to the same incident particle are also equalized.

The source scan results, together with the photomultiplier database mentioned in previously and some simple software tools, allow the adjustment of the PMT operating voltages, either to equalize response of all channels, or to scale, as whole, the response of the detector [11].

---

[11]Because of the slightly different geometries of the setup for X and Y scans, the average response of the X strips is not necessarily the same of the Y strips, even after equalization, but the difference should be small enough so that a fine tuning calibration can be performed offline

Chapter 5

BPC performance

This chapter discusses the performance of the BPC. The offline energy and position reconstruction algorithms are described, followed by the results of test beam measurements made in early 1995. The main results obtained with a standalone Monte Carlo (MC) simulations of the detector are listed, and the calibration methods using physics data after the installation of the BPC in the ZEUS detector are presented. The electron identification and the BPC time measurement, two means of selecting events with an electron from an ep collision in the BPC, are described. The radiation dosage accumulated by the BPC and its impact on the detector performance are discussed, and finally, the main results on the BPC performance are summarized.

5.1 Energy and position determination

5.1.1 Energy reconstruction

Regardless of the method adopted to reconstruct the BPC energy, there are three factors which affect the transverse uniformity of the energy response of the calorimeter:

- Differences in calibration from channel to channel (arising, for example, from different optical couplings, uneven polishing, wrapping or aluminization of the fingers, and different PMT responses).

- Due to the attenuation length of the scintillator fingers, the response to the same signal in a strip varies according to the distance of the impact position from the WLS readout.

- Close to the edges of the calorimeter the shower will not be fully contained.

Keeping in mind that the BPC consists of two independent readout schemes, with the scintillator fingers positioned along the X and Y direction, providing two independent energy measurements E_{TotX} and E_{TotY}, the energy of a particle impinging on the BPC is reconstructed according to the following method:

- The energy deposited in each strip is corrected with the respective strip-to-strip calibration constant, accounting for differences in the response of the individual channels.

- According to the X (Y) hit position, the attenuation suffered by the signals propagating through the scintillator fingers is estimated, and the overall Y (X) energy corrected for this effect.

- Depending on the distance in X and Y of the impact position to the edges of the calorimeter, a correction for energy leakage is introduced.

- The energy of a certain number of strips ($Ncluster$) in X is summed. Similarly, the energy of $Ncluster$ Y strips is summed. These two results are added and their sum is corrected by the absolute energy calibration scale, yielding the reconstructed energy of the incident particle, E_{Tot}.

This can be summarized as

$$E_{Tot} = S \cdot (E_{TotX} + E_{TotY}) \tag{5.1}$$

$$E_{TotX} = \sum_{Ncluster} C_X(i) \cdot E_X(i) \cdot ATTcor_X(Y) \cdot LEAKcor(X) \tag{5.2}$$

$$E_{TotY} = \sum_{Ncluster} C_Y(i) \cdot E_Y(i) \cdot ATTcor_Y(X) \cdot LEAKcor(X) \tag{5.3}$$

where

- E_{Tot} is the total, corrected, energy of a particle hitting the BPC.

- S is the absolute energy correction factors.

- The index $Ncluster$ specifies that each sum runs over a number $Ncluster$ of adjacent strips, surrounding the strip in X (Y) where the event position is reconstructed (see following section on position reconstruction) [1].

- $C_X(i)$ and $C_Y(i)$ are the strip to strip relative calibration constants.

- $E_X(i)$ and $E_Y(i)$ the energies measured in each finger.

- $ATTcor_Y$ and $ATTcor_X$ are correction functions for the attenuation of the signals along the scintillator fingers: these corrections are different for X and Y fingers due to their different lengths. The attenuation correction for the energy in X depends only on the Y impact position, since the X fingers run vertically, and conversely for the Y fingers.

- $LEAKcor$, the leakage correction, is the same for both views, and, while in general it is a function of both X and Y impact positions, in practice depends only on X, since in the vertical direction the fiducial region is far enough from both edges of the detector, covering, approximately, the central 6 cm of the 13.4 cm length of each finger (see, for example, figure 5.11).

---

[1]In practice the results are equivalent if, instead of using the strip corresponding to the hit position, the cluster is built around the most energetic strip.

The determination of the relative calibration constants and correction functions mentioned above and of S are described in section 5.4.1.

The cluster size $Ncluster$ chosen is a compromise between two factors:

- The number of strips included in the sum should be large enough so that the algorithm is not too sensitive to the impact position of the particle inside a strip. This is illustrated with the limit case, where only one strip would be used to determine the energy: events hitting the center of this strip would deposit in it much more energy than events hitting its edge, giving rise to big non-uniformities inside a strip.

  A large number of strips should also improve the resolution of the measurement.

- The number of strips included in the sum should be small enough so that the same algorithm can be used over as wide a portion of the fiducial region as possible. If the strip where the position is reconstructed is closer to the edge of the calorimeter than the number of neighboring strips to be included in the sum, the algorithm is distorted, giving rise to extra non-uniformities along the calorimeter, and increasing the importance of the transverse leakage.

The issue of the non-uniformity within a strip can be investigated, in a qualitative way, with a little 'toy model' [2]:

- The transverse shower shape $f(X) = \left(\frac{dE}{dX}\right)$, is parameterized as a sum of two exponential functions (the exact parameters are irrelevant for a qualitative interpretation of the results), with the maximum at a position X_0 (see figure 5.1 i))

$$f(X) = e^{(-|X-X_0|/R_1)} + p_2 . e^{(-|X-X_0|/R_2)} \qquad (5.4)$$

- To simulate the BPC strip readout, the shower impact position X_0 is chosen to be inside 'strip X8'. Then, the shower profile is integrated, around the center of strip X8, over 8-2δ mm wide intervals (corresponding to the 8 mm BPC strips, where $2\delta \simeq 0.1$ mm is the gap between two consecutive fingers), separated by gaps of 2δ mm; the results of these integrations correspond to the energies deposited in each of the calorimeter strips (the shaded area in figure 5.1 i) shows, as an example, the deposit $E_X(6)$)

$$E_X(i) = \int_{X(i)-(4-\delta)}^{X(i)+(4-\delta)} f(X)dX \qquad (5.5)$$

where $X(i)$ is the coordinate of the center of strip Xi.

- The energy reconstruction algorithm 5.1 is applied to the quantities determined in this fashion.

---

[2]Throughout this chapter, whenever the variables corresponding to the X and Y strips of the BPC are treated in an equivalent way, only the case for X is presented.

- The same calculation is repeated, in steps, with the shower maximum X_0 moving from the center of strip X8 to its edge (the results are symmetric around the center of the strip, so only half a strip is 'scanned').

- The previous exercise is repeated, using various cluster sizes in the reconstruction algorithm.

The results of these investigations are presented in figure 5.1 iii): the energy reconstructed for clusters of three, four, five, six and seven strips, normalized to the energy at $X_0 = 0$, is shown versus the shower position X_0 in a strip ($X_0 = 0$ mm is the center of the strip, $X_0 = 4$ mm its edge).

It can be seen that the non-uniformity within a finger is large for $Ncluster$=3, as expected, and that it decreases if more strips are included in the reconstruction. Clusters including an even or odd number of strips show a different shape. The interesting feature, however, is that, in general, clusters including an even number of strips perform better than those
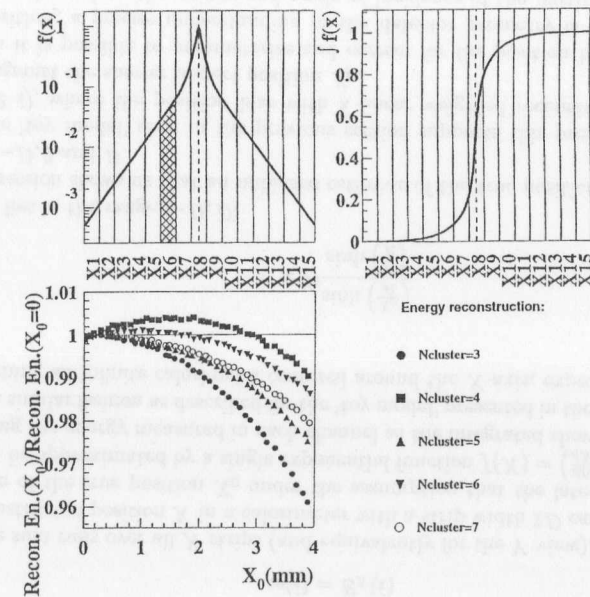
Figure 5.1: 'Toy model' for BPC reconstruction: i) The (normalized) shower shape $f(X) = \frac{dE}{dX}$ and ii) the integrated energy $\int f(X) = E(X)$ (normalized to $E(X = \infty)$), for an impact position X_0 in the center of strip X8; iii) Reconstructed energy (normalized to the reconstructed energy at $X_0 = 0$), for different algorithms, a function of the impact position X_0 inside a strip. $X_0 = 0$ denotes the center of a strip, and $X_0 = 4$ mm its edge.

including an odd number [3]: the non-uniformity inside a strip is smaller for $Ncluster=4$ than for $Ncluster=5$, and comparable for $Ncluster=4$ and $Ncluster=7$.

In addition it can be seen that the improvement in the uniformity from a four strip algorithm to a six strip one is small.

The number of strips included in the cluster is also an important factor in the reliability and stability of the strip-to-strip calibration described in section 5.4.1. This affects the reliability of the calibration in the sense that accurate strip-to-strip constants can only be determined within the fiducial volume of the BPC. Cluster algorithms involving a very large number of strips imply that more strips outside this region have be included in the sum. The stability of the constants was tested varying the cluster size and re-doing the calibration, as well as testing it in separate samples and comparing results. Also here it was found that even cluster sizes perform better than odd ones.

The discussion presented above has motivated the use of $Ncluster = 4$ in the reconstruction algorithm. In addition, it has been verified using the Monte Carlo simulations described in section 5.3 that the energy resolution achieved with this choice is not worse than that achieved when more strips are included.

The cluster is defined as the strip where the particle position is reconstructed, its two adjacent strips, and the most energetic of its second-order neighbors.

5.1.2 Position reconstruction

Due to the fine segmentation of the BPC, it is possible to reconstruct the impact position of the scattered electrons in this detector with high accuracy.

The ideal position reconstruction algorithm is the one in which both the position resolution and the bias between the reconstructed and the real impact positions in the BPC are optimized. Typically, algorithms tuned to improve one of these aspects, degrade the other, and a compromise has to be achieved between the reconstructed position resolution and the bias.

Two approaches are discussed below: the use of a simple linear weighting position reconstruction method, and a *log weighting* method with an effective energy *cutoff* which reduces the impact of shower fluctuations and controls the importance of the tails of the shower.

The logarithmic weighted method has been chosen to reconstruct the BPC impact position.

Linear weighting method

The most obvious position reconstruction algorithm to use in a finely segmented device is to calculate the center of gravity of the shower as a sum of the central positions of each readout channel $X(i)$, weighted by the corresponding measured energy $E_X(i)$ (method 1)

---

[3]A quantitative description of both the ratio of reconstructed energy to total energy and of the size of the non-uniformities for each of the algorithms cannot be extracted from this 'toy model', as these strongly depend on the precise shower parameters. However, the fraction of the energy measured by the clustering algorithm is not an important variable in this study since an absolute energy calibration is performed for any chosen algorithm. As for the relative behavior of the non-uniformity from one algorithm to the other, it has been checked that it is not sensitive to reasonable variations of $f(X)$.

$$X = \frac{\sum_X w(i)X(i)}{\sum_X w_i} \tag{5.6}$$

$$w(i) = E_X(i) \tag{5.7}$$

where the sum runs over all X strips (and equivalently for the Y view).

The reconstructed position X in a calorimeter with a strip width $2D$ can be expressed as a function of the true position X_0 under the assumption that the lateral shower profile $f(X)$ can be approximated by a single exponential function $f(X) = \left(\frac{dE}{dX}\right) \propto e^{(-|X-X_0|)/R}$. Calculating the energy measured in each channel as the integrated shower profile in that strip, in a similar fashion as described for the 'toy model' presented in the previous section, and assuming an infinite calorimeter centered around the X-axis, expression 5.6 reduces to

$$X = D\frac{\sinh\left(\frac{X_0}{R}\right)}{\sinh\left(\frac{D}{R}\right)} \tag{5.8}$$

where X lies in the range $[-D, D]$

This expression shows us that an unbiased estimate of the true position is only achieved for $X = -D, 0$ and D.

The same 'toy model' used in the previous section supports this prediction, as seen if figure 5.2 *i)*, where the position bias with a linear weighted reconstruction method is plotted against the shower impact position X_0.

Although it is possible to parameterize and correct for the position bias obtained with this algorithm, a precise understanding of the detector geometry is required, and the corrections depend on the energy and angle of incidence of the particle in the detector [1].

Log weighting method

Alternative position reconstructions methods have been developed which instead of weighting each strip's position with its energy, use the logarithm of the energy, trying to take into account the exponential falloff of the shower profile [4] [6].

The center of gravity of the shower is still reconstructed using expression 5.6, but the weights $w(i)$ are given by (method 2)

$$w(i) = \max(0, [w_0 + \ln(\frac{E_X(i)}{E_{XTot}})]) \tag{5.9}$$

w_0 is a dimensionless parameter, defining the minimum fractional energy in a strip required for that strip to be included in the position calculation, and it provides a way of controlling the importance of the shower tails. In the present case it takes the value 2.8, corresponding to a strip threshold of roughly 6% of the total shower energy.

---

[4]The fact that the shower shape is actually a more complicated function than a single exponential hardly affects the performance of these methods.

If w_0 is too small, a few central strips dominate the calculation, and the bias in the reconstructed position is big. On the other hand, as $w_0 \to \infty$, all strips are weighted equally, and the reconstructed position is the center of the detector.

For reasonable values of w_0, the bias in the estimated position decreases for larger w_0.

Position reconstruction:

Linear weighting   **Log. weighting (w01 < w02 < w03)**
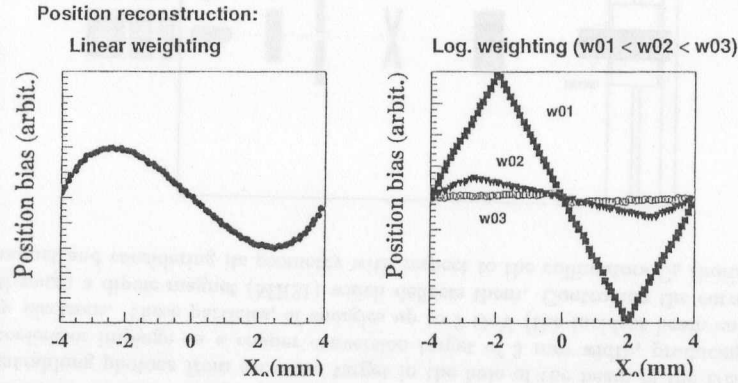
Figure 5.2: 'Toy model' for BPC reconstruction: qualitative behavior of the bias in the position reconstruction with $i)$ a linear weighting method and $ii)$ with logarithmic weights. The vertical scale is in arbitrary units.
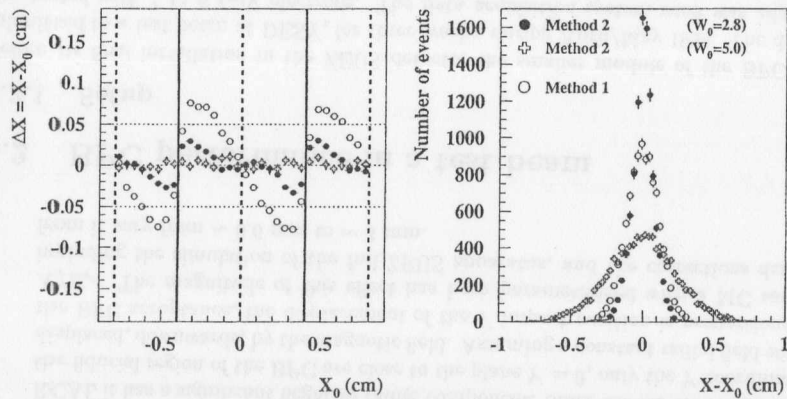
Figure 5.3: $i)$ Position bias and $ii)$ position spectra using different values of the parameter w_0 in the position algorithm, from an EGS4 simulation of 10 GeV electrons(from [96]).

This is shown in figure 5.2 $ii)$, where the position bias is plotted against the shower impact position X_0 for three different values of w_0 [5].

As w_0 increases, the improvements in the position bias are traded for a slow worsening of the resolution. The determination of the optimal w_0 value is therefore a compromise to keep both the position bias and resolution at acceptable levels.

The choice of $w_0 = 2.8$ is based on studies performed with a 10 GeV and a 25 GeV EGS4 MC samples (see section 5.3), where the dependence of the position bias and resolution was investigated for different values of w_0. Details on this study can be found in [96]. Figure 5.3 shows a comparison of the results obtained with a linear weighting method and with a log writhed method with $w_0 = 5.0$ and $w_0 = 2.8$. The last choice optimizes the resolution of the measurement, while keeping the bias well within 0.5 mm.

This position reconstruction method has also the advantage that the effects of the shower fluctuations are damped by the logarithmic function.

Corrections to the measured position

Two corrections are applied to the X and Y impact positions determined via the log weighting reconstruction method described above:

- The first correction arises due to the fact that the electrons do not enter the BPC at an angle of 90°. Since the energy of the particle is deposited in the calorimeter at some 'effective depth', the reconstructed positions are only unbiased at that same depth, and have to be extrapolated back to the front face of the detector. The corrected X and Y positions at the face of the BPC are given by

$$X' = X \frac{\Delta Z}{S + \Delta Z} \tag{5.10}$$

$$Y' = Y \frac{\Delta Z}{S + \Delta Z} \tag{5.11}$$

where S is the 'effective depth' at which the energy is deposited in the BPC, and ΔZ is the longitudinal distance between the ep interaction vertex and the front face of the BPC, Z_0^{BPC}.

ΔZ and S are determined on an event by event basis. If no Z vertex measurement is available for an event, the mean Z vertex position of that run is taken. S has been parameterized as a logarithmic function of the electron energy (see t_{max} given in section 4.1), and is always of the order of 5 cm (corresponding, in radiation length to $\sim 7X_0$).

- The second correction to be applied to the reconstructed position is due to the fact that the scattered electron travels through a non-zero magnetic field from the interaction point to the BPC. In the central part of the ZEUS detector the field, from the ZEUS central magnet, is parallel to the Z-axis, but just in front of the

---

[5]Once again, the exact dimensions of the position bias for each method depend on the precise parameterization used, and cannot be extracted from this simple model.

RCAL it has a significant negative radial component. Since the electrons that reach the fiducial region of the BPC are close to the plane $Y = 0$, only the Y coordinate is displaced, downwards, by the magnetic field. Assuming a constant radial field within the BPC acceptance, the displacement of the Y impact position is proportional to $X/E_{e'}$. The magnitude of this effect has been parameterized with a MC sample including the simulation of the full ZEUS apparatus, and the corrections derived from it vary from ~ 0.6 mm to ~ 3 mm.

5.2 BPC performance in a test beam

5.2.1 Setup

Before its final installation in the ZEUS detector the smaller module of the BPC was submitted to a test beam at DESY, for three weeks, during April/May 1994. The device was tested with 1 to 6 GeV electrons. The data acquisition system used was adapted from that used in the studies of the photomultiplier tubes: it consists of CAMAC ADCs, interfaced by a VME-based OS9 processor. It allows the simultaneous readout of all BPC PMT's, and stores the response of each calorimeter channel on an event-by-even basis in a simple ASCII data file. The setup is shown in figure 5.4.

The electrons available on the test beam are produced through the following scheme: bremsstrahlung photons from a carbon target in the halo of the beam of the DESY II pre-accelerator impinge on a copper conversion target of 3 mm width, producing secondary electrons. These particles, of energies up to 7 GeV (the incident beam energy), pass through a dipole magnet (MR21) which deflects them. Controlling the current in the magnet and considering its geometry with respect to the collimators C_h (horizontal
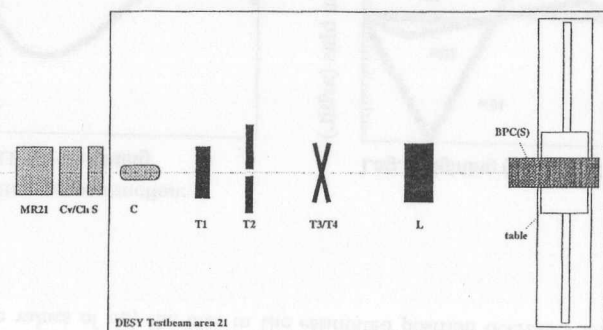
Figure 5.4: A schematic view of the trigger and detector setup used in the BPC test beam.

opening) and C_v (vertical opening), remotely controlled, one can select the energy of the electrons accepted by the final setup. After the collimators there is a beam shutter (S) and a further collimator (C).

The trigger setup consisted of a 5×20 cm^2 scintillator pad (T1), a veto counter (T2) which is a 20×30 cm^2 scintillator tile with a hole in its center of 3 cm diameter, and a 1 cm wide horizontal and vertical strip counters (T3 and T4). The signals of T1, T2, T3 and T4 are sent to NIM discriminators. The beam trigger is defined as a coincidence of T1, T3 and T4, in anti-coincidence with T2, and it enables the readout by the ADC. The gate width (100ns) was adjusted so that it contains more than 99% of the calorimeter signal.

Just in front of the BPC module there is a set of scintillator counters, referred to as LUMI counters (L), consisting of four horizontal adjacent strips and four vertical adjacent strips, each 2.6 mm wide. These strips, which provide information on the electron impact position, are read out and can be used offline for event selection, for example in the position resolution studies.

The BPC module is positioned on the top of a remotely controllable movable table. This table can be moved independently in the horizontal and vertical directions to a precision of 0.1 mm^2, although its absolute position cannot be accurately determined.

A collimator scan was performed, varying the opening between 1×1 mm^2 to 5×5 mm^2. Since no effect was seen in the energy resolution, the widest opening was chosen to maximize the data taking rate.

5.2.2 Data sets

During the test beam period the following data samples were collected:

- Uniformity scan: 10K events were taken at the center of each X and each Y BPC strip, with the beam energy set to 3 GeV. This data set allows the study of the variations in response from channel to channel, as well as the attenuation length along the scintillator.

- Energy scan: With the beam positioned in the center of the face of the detector (interception of strips SX5 and SY8), the energy was varied between 1 and 6 GeV, in 1 GeV steps. This data set allows the study of the energy resolution and linearity of the BPC.

- Fiducial edge scan: The beam position was scanned from the edge towards the center of the detector, in steps of 1 or 2 mm, at a fixed energy of 3 GeV. This data set allows the study of the energy and position measurements close to the edge of the calorimeter.

The pedestal of the ADCs was determined before each run with random triggers (while the beam shutter is closed) and several LED monitor triggers were taken through the test beam period, confirming the PMT stability. In addition, the test beam average PMT HV was lowered once from 850 V to 700 V, and the expected change in the calorimeter response was observed.

5.2.3   Results

The energy of the test beam data, in ADC counts, is calculated from the expression 5.1, with the energy measured in each strip subtracted by the the corresponding pedestal, and S set to unity. The leakage and attenuation, and the strip to strip corrections used are discussed in the following.

The position reconstruction of the test beam data is performed according to equation 5.6, with logarithmic weights.

The BPC uniformity and strip to strip calibration

While the signal attenuation and the energy leakage are fully corrected offline, the initial channel to channel corrections were determined by the source scan (described in section 4.3.1), and the PMT voltages adjusted individually so that an uniformity at a level of 10% was reached.

This initial strip to strip calibration can be refined using the test beam data, in particular the data taken with the beam position in the center of each X and Y strips, for a fixed
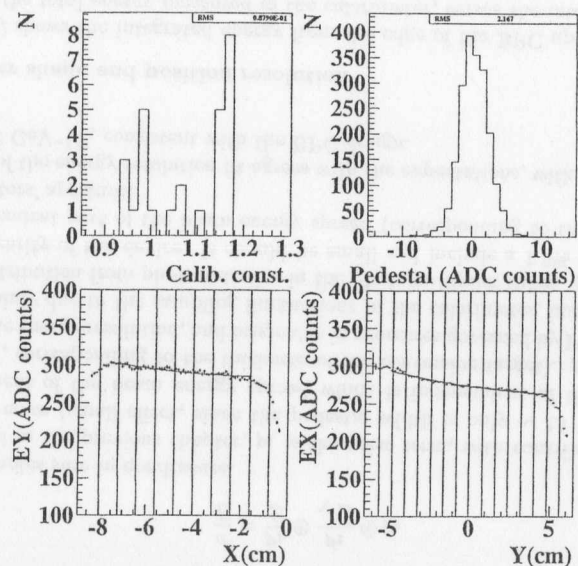
beam energy [6]. The method used for the strip-to-strip calibration is described in section 5.4.1, and its result is a set of constants $C_X(i)$ and $C_Y(i)$ by which the test beam energies measured in each strip should be multiplied.

Figure 5.5 shows a distribution of the test beam calibration constants, normalized to unity, indicating that the initial uniformity achieved by tuning the PMT HV is at a level of $\sim 9\%$. Also shown is the distribution of the sum of the ADC pedestal of all BPC channels for a day of running: the total width corresponds to (roughly) only 15 MeV. Although the pedestal values varied throughout the three weeks of running (within 100 MeV) due to hardware instabilities, this does not affect the analysis since the pedestal values used were measured just before each of the data runs.

The attenuation and leakage effects are illustrated in figure 5.5.

Figure 5.5 *iii)* shows the energy measured in the Y strips, before corrections, for a fixed vertical incident position, as the horizontal beam position varies ($X=0$: inner edge of the BPC, X=-9.4 cm: coupling to WLS), and figure 5.5 *iv)* shows the energy measured in the X strips, before corrections, for a scan of the Y impact position ($Y=0$: center of the BPC, Y=-7.0 cm: coupling to WLS), at fixed X .

In both plots one can see the attenuation of the signal due to the distance of the impact position to the WLS readout, superimposed to the signal degradation close to the edges of the detector, due to leakage. The corrections for these effects are determined through fits to the data (the fit to the attenuation length can be seen in the figures), and have similar functional form for both test beam data and data collected after the installation in the ZEUS detector; their parameterization is discussed is section 5.4.1.

The energy resolution and linearity studies

Figure 5.6 shows the BPC energy spectrum after pedestal subtraction, in ADC counts, for a beam energy of 3 GeV.

The BPC response as a function of energy is obtained by fitting the measured distribution at each beam energy with a Gaussian function and plotting the resulting mean versus the nominal beam energy (in GeV), as shown in figure 5.7*i)*.

A linear fit ($p_1 + p_2.E_{beam}$) between 2 and 6 GeV gives a good description of the BPC response as a function of energy, with a linearity better than 1% for energies greater than 2 GeV. Figure 5.7*ii)* shows the deviation of the measured energies from the linear fit.

There are two remarks to this fit: first, it does not pass through the origin and second, the non-linearity at 1 GeV is at the level of 8%. Similar effects have been observed in the test beam of another ZEUS component (the '8 m tagger'), which took place immediately after the BPC data taking. Since this device has a different design and used other readout electronics than the BPC, it is suggested that the observed effects are due to a miscalibration of the nominal beam energy. This possibility has been confirmed by the DESY machine group. Therefore, in the following, the 1 GeV data set is ignored, the offset in the response corrected.

The fractional energy resolution versus beam energy is presented in figure 5.7*iii)*. It is

Figure 5.5: *i)* BPC calibration constants; *ii)* Pedestal spread; *iii)* and *iv)* Attenuation length and leakage effects in the BPC, as a function of the reconstructed impact position.

---

[6]The relative calibration constants determined from the test beam data are to be used only in the test beam reconstruction and not in the physics data, as the detector installation, and the use of a different readout scheme and HV power supplies can affect the channel to channel performance.

well described by the following parameterization

$$\frac{\sigma}{E} = \frac{p_1}{E} \oplus \frac{p_2}{\sqrt{E}} \oplus p_3 \qquad (5.12)$$

where $\oplus$ denotes sum in quadrature.

As discussed in the previous chapter, p_1 is the noise term, with contributions from the electronics' noise (small effect, since the pedestal width is only ~ 15 MeV) and from the component of the beam energy spread which is independent of the beam energy (~ 100 MeV, corresponding to the thickness of the conversion target). p_2 is expected to dominate the energy resolution, and originates in processes governed by Poisson statistics. It arises mainly due to the sampling fluctuations in the calorimeter, but it also includes a small contribution from photostatistics in the photomultiplier tubes. p_3 is sensitive to the non-linearity of the device. It should be small and include a 1-2% term due to the energy dependent part of the beam energy spread (corresponding to the finite width of the collimators' aperture).

The result of the energy resolution fit agrees with the expectations, with a sampling term of $17\%/\sqrt{E}$ GeV$^{-1/2}$, consistent with the BPC design.

The shower shape and position resolution

Figure 5.8i) shows the integrated energy from the edge of the BPC up to limit X, normalized to the total energy measured in the calorimeter, versus the integration limit X, $\int_{-\infty}^{X} \frac{dE}{dx}dx / \int_{-\infty}^{+\infty} \frac{dE}{dx}dx$, with $X = 0$ cm being the nominal beam position.
It is a nice picture of the integrated shower profile $E(X)$ in the calorimeter, and helps in qualitatively understanding the shape of the energy leakage close to the edges of the device.

The shower profile shown can be well parameterized as the sum of exponential functions [100]. Unfortunately any parameter determined by such a fit cannot be applied in the leakage correction due to the fact that at the very edge of the BPC there is a tungsten bar which affects the shower shape, making it preferably to parameterize the leakage as a function of the impact position directly from data taken at the edge of the calorimeter, as described in section 5.4.1.

Figure 5.8ii) shows the reconstructed electron position for a 5 GeV beam energy. The data has been selected requiring that one and only one of the central LUMI counters shows a hit. This restricts the impact position to within the width of a counter, 2.6 mm. A fit of the reconstructed position by a Gaussian profile yields a width of 1.7 mm. Correcting this value for the contribution of the finite beam width ($2.6/\sqrt{12} = 0.75$ mm) the BPC position resolution for a 5 GeV electron is determined to be 1.5 mm.

The BPC response close to its edges

The results of the BPC fiducial scan, after attenuation, leakage and strip to strip corrections, are presented in figure 5.9. The ability to accurately parameterize and correct for these effects is a factor to take into account when defining the limits of the BPC fiducial

Figure 5.6: i) BPC response to 1-6 GeV electrons; ii) Gaussian fit to the 3 GeV spectrum.
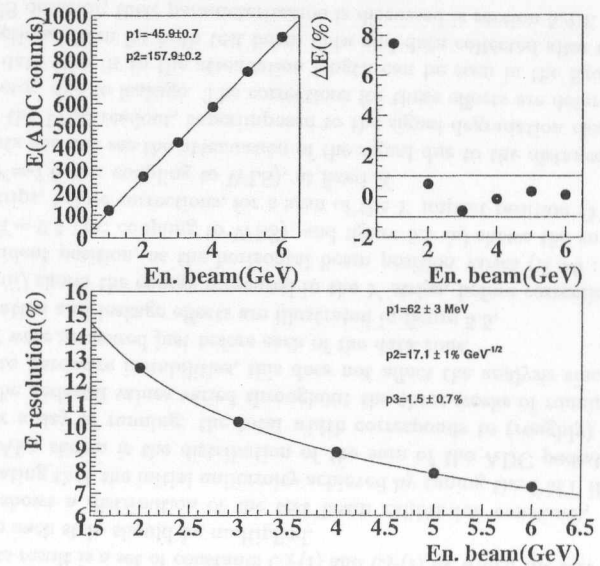
Figure 5.7: i) Linearity and ii) energy resolution of the BPC.

area.

The energy, energy resolution and position measurements are presented as a function of the beam impact position, in a region close to the edge of the calorimeter ($X = 0$: inner edge of the BPC).

Figure 5.9 *i)* shows that the energy measurement of the BPC is fairly constant up to impact positions in the first strip of the detector (SX1).

The energy resolution (figure 5.9 *ii)*, in the same fashion, is stable if one restricts the studies to 8 or more millimeters (i.e., one strip) away from the edge. Beyond that limit, the energy resolution degrades since the fluctuations in the transverse shower profile become important, and the energy deposited in the detector is smaller.

Figure *iii)* displays a very good linear correlation between the reconstructed impact position and the *true* beam position [7], but also in this case the agreement is only good more

[7]Since the accuracy on the absolute position of the BPC in the test beam is rather limited, offsets in figure 5.9 *iii)* are not significant.
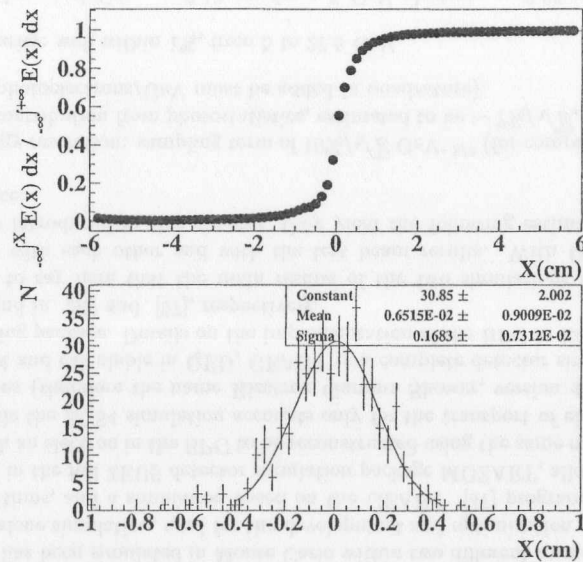
Figure 5.8: *i)* Integrated energy from the edge of the BPC up to limit X, normalized to the total energy measured in the calorimeter, versus the integration limit X, with the nominal beam position at $X = 0$ cm. *ii)* Reconstructed impact position in the BPC, where the nominal beam position is at $X = 0$ cm, giving the BPC position resolution (convoluted with beam spread), for 5 GeV electrons.

than 8 mm away from the inner edge of BPC.

These studies show that the fiducial region of the detector can be extended up to one strip away from the edge of the calorimeter.

5.2.4   Conclusions from the test beam studies

The results of the BPC under the DESY test beam prove that the calorimeter, its optical readout and photomultiplier tubes perform well, and that the method for setting the individual PMT HV allows the channel to channel response to be equalized to within 10%.

The test beam data proved to be a very good sample on which to test and develop reconstruction and detector calibration techniques.

In addition, the detector shows energy and position resolutions compatible with the expectations (the energy resolution is dominated by the sampling term of $17\%/\sqrt{E}$ GeV$^{-1/2}$, and the position resolution at 5 GeV is at a level of 1.5 mm), and its linearity from 2 to 6 GeV is found to be better than 1%.

The test beam results also demonstrate that the BPC fiducial region can be extended up
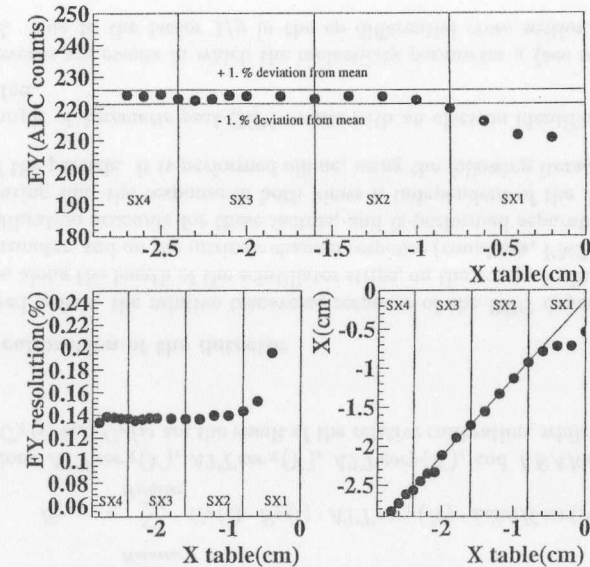
Figure 5.9: *i)* Energy response, *ii)* energy resolution and *iii)* position determination close to the edge of the BPC (reconstructed position versus position of the table).

to 8 mm away from its edge.

5.3   BPC simulation

The BPC has been simulated in Monte Carlo within two different frameworks: an EGS4 [77] standalone simulation, used for the development and optimization of the reconstruction algorithms, and a simulation based on the GEANT [47] program. The latter was integrated in the full ZEUS detector simulation package MOZART, allowing MC physics events with an electron in the BPC to be reconstructed using the same method as used for data. While the EGS4 simulation accounts only for the transport of electrons/positrons and photons (therefore the name Electron Gamma Shower, version 4) using processes understood and calculable in QED, GEANT is a complete detector simulation and particle tracking package. Details on the implementation of the BPC in EGS4 and GEANT can be found in [96] and [97], respectively.

It suffices to say here that the main results of the two simulations are in very good agreement with each other and with the test beam results. With the reconstruction algorithms introduced in this chapter, they yield the following estimates for the BPC performance:

- Energy resolution: sampling term of $16\%/\sqrt{E}$ GeV$^{-1/2}$ (for comparisons with data, the contribution from photostatistics, estimated to be $\sim 7\%/\sqrt{E}$, corresponding to 200 photoelectrons/GeV must be added in quadrature).

- Linearity: well within 1%, from 5 to 27.5 GeV.

- Position resolution: ~ 0.13 cm for a 5 GeV electron, ~ 0.05 cm for a 25 GeV electron,.

- Position bias: less than 0.05 cm.

- Transverse shower containment: 8 mm (one strip) away from the edge of the calorimeter, the shower is more than 95% contained.

5.4   BPC performance in ZEUS

5.4.1   Calibration of the detector

The calibration of the calorimeter can be separated into the strip to strip relative calibration and the absolute energy calibration, which sets the overall energy scale. These two steps are performed sequentially and result in the set of corrections to be applied to the measured energies on an event-by-event basis.

The expressions for the energy reconstruction, introduced in section 5.1.1 reflect this procedure

$$E_{Tot} = S \cdot (E_{TotX} + E_{TotY}), \qquad (5.13)$$

$$E_{TotX} = \sum_{Ncluster} C_X(i) \cdot E_X(i) \cdot ATTcor_X(Y) \cdot LEAKcor(X), \qquad (5.14)$$

$$E_{TotY} = \sum_{Ncluster} C_Y(i) \cdot E_Y(i) \cdot ATTcor_Y(X) \cdot LEAKcor(X). \qquad (5.15)$$

The functions $ATTcor_X(Y)$, $ATTcor_X(Y)$, $ATTcor_Y(X)$, and $LEAKcor(X)$, plus the constants $C_X(i)$ and $C_Y(i)$ are the result of the relative calibration, while S is an absolute scale.

Relative calibration of the detector

As described before, the relative transverse response of the BPC depends on the light attenuation along the length of the scintillator strips, on the energy leakage near the edge of the calorimeter, and on the intrinsic channel response (couplings, PMT, HV, etc.). The relative calibration accounts for these factors, and is performed separately for X and Y strips, ensuring that the response in both views is independent of the X and Y impact position of the particle. It is performed offline, using the following iterative procedure:

- A sample of *kinematic peak* (KP) events with an electron identified in the BPC is selected.

   KP events are events in which the inelasticity parameter y (see section 2) is very small. Due to the factor $1/y$ in the ep differential cross section, the number of
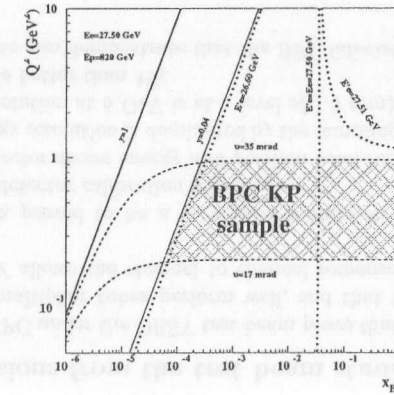
Figure 5.10: The BPC $x - Q^2$ plane, with the kinematic peak region shaded. The dashed lines are lines of constant scattering angle $\vartheta_{e'} = \pi - \theta_{e'} = 17$ mrad and 35 mrad, limiting the BPC fiducial volume. The dotted lines are lines of constant energy of the scattered electron, and the solid lines denote the kinematic limit $y = 1$ and the selection cut $y \leq 0.04$.

events peaks in this region. When a maximum y cut is imposed on the data and an electron is required in the BPC the energy of the scattered electron is very close to the electron beam energy, as shown in figure 5.10.

The KP were selected applying a cut of $y_{JB} < 0.04$ [8], requiring conservation of energy and momentum in the event, a good vertex position, timing information from the main calorimeter and from BPC compatible with an ep interaction, a reconstructed vertex in the tracking system, shower width cuts on BPC (see 6.2.3) and a tight fiducial cut on the impact position.

The mean energy of the KP events should be constant over the whole fiducial region of the BPC to within one part in 10^4 [97].

Figure 5.11 shows the distribution of the KP events in the front face of the BPC: the outer edges of the fiducial region selected were determined by the projection onto the BPC face of the beam pipe exit widows and the lower X cut was fixed by the requirement that the electron shower is reasonably contained in the detector, and that the impact position of the particle is well reconstructed (see previous section.)

Figure 5.13 shows the energy measured in both views of the BPC (X and Y), versus the X and Y impact positions of the KP electrons within the fiducial region of the BPC. The relevant views are shown at each stage of the relative calibration procedure (raw energies, energies after attenuation correction, after attenuation and leakage corrections, and final distributions, including strip to strip factors). Each

---

[8]In this selection, the y variable is reconstructed via the so called *Jacquet-Blondel* (JB) method [63], where only the hadronic final state variables (energy E_h and momentum along Z p_{Zh}) are used: $y_{JB} = \frac{E_h - p_{Zh}}{2E_e}$. In the KP region this method provides a much better resolution than the reconstruction of y using the electron variables.
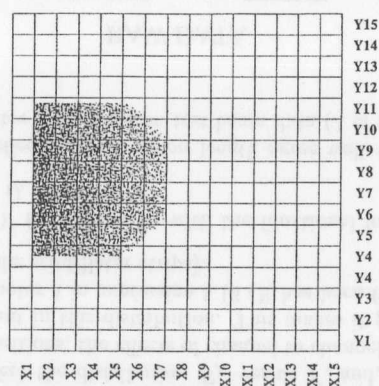
Figure 5.11: The distribution of the KP events in the BPC face, after impact position cuts.

of the four projections (E_X versus X , E_X versus Y, E_Y versus X and E_Y versus Y) is sensitive to different non-uniformity sources, allowing the attenuation, leakage and strip-to-strip corrections to be decoupled and extracted directly from the KP data. This figure should help to understand the calibration procedure described in the following.

- The first step of the calibration is to correct the energy measurement for the effects of the attenuation of the signals within each finger. The scintillation light produced by a shower can reach the WLS through two paths, either directly into the WLS bar, or traveling in the opposite direction, and then reflected back by the aluminized end of the finger. The light reaching the WLS is well parameterized by the formula

$$I = I_0(.e^{-\frac{\Delta X}{\lambda}} + R.(e^{\frac{2L - \Delta X}{\lambda}})) \qquad (5.16)$$

where ΔX is the distance between the electron impact position and the end of the scintillator strips coupled to the WLS, R is the reflection coefficient, L is the scintillator length and λ is an 'effective attenuation length'.
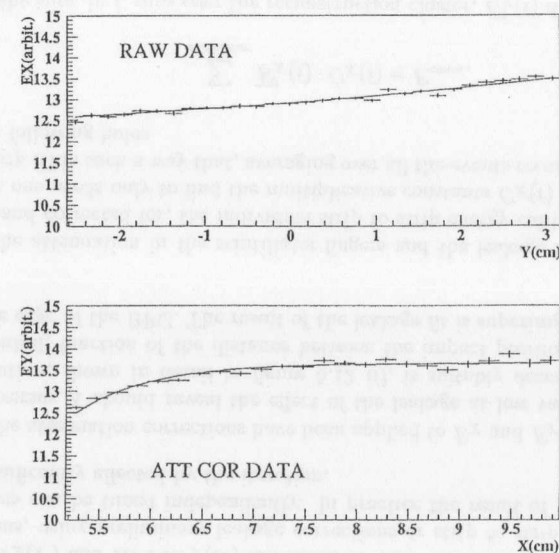
Figure 5.12: Detail on the *i)* attenuation and *ii)* leakage parameterizations determined in the relative calibration of the BPC with KP events.

Due to the restricted fiducial volume in the Y direction, the transverse shower leakage does not affect the distribution E_X versus Y, and, since E_X is averaged over all X impact positions, the effects of channel to channel variations in response are also not significant in this distribution. This makes it particularly suitable to determine the parameter λ in expression 5.16 (R has been fixed to 0.85, according to bench studies of the scintillator strips).

A fit to E_X versus Y for KP events with the functional form presented above is shown in figure 5.12 *i)*.

The results of the effective attenuation length agree well with those obtained in scans of the scintillator strips, and on test beam data (λ of the order of 25-30 cm).

RAW DATA

ATT COR DATA

ATT+LKG COR DATA

ATT+LKG+STR COR DATA (final)
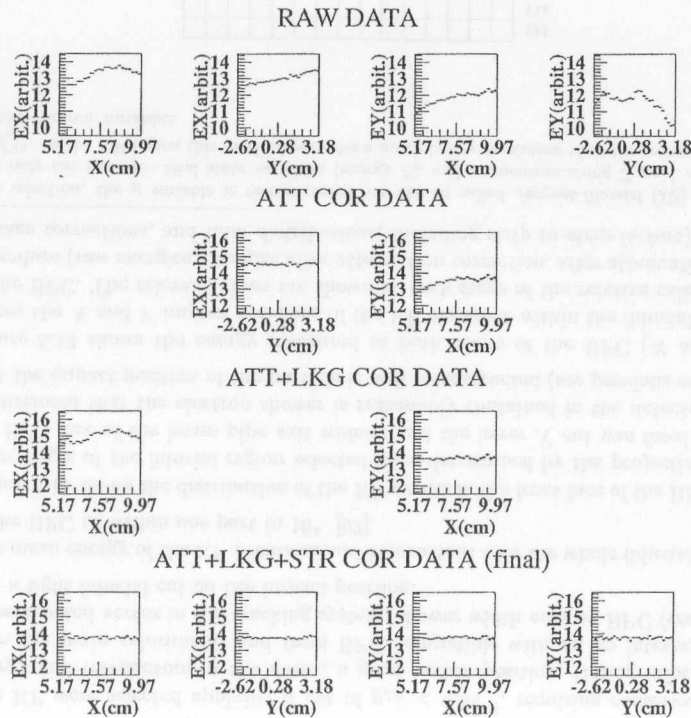
Figure 5.13: The stages of the relative calibration of the BPC with KP events. The views affected by each calibration step are shown.

The resulting corrections to E_X and E_Y, due to attenuation effects vary between 0% and 7%, depending on the impact position of the particle. In the first iteration, $ATTcor_X(Y)$ and $ATTcor_Y(X)$ are taken to have the same form. In subsequent iterations, using preliminary leakage corrections or strip to strip constants, these functions can be tuned independently. In practice the result of the calibration is not significantly affected by the iteration.

- After the attenuation corrections have been applied to E_X and E_Y, the distribution of E_Y versus X should reveal the effect of the leakage at low values of X . This distribution, shown in detail in figure 5.12 *ii)*, is suitably described by a single exponential, function of the distance between the impact position of the electron and the edge of the BPC. The result of the leakage fit is superimposed to the data points.

- Once the attenuation in the scintillator fingers and the leakage have been understood, and corrected for, the individual strip to strip energy calibration method is simple: one needs only to find the multiplicative constants $C_X(i)$ to be assigned to each strip Xi in such a way that, averaging over all the events reconstructed on strip Xj, the following holds

$$\sum_{Ncluster} \overline{E}_X^j(i) \cdot C_X(i) = E_{const}, \qquad (5.17)$$

where the sum, in i, runs over the reconstruction cluster, $E_X^j(i)$ denotes the energy measured in strip i for an event whose position is within strip j and E_{const} is the same constant regardless of the index j.

The constant E_{cont} is, for simplicity, set to half the electron beam energy, since this is a good approximation to the expected energy in each view for KP events. However, due to kinematic cuts and radiative corrections, the average energy of the KP sample is somewhat lower than E_e. This is accounted for in the absolute energy calibration.

The last expression can be written in a matrix form

$$\overline{E}_X^{ji} \cdot C_X^i = 13.75 \qquad (5.18)$$

and the linear system can be solved inverting the matrix $\overline{E}_X^{ji}$. In practice, the index j runs over only the strips in the fiducial volume of the BPC, and the calibration constants of strips outside this volume are set, at each iteration, to the average value of the constants determined. This nominal setting was varied for stability studies, and found to be a sensible choice.

Once a complete set of corrections is available, the position of each event in the calibration sample is re-calculated, and the procedure iterated. This is necessary because if one strip has an energy response very different from the its neighbors, it can bias the position reconstruction. However, these effects turn out to be very small, and the calibration

method converges very quickly: two or three iterations guarantee that the results are stable to 1%.

The final results of the relative calibration are displayed in figures 5.14 and 5.15: in the first one, the reconstructed energy versus *i)* X and *ii)* Y impact positions are shown, and found constant throughout the detector at a level of $\sim 0.5\%$. The second plot shows the deviation, in percent, from 27.5 GeV, of the reconstructed mean energy in each 8×8 mm^2 $X - Y$ bin of the detector.

It should be noted that, due to the method of calibration, the corrections to be applied are consistent only if the energy algorithm described above is used.

Absolute energy calibration

The absolute energy calibration was determined with elastic ρ^0 events ($ep \rightarrow e\rho^0(\pi^+\pi^-)p$), in which the electron energy measured in the BPC is required to 'match' the energy of the hadronic system reconstructed in the main detector.

The selection of ρ^0 events is discussed in detail in chapter 6.

For an event in which no particles escape undetected through the rear beampipe, the
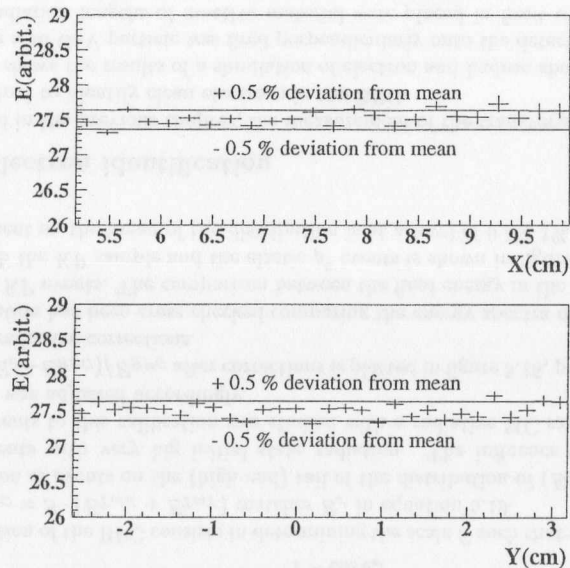
Figure 5.14: Final uniformity achieved after BPC calibration: reconstructed energy versus *i)* X and *ii)* Y impact position.

quantity $E - p_Z \equiv \sum_i E_i - \sum_i p_{Z_i}$, where E_i and p_{Z_i} are the energy and the momentum component along the Z-axis of the energy deposits in the ZEUS calorimeter and BPC, equals two times the incoming electron energy.

In this case, and assuming no initial state radiation (see section 7.1.2),

	X1	X2	X3	X4	X5	X6	X7	X8	
									Y13
	0.98	0.34	0.04	-0.47	-0.56				Y12
	0.22	-0.15	-0.17	-0.4	0.15	0.59			Y11
	-0.03	-0.07	-0.27	-0.07	0.13	0.16			Y10
	-0.22	-0.07	-0.12	0.3	-0.47	0.62			Y9
	-0.36	-0.47	0.24	0.48	0.77	0.01			Y8
	-0.65	-0.18	-0.16	0.27	0.64	1.2			Y7
	-0.53	0.2	0.6	0.46	0.86	-0.77			Y6
	0.61	0.05	-0.41	-0.25	0.03				Y5
									Y4

Figure 5.15: Deviation of the reconstructed mean energy in each $X - Y$ bin from the reconstructed mean over the whole region for KP events, in percent.
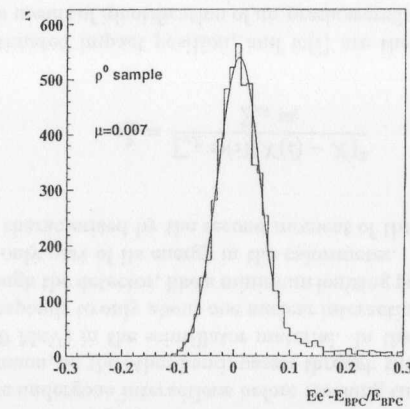
Figure 5.16: The absolute calibration with ρ^0 events: $(E_{e'} - E_{BPC})/E_{BPC}$ (see text) after calibration.

$$E_{e'} = \frac{2E_e - (E - p_z)_{\pi^+} - (E - p_z)_{\pi^-}}{1 - \cos\theta_{e'}}. \tag{5.19}$$

The calibration of the BPC consists in determining the scale S such that the reconstructed energy $E_{BPC} = S \cdot (E_{TotX} + E_{TotY})$ matches $E_{e'}$ in equation 5.19.

The exclusion of events on the (high end) tail of the distribution of $(E_{e'} - E_{BPC})/E_{BPC}$ removes events with very big initial state radiation. The influence of the remaining radiative events to this calibration was studied with a radiative MC sample (see chapter 7.5), and S was adjusted accordingly.

The ratio $(E_{e'} - E_{BPC})/E_{BPC}$ after corrections is plotted in figure 5.16, peaking at $\sim 0.7\%$, due to the radiative corrections.

This calibration has been cross checked comparing the energy spectra of data and MC in a sample of KP events. The comparison between the final energy in the BPC in data and MC for both the KP sample and the elastic ρ^0 events is shown in figure 5.17. The agreement on the mean of the distribution is at a level of 0.5%-1%.

5.4.2 Electron identification

As discussed in the previous chapter, the measurement of the transverse shower profile is a powerful tool to identify clean electrons in the BPC.

Figure 5.18 shows the results of a simulation of electron and hadron showers in the BPC. In each case a 10 GeV particle was fired perpendicularly onto the detector, and, in figure *ii)*, three radiation lengths of inactive material were placed in front of the detector, at a distance of 50 cm. The development of the shower and the transverse shower profile are quite different from case to case: clean electrons that enter the BPC without passing
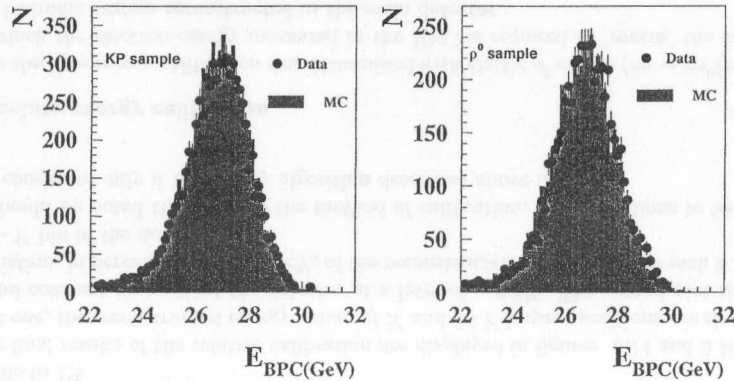
Figure 5.17: Comparison of the BPC energy in data and Monte Carlo (Standard Model plus ZEUS simulation) for *i) kinematic peak* events and *ii)* ρ^0 events.

through any inactive material produce a narrow transverse shower, while electromagnetic particles which have undergone interactions before reaching the calorimeter show a much broader profile. A muon, on the other hand, passes through the BPC depositing only very little energy (~ 300 MeV) in the scintillator material. In the case of hadronic showers, since the BPC corresponds to only about one nuclear interaction length, the hadron either passes straight through the detector, like a minimum ionizing particle, or will start a broad shower, depositing only part of its energy in the calorimeter.

The shower width, characterized by the second moment of the shower distribution

$$\sigma_X^2 = \frac{\sum_X w(i)(X(i) - X)^2}{\sum_X w_i} \tag{5.20}$$

where X is the estimated impact position, and $w(i)$ are the weights described in section 5.1.2, is used as means of identification of un-preshowered electrons (and equivalently for the Y view).

As for the position reconstruction, the use of the log weighting technique reduces the bias on σ_X, improving the ability to separate hadron and preshowered electrons from clean ones. For an optimum e/h separation the value of the parameter w_0 need not be the same as the value that optimizes the position resolution (according to the results of [6], larger values of w_0 are required to optimize the electron/pion separation than the position reconstruction). However, for simplicity, this parameter was kept at w_0=2.8 (value used in the position reconstruction) also in this calculation, without significant loss of performance.

A large discrepancy is seen when the expression given above for the shower width is used in KP data and in a MC sample of KP events with an electron in the BPC see figure 5.19. The transverse energy distribution is narrower in MC than in data and this discrepancy is seen both in the X and Y views. [9] If the shower width parameter is to be used is selection cuts, its correct reproduction in the MC is important, since it is via this simulation that the efficiency of the cut is estimated. A possible explanation for such an effect is the existence of cross-talk between neighboring channels of the BPC, either at the level of the coupling between scintillator and WLS, or at the level of the trigger summing card (this last possibility seems rather remote, as the card was explicitly designed to minimize this effect). If the MC strip energies are reweighted, on an event by event basis, such that a few percent of the light of each scintillator finger are allocated to the strips that surround it, the shower width of the MC can be made to agree well enough with that of the data (see reweighted MC in figure 5.19).

A cut of $\sigma_X < 0.7$ cm and $\sigma_Y < 0.7$ cm is applied to select good electrons. This cut keeps the electron acceptance close to 100%, without increasing the background significantly, as discussed in section 6.2.3.

---

[9] On the average, the values of σ_X are slightly larger than those of σ_Y. This results from the fact that the incidence of particles in the BPC is not perpendicular to the detector, with a wider angle in the horizontal plane than in the vertical one.

5.4.3 Timing reconstruction

In addition to the energy information, the BPC readout system provides a timing measurement per energy deposit, per strip. The time of passage of a particle is reconstructed
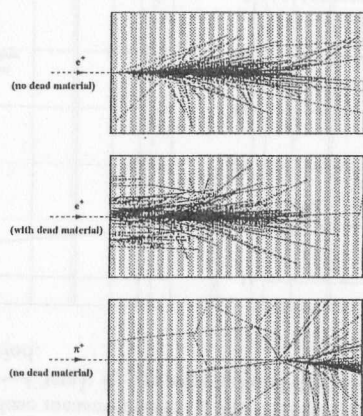
Figure 5.18: GEANT simulation of the shower tracks inside the BPC for: *i)* an incoming electron, directly hitting the BPC; *ii)* an incoming electron, hitting the BPC after three radiation lengths; *iii)* an incoming pion. The white areas correspond to the scintillator material, while the shaded areas denote the tungsten plates.
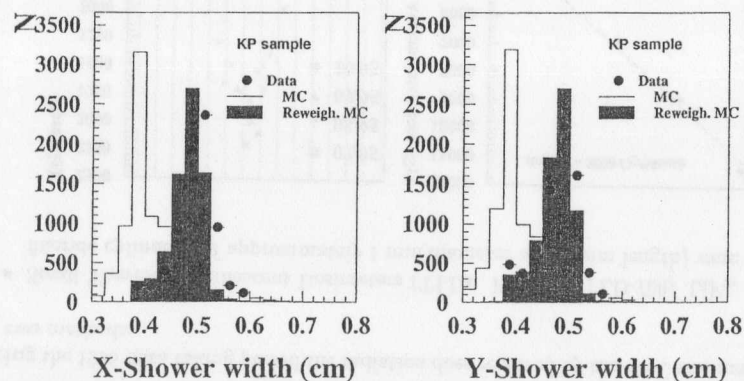
Figure 5.19: Comparison of the BPC shower width in data and Monte Carlo (Standard Model plus ZEUS simulation) for *kinematic peak* events: *i)* X-shower width; *ii)* Y-shower width.

offline as the (linear) weighted mean of the timing information of each strip in the BPC, $t_X(i)$ and $t_Y(i)$

$$t = \frac{\sum_X E_X(i).t_X(i) + \sum_Y E_Y(i).t_Y(i)}{\sum_X E_X(i) + \sum_Y E_Y(i)} \tag{5.21}$$

where the sums run over all X and Y strips in the detector. The absolute value of the reconstructed time depends on the signal cable length and, *per se*, contains little information. However, the difference between each event's time and the mean time of a sample of good electrons in a run is a powerful event selection tool. The timing resolution of the detector is found to be better than 0.5 ns.

A timing distribution for a selected sample of good BPC electrons is shown in figure 5.20. The BPC timing signals are also used to to supply online timing and vertex information to the ZEUS shift crew. Details on this feature are given in appendix A.

5.4.4 BPC performance during 1995

Bremsstrahlung background

Shortly after the installation of the BPC in ZEUS it was found that electrons which loose energy through bremsstrahlung and, therefore, deviate from the nominal electron orbit were a significant background in the BPC. These events, which are in time with respect to electrons scattered in an *ep* collision, have an energy spectrum that peaks at about half of the electron beam energy, and their rate could be reduced by a factor 100 with the adjustment of the movable ZEUS beam collimators, bringing it to an acceptable level.
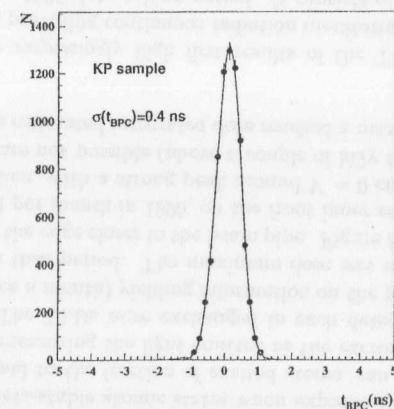
Figure 5.20: Time distribution around the mean reconstructed BPC time for kinematic peak events (the mean value is determined by the length of the signal cables.)

Radiation damage

During the 1995 data taking period the radiation dose received by the BPC was monitored via two methods:

- Small Thermo-Luminescent Dosimeters (TLDs: Harshaw TLD-700/ LiF$_2$, lithium fluoride cylinders, of approximately 1 mm diameter and 5 mm length) were stacked
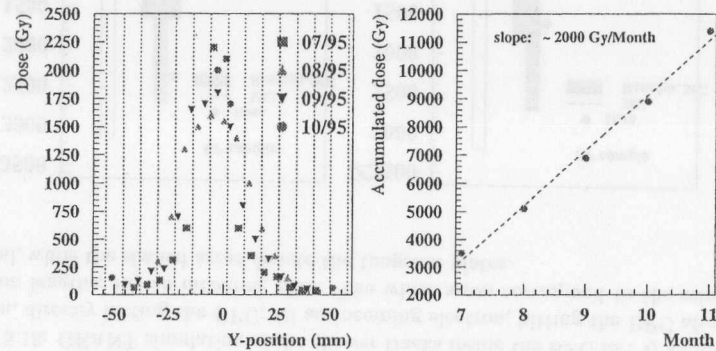
Figure 5.21: Radiation dose measurements: *i)* the dose profile along the Y direction, in the front inner edge ($X \sim 4.3cm$); *ii)* the accumulated dose at $Y \sim 0, X \sim 4.3cm$ during the 1995 data taking period.
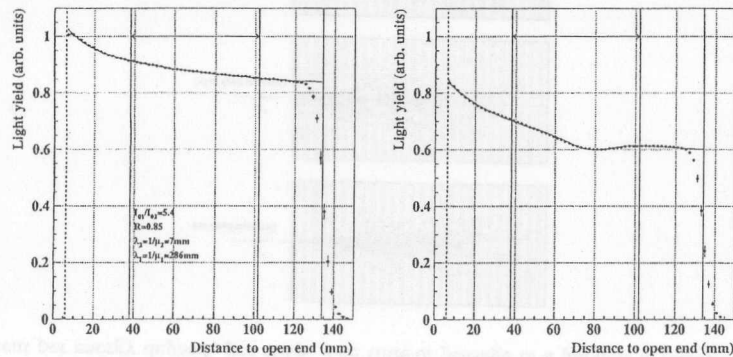
Figure 5.22: The effect of the radiation damage on the scintillator response: scan of a X scintillator finger (see section 4.2.1) of the 7th BPC active layer before *i)* and after *ii)* the 1995 data taking period. (The normalization of the two plots has been done to different references; only the shape of the response should be compared. From [96]).

inside vertical brass tubes, mounted along the four corners of the BPC. This substance forms meta-stable atomic states when exposed to radiation. The absorbed dose, proportional to the fraction of excited atoms, can be determined by heating the TLDs and measuring the light emitted as the excited atoms come back to the ground level. The TLDs were exchanged in each detector maintenance day (approximately once a month) yielding information on the profile of the radiation dose accumulated in that period. The maximum dose was received in the front of the calorimeter, on the edge closer to the beam pipe. Figure 5.21 shows the approximate doses deposited per month in 1995, on the front inner edge of the calorimeter, versus the Y position, with a strong peak around $Y = 0$ cm. Although accurate dose measurements are not possible (above a couple of kGy the TLD response becomes non-linear), the estimated integrated dose reached a maximum of approximately 12 kGy.

- In view of the surprisingly high first results of the TLD dose measurements, a second system, providing continuous radiation monitoring, was installed during the final part of the 1995 data taking period. It consists of silicon photodiodes which generate a current proportional to the flux of radiation received. These diodes have been calibrated with a ^{137}Cs source, but a strong temperature dependence of the current and annealing effects complicate the detailed understanding of this measurement. However, the measurements revealed that most of the dose received by the BPC originated in positron dumps. The positron dumping procedure has, since then, been improved by the HERA group.

The results of a second cobalt scan of the BPC North module, after the 1995 data taking period, showed that the scintillator material was damaged, particularly the scintillator strips closest to the beam, at central Y positions. Since this module of the calorimeter was rebuilt for the 1996 HERA run, the scintillator fingers could be scanned on a bench, and compared to results of non-damaged samples. It was found that the amount of light yield loss is maximum approximately at the shower maximum ($\sim$ seventh active layer), consistent with a flux of high energy electromagnetic particles.

The response of the scintillator material to the scans before and after data taking was parameterized as

$$I(X) = I_{01}(e^{-\Delta X/\lambda_1} + Re^{(2L-\Delta X)/\lambda_1} + I_{02}e^{-\Delta X/\lambda_2}) \qquad (5.22)$$

where ΔX is the distance to the open end of the finger, and L is its total length. This ansatz is similar to equation 5.16, but the region of the measurement and its higher precision allow the introduction of a term corresponding a very short attenuation length. The effect of the radiation damage can be described by a loss of light yield plus a change of the attenuation length of the material. Details on the finger scans and on the parameterizations used to describe their results can be found in [96].

The results of the scans of the individual fingers after radiation damage has been simulated in EGS4 MC [96]. For energies above $\sim$ 7.5 GeV, and after accounting for the overall light reduction using the calibration method described, the response deviates less than 1% from the non-damaged one. Above 15 GeV the disagreement is smaller than 0.5%.

In order to correct for the decrease of the BPC response due to radiation damage, the 1995 data set was divided into four run ranges and the detector calibration was performed independently for each of them. This procedure was enough to guarantee that the absolute energy scale of the BPC is accurate to 0.5% over the whole run range, although the uncorrected mean energy from KP peak events dropped, during the year, by about 2%.

5.5 Conclusions on the detector characteristics and performance

The design described in the previous chapter resulted in a calorimeter with the following characteristics (supported by testbeam results and Monte Carlo simulations):

- The BPC corresponds to a total length of $\sim 24X_0$, enough to contain longitudinally more than 99.5% of a shower initiated by a 27.5 GeV electron.

- The Molière radius of the detector is circa 13 mm.

- The energy sampling fraction of the BPC for electrons is approximately 4%.

- The detector position and alignment are known to 0.5 mm (section 4.2.6).

- The fiducial area of the BPC covers angles from 17 to 35 mrad. At the lowest angle, corresponding to impact positions 8 mm away from the edge of the detector, the shower containment is better than 95% (sections 4.2.6 and 5.2.3).

- In the fiducial region the energy resolution of the BPC has the stochastic term $\sim \frac{17\%}{\sqrt{E}}$ GeV$^{-1/2}$ (sections 5.2.3 and 5.3).

- In the fiducial region, the position resolution of the BPC is better than 1 mm for electron energies $E \gtrsim 10$ GeV, and the intrinsic position reconstruction bias is below 0.5 mm (sections 5.1.2, 5.2.3 and 5.3). The absolute position of the detector is known to 0.5 mm.

- After calibration, the BPC is uniform within $\pm 0.5\%$ (section 5.4.1). The detector is linear within 1% (sections 5.2.3 and 5.3).

- The BPC absolute energy scale is known to $\pm 0.5\%$. (section 5.4.1).

- The timing resolution of the detector is better than 0.5 ns (section 5.4.3).

- During 1995 the BPC accumulated a radiation dose of approximately 12 kGy at a distance of approximately 4.3 cm to the beam. The calibration procedure was developed such that the performance characteristics listed above were maintained during the 1995 data taking.

Chapter 6

Event selection and reconstruction

Elastic ρ^0 production in the reaction $ep \to e\rho^0 p$ is studied via the decay channel $\rho^0 \to \pi^+\pi^-$, which has a branching ratio of $\sim 100\%$. The main characteristics of these events are two oppositely charged tracks found in the Central Tracking Detector, a scattered electron detected in the Beam Pipe Calorimeter and no activity in the CAL, except that associated with the decay pions (see figure 6.1). In this chapter the trigger and offline cuts applied to select elastic ρ^0 events are discussed. In addition, the reconstruction of the kinematical variables from the measured quantities is presented.

6.1 Trigger logic

As described in section 3.2.6, the ZEUS trigger system consists of three levels. The trigger for ρ^0 events with a electron in the BPC can be described by the requirements which were imposed at each of these stages:

- At the first level trigger (FLT) the candidates were identified by an energy deposit in the BPC of more than ~ 6 GeV, at least one track candidate in the CTD, and no vetoes from the ZEUS veto counters (the timing information from these upstream counters is used to remove proton beam gas interactions) - This trigger is called FLT slot 32 (see appendix B).

- The second level trigger (SLT) included a restriction on the number of tracks and track segments in the CTD, and a requirement on the vertex position, if a vertex had been found. Further cuts in the calorimeter timing and timing difference between upper and lower half of BCAL allowed rejection of beam gas events (the mean calorimeter timing is calibrated to be zero for an event originating from the nominal interaction point) and cosmic or halo muons - This trigger is called SLT stream SPP6 (see appendix B).

- At the third level trigger (TLT) the full event information from the ZEUS detector is available, allowing more stringent veto cuts to be applied. The selected events had two and only two tracks, pointing to the interaction region, and an event vertex within ± 66 cm of the nominal interaction point - This trigger is called TLT SPP15 (see appendix B), or, equivalently, DST bit 62.
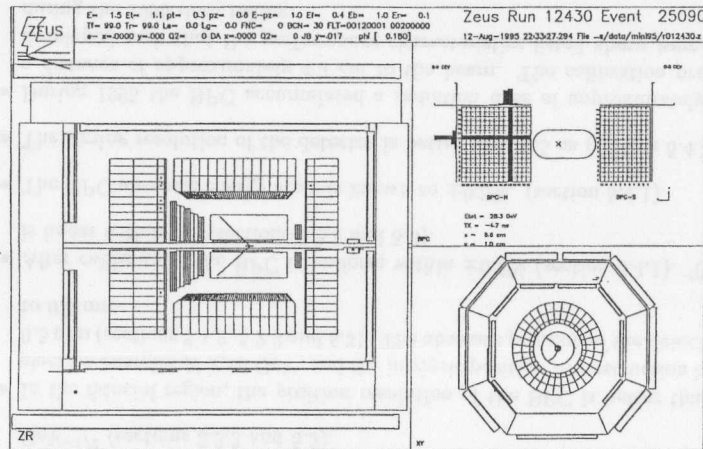
Figure 6.1: An exclusive ρ^0 event, from the data sample, displayed with the ZEUS event display LAZE (Q^2=0.59 GeV^2, W=24.0 GeV, $M_{\pi\pi}$=781.3 MeV). In the left side of the figure, one can identify in the ZEUS detector the two charged tracks reconstructed in the CTD, surrounded by no activity in the main calorimeter. The electron found in BPC is also indicated. On the upper left side of the picture, the reconstruction of the electron in BPC is shown. The lower left part of the figure shows an $X - Y$ view of ZEUS, with the reconstructed opposite charged tracks.

The efficiency of these trigger cuts is rather high, as is discussed in detail in the following chapter.

6.2 The offline selection cuts

The following conditions were required offline to obtain the final data sample, using the output of the ZEUS reconstruction software (ZEPHYR).

6.2.1 Generic cuts

- Only runs were used in which there were proton and electron beams, at nominal energies, colliding at the nominal interaction vertex.

- Only runs were used in which all relevant detector components were monitored and their status was good and stable.

- During the 1995 data taking period a hardware problem at the BPC FLT level occurred (intermittent problem with a NIM discriminator, affecting the strobe input
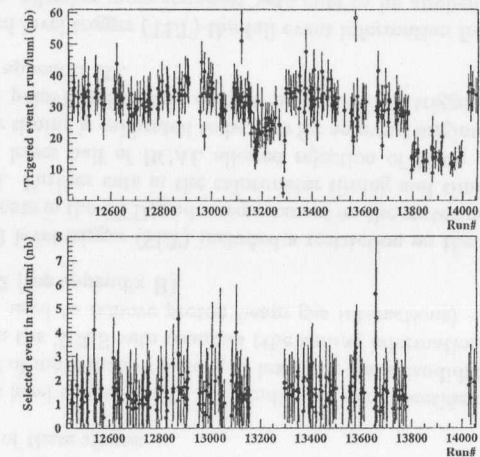
Figure 6.2: Number of events accepted per run *i)* at TLT SPP15 (DST bit 62) and *ii)* after selection cuts as a function of the respective run number, normalized to the integrated luminosity of each run. Some run ranges excluded from the analysis due to BPC FLT inefficiency can be identified.

to the BPC FLT FADC, see section 4.2.8). It resulted in a drop of efficiency of the BPC FLT for some of the runs, independent of the energy and position of the particle reaching the detector. The run ranges in which this problem affected the trigger performance more seriously were removed from the analysis. The efficiency loss in the remaining runs is discussed in the next chapter.

6.2.2 The tracking requirements

- The vertex was required to be within ±50 cm of the nominal interaction point.

- Exactly two tracks were required, both associated with the primary vertex. These tracks must have opposite charge.

- Track quality cuts were applied to restrict the measurement to a region where the detector performance is well understood and well simulated (the pseudorapidity of each track was required to be $|\eta| < 1.75$, and the minimum transverse momentum of each track $p_T > 150$ MeV).

6.2.3 The BPC electron requirements

- The timing of the electron, reconstructed in the BPC as the energy-weighted time of all channels, was required to be within 3 ns of the mean BPC timing in the corresponding run (the variation of the mean BPC timing as a function of the run number reflects the variations in the HERA *ep* bunch crossing time due to shifts of the electron and proton radio-frequencies).

- The reconstructed impact position was limited to the calibrated fiducial region of the BPC, the acceptance extending in the X direction over 6 strips starting 8mm away from the edge of the detector, and in Y over 7.5 strips, symmetrically around the center of the detector. The coordinates, in the ZEUS system, of the selected events fulfill the condition $5.17 < X_{BPC} < 9.97$ cm and $-2.82 < Y_{BPC} < 3.18$ cm, where X_{BPC} ($Y_{BPC}=$ are the horizontal (vertical) impact position reconstructed in the BPC (see section 5.1.2 for details on BPC position reconstruction and section 4.2.6 for the BPC coordinates in ZEUS.)

- A shower width cut was applied; $\sigma_X < 0.7cm$ and $\sigma_Y < 0.7cm$. This loose cut guarantees a very high efficiency for electrons, with a modest background increase. Given the energy requirement imposed (see below), the contamination by hadrons and pre-showered electrons should be minimal. The misidentification of photons cannot be reduced by means of a shower width cut [1], but given the overall event selection requirements, it should not constitute a problem.

- The energy reconstructed in the BPC (E_{BPC}) had to be bigger than 20 GeV. This cut, which does not affect non-radiative ρ^0 events (due to the kinematic coverage defined by the track requirements and BPC position, the scattered electron energy in this sample is always larger than 23 GeV, see figure 6.3), reduced the contamination of the sample by events wit an energetic initial state radiation (see section 7.1.2), and helped to reject hadronic showers and those induced by pre-showered electrons, as well as events originating from electron beam gas, synchrotron radiation and off momentum electrons. All of these processes are expected to decrease as the energy of the electron candidate increases.

- Finally, if the electron impact position was reconstructed in the second or third strips of the BPC, the event was required to have a smaller energy deposit in the first strip of the detector than in the second one. This cut rejects some rare badly reconstructed events in which the electron hits the tungsten bar at the BPC edge and, due to the wide and asymmetric shower shape, its reconstructed position is shifted with respect to the true impact. Such effect was observed in testbeam measurements and is reproduced in MC. The rate reduction due to this requirement is quite small, when applied to a sample of events that have been accepted by the remaining electron quality cuts.

---

[1]Before the 1996 data taking period, two scintillator tiles, read by photomultipliers, were placed in front of the BPC, to be used as a photon taggers.
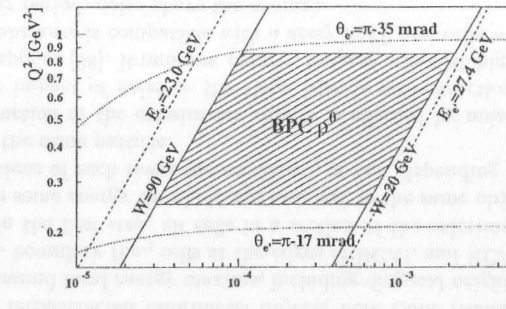
Figure 6.3: Kinematic region covered by the data sample. Indicated in the plot are lines of constant energy of the scattered electron (dashed line), constant $W_{\gamma^* p}$ (solid line) and constant electron scattering angle (dotted lines).

6.2.4 The selection of elastic events (elasticity cuts)

- An efficient cut against background, especially from inelastic ρ^0 production is a cut on the maximum energy of calorimeter objects that are not associated with the tracks of the decay pions. This is achieved by applying a *clustering* algorithm to the CAL cells, followed by a *matching* routine, associating the tracks in the CTD with the energy deposits in the calorimeter. Calorimeter clusters which have very small probability of matching one of the tracks are either caused by an outgoing particle undetected in the CTD (neutral particle, or particle with trajectory outside the CTD coverage), or by noisy cells in the detector, so that the selection criteria should be a compromise between rejecting the first while keeping the latter. In this analysis, events with unmatched calorimeter clusters (matching probability less than 1/1000) with energy in excess of 300 MeV were rejected. Details on the clustering and matching schemes, as well as on the optimization of cuts, are given in [10, 11].

- In addition to the previous cut, the requirement was imposed that the difference between the total energy in the calorimeter and the summed energy obtained from the momentum of the tracks does not exceed 2 GeV.

6.2.5 The kinematics cuts

The following cuts were also applied to the data sample (details on how to reconstruct the relevant variables follow):

- $0.6 < M_{\pi\pi} < 1.2$ GeV ($M_{\pi\pi}$ is the invariant mass of the event, obtained from the two charged tracks, and calculated assigning the pion mass to each track),

Cut	# events accepted(% of initial sample)
Trigger and run range	123380 (100)
Vertex and 2 opp. charged tracks	94251 (76)
$\|\eta\| < 1.75$	57900 (47)
$p_T > 150$ MeV	49471 (40)
BPC timing, position and shower width	22335 (18)
BPC energy	20620 (17)
Elasticity cuts	8915 (7)
Mass range	7010 (6)
Q^2, W and t cuts	5462 (4)

Table 6.1: Overview of the cuts applied to selected the events, and their impact on the triggered data.
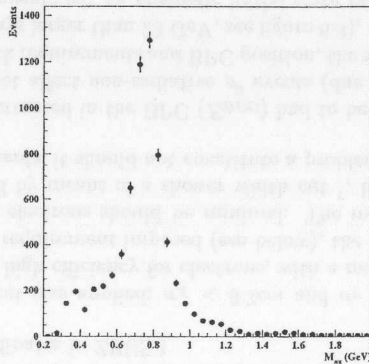
Figure 6.4: Mass spectrum after selection cuts (except for the mass cut).

- $0.25 < Q^2 < 0.85$ GeV^2,

- $20 < W_{\gamma^* p} < 90$ GeV,

- $|t| < 0.6$ GeV^2.

The hatched region in figure 6.3 displays the region in Q^2 and x ($W_{\gamma^* p}$) covered in the analysis, with superimposed lines that help to characterize the ρ^0 sample.

Table 6.1 summarizes the impact of the successive cuts applied, and figure 6.4 shows the mass spectrum of the selected data sample (except for the cut on $M_{\pi\pi}$), with a clear ρ^0 peak.

6.3 Event reconstruction

6.3.1 The CTD reconstruction

The package VCTRACK [59] was used for the offline reconstruction of the CTD tracks and the primary event vertex. The input to this program comes from the hit information of 52 axial layers in the CTD, 16 layers instrumented by Z-by-timing and 32 stereo layers and RTD hits. The pattern recognition algorithm looks for a track *seed* in an outer part of the CTD, which can either come from three CTD axial superlayer hits, or a combination of RTD and CTD hits. Given a track seed, the trajectory is extrapolated inwards, and, as more axial hits are assigned to the track, the precision of the track reconstruction increases. The hits from Z-by-timing and stereo layers is added, and eventually every track has 3D information. The program extends the tracks into the VXD and fits them to extract the vertex position. The longest tracks are reconstructed first, and then the shortest. The actual vertex fitting proceeds in three stages:

- Tracks that are incompatible with coming from the beam line are rejected.

- Remaining trajectories are fitted, and used to estimate the vertex position as a weighted center of gravity. This is an iterative process, in which tracks contributing too much to the χ^2 are removed until the quality of the fit is acceptable.

- The final complete vertex fit gives not only the vertex position, but re-evaluates the direction and curvature of the tracks constrained to it.

6.3.2 The main calorimeter reconstruction

The reconstruction of the calorimeter quantities uses as input the readout of the two PMTs connected to each cell. The energy imbalance, measured from the difference of the response between the two PMTs, is used to improve the position reconstruction. In this analysis, the reconstructed calorimeter objects were *Cone Islands* (see [10, 15]), which are clusters around local energy maxima, including diagonal neighbor cells and also those across a CAL boundary (i.e., cells at the edges of BCAL and RCAL, for example, might be joined). In the first step, all cells in a section of the calorimeter (EMC, HAC1 and HAC2) above some energy threshold are assigned to the same object. Then, in a second step, the sections of each tower are combined, or not, depending on their probability of belonging to the same particle.

The reconstruction of the calorimeter objects is affected by noise in this detector. To minimize the impact of noise in the Cone Islands reconstruction, a noise suppression procedure is applied [98]. It removes, namely, isolated cells with high energy, cells in which the energy imbalance is compatible with a noisy PMT and cells which show, throughout a long running period, noise above the average.

In this analysis the energies and position of the calorimeter Cone Islands are not used *per se*. They are only important in the process of matching calorimeter clusters to the CTD tracks.
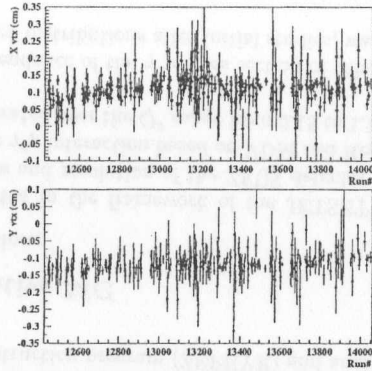
Figure 6.5: *i)* Mean X and *ii)* mean Y vertex positions averaged over a run as a function of the respective run number.

6.3.3 The BPC reconstruction

The BPC energy and position reconstruction has been described in detail in chapter 5. The electron scattering angle, with respect to the ZEUS coordinate system, is obtained from the corrected impact position in the BPC and the event vertex by simple trigonometric relations. In practice, the X and Y coordinates of the vertex used to calculate the electron scattering angle were averaged run-by-run, since the CTD resolution in these variables is ~ 1.0 mm, which is considerably larger than the spread of the HERA beam (300 μm in X, 70 μm in Y). The mean X and Y vertex positions, averaged over each run, as a function of the respective run number are shown in figure 6.5. The event-by-event Z vertex coordinate was used; it is measured, for events with at least two good tracks, with a resolution better than 5 mm.

6.4 The reconstruction of the kinematical variables

6.4.1 Influence of the beam tilt

For the accurate measurement of electrons at scattering angles close to π rad, it is necessary to investigate the tilt of the electron beam with respect to the ZEUS coordinate system. Such a tilt has a significant impact on the Q^2 and t measurement, and the formulae 2.2 and 2.7 have to be generalized to the non-collinear collision case.

It is known that the nominal proton beam orbit in ZEUS is tilted with respect to the Z coordinate of the ZEUS reference frame by $\Theta_p = 0.41$ mrad in the horizontal plane (determined by the DESY survey group). Using events with a photon measured in the ZEUS luminosity monitor LUMIG, it is possible to determine the tilt of the electron beam

with respect to the nominal proton orbit, yielding a value of $\Theta_e = -0.15$ mrad. This adds to a total tilt of the electron beam with respect to the ZEUS coordinate system of

$$\Theta_{tilt} = 0.26 \text{mrad} \tag{6.1}$$

in the horizontal plane.

The expressions used to determine Q^2 and t can be rewritten as:

$$Q^2 = 2E_e E_{e'}(1 + \cos\theta_{e'}) - 2E_e \Theta_{tilt} E_{e'} \tag{6.2}$$

$$-t = (p_X(\rho^0) + p_X(e'))^2 + (p_Y(\rho^0) + p_Y(e'))^2 + 2E_e\Theta_{tilt}(p_X(\rho^0) + p_X(e')) \tag{6.3}$$

In this analysis the momentum and scattering angle of the ρ^0 are obtained from the corresponding momentum and angles of the decay pions measured by the CTD, while the electron scattering angle was determined with the BPC. The scattered electron energy, however, was determined via a method, the so-called *constrained method*, which uses the exclusiveness of the final state. Under the hypothesis of a purely elastically produced ρ^0 and of absence of initial state radiation (see section 7.1.2), energy and momentum conservation in the collision imply:

$$E_{e'}(1 - \cos\theta_{e'}) + \sum_{i=hadrons}(E - p_z)_i = 2E_e \tag{6.4}$$

i.e.,

$$E_{e'} = \frac{2E_e - (E - p_z)_{\pi^+} - (E - p_z)_{\pi^-}}{1 - \cos\theta_{e'}} \tag{6.5}$$

The resolution in $E_{e'}$ achieved with this method, $\sigma_{E_{e'}}/E_{e'} \approx 0.002$ for the events under study, is more precise than that of the direct energy measurement with the BPC. The formulae 6.2 and 6.3 above were then used to calculate Q^2 and t.

The variable y was calculated with the so-called Jacquet-Blondel method [63], which in this case reduces to

$$y_{JB} = \frac{1}{2E_e}\left((\sqrt{m_{\pi^+}^2 + p_{\pi^+}^2} - p_{\pi^+}\cos\theta_{\pi^+}) + (\sqrt{m_{\pi^-}^2 + p_{\pi^-}^2} - p_{\pi^-}\cos\theta_{\pi^-})\right) \tag{6.6}$$

and the hadronic center of mass energy W_{γ^*p} was obtained from this by

$$W_{\gamma^*p} = \sqrt{y_{JB}s} \tag{6.7}$$

Chapter 7

Monte Carlo simulations, efficiencies and background studies

In this chapter the Monte Carlo (MC) simulation programs used to study the efficiency of the selection of the elastic ρ^0 sample as well as to understand the contamination of this sample by background events are briefly described. The results of these studies, together with supplementary background investigations, are then discussed in detail.

7.1 Monte Carlo simulation

Different MC generators were used to study the effects of efficiency and resolution of the detector, to investigate systematic uncertainties and to estimate the contribution of background events to the elastic ρ^0 sample.

Regardless of the generator used, the MC events passed through a detailed simulation of the ZEUS detector (MOZART program) and of the trigger system (ZGANA program) as well as the same reconstruction program (ZEPHYR) and analysis chain as the data.

7.1.1 Non-radiative MC

Elastic VM production:

A MC generator, written in the framework of the JETSET package [12] was used to evaluate the acceptance and resolution of the ZEUS detector for elastic ρ^0 events. This generator simulates the $\gamma^* p$ interaction based on VDM and Regge Theory (see chapter 2). These events were generated over the Q^2 range from 0.15 to 1.1 GeV^2, and the $W_{\gamma^* p}$ range from 15 to 110 GeV.

The effective $W_{\gamma^* p}$ dependence of the $\gamma^* p$ cross section of this MC sample, reweighted to agree with the measured distributions after initial studies, was $\sigma \propto W_{\gamma^* p}{}^{0.12}$.

The Q^2 dependence, also reweighted to match the data, was $\sigma \propto \left(\frac{1}{1+\frac{Q^2}{M_\rho^2}}\right)^{1.75}$ and the

t dependence was the double exponential, $\frac{d\sigma}{d|t|} = e^{-b|t|+ct^2}$ with slope parameters $b = 9$ GeV^{-2} and $c = 2$ GeV^{-4}.

The angular distribution of the decay pions were generated according to s-channel helicity conservation, and the ratio of longitudinal to transverse ρ^0 production was parameterized as

$$R = \xi^2 \frac{Q^2}{M_{\rho^0}^2}. \tag{7.1}$$

The same generator was also used to simulate elastic ω and Φ production, decaying into all known modes, and assuming the same Q^2 and $W_{\gamma^* p}$ of the $\gamma^* p$ cross section as in the ρ^0 case. These samples were used for background studies,

This MC generator does not include radiative processes, which have a small impact ($< 2\%$) in the kinematic region and process under study (see details on section 7.5).

Production of single dissociative events

To simulate proton dissociative ρ^0 events, the main background to the elastic reaction under study, the Monte Carlo generator PYTHIA [92] was used. The Q^2 and $W_{\gamma^* p}$ dependences of the $\gamma^* p$ cross section were taken to be the same as in the elastic process, and the proton dissociation was parameterized according to

$$\frac{d^2\sigma_{\gamma^* p \to \rho^0 N}}{dt dM_N^2} \propto e^{-b_{diss}|t|} F_{diss}(M_N)/M_N^2 \tag{7.2}$$

with $b_{diss} = b_0 + 2\alpha' \ln(W_{\gamma^* p}^2/M_N^2)$, with $\alpha' = 0.25$ GeV^{-2}, leading to a t slope for the full generated sample of $b_{diss} \simeq 5$ GeV^{-2}.

The function F_{diss} enhances the cross section in the low mass resonance region and suppresses the production of very large masses; in an intermediate mass region ($4 < M_N < 16$ GeV), the effective dependence of the cross section on the generated hadronic final state mass was described by

$$\frac{d\sigma_{\gamma^* p \to \rho^0 N}}{dM_N^2} \propto 1/M_N^\beta \tag{7.3}$$

with $\beta = 2.2$, as measured in diffractive $p\bar{p}$ scattering [18]. Light dissociative systems (M_N less than 1 GeV above the mass of incoming particle) decay isotropically into a two-body system; higher mass states are decayed using a string hadronization model. Only events that fulfilled $M_N^2 < 0.1 W_{\gamma^* p}^2$ were considered.

In addition, some checks were performed using a sample of proton dissociative MC events generated with EPSOFT [65]. This sample covered a region of Q^2 different from that of this analysis ($3 < Q^2 < 50$ GeV^2), so only distributions believed to be independent of this variable were compared. The comparisons were limited to the region $30 < W_{\gamma^* p} < 90$ GeV, where the samples overlap. Like PYTHIA, EPSOFT is based on VDM and Regge Theory. This generator was developed in the framework of HERWIG [72], and was tuned to reproduce the properties of photoproduction events measured with the ZEUS detector. It describes the ρ^0 proton dissociative cross section in terms of the ρ^0 elastic process:

$$\frac{d^2\sigma_{\gamma^* p \to \rho^0 N}}{dt dM_N^2} = \frac{1}{2} \frac{d\sigma_{\gamma^* p \to \rho^0 p}}{dt} \frac{d^2\sigma_{pp \to pN}/dt dM_N^2}{d\sigma_{pp \to pp}/dt}. \tag{7.4}$$

The second term is obtained from parameterization of pp cross sections [65]. The nucleonic mass was generated in the region $(1.25 \text{ GeV}^2)^2 < M_N^2 < 0.1 W_{\gamma^*p}^2$, including all resonances. The generated t distribution is well represented by an exponential function, with a slope $b_{diss} \simeq 5 \text{ GeV}^{-2}$.

PYTHIA was also used to study photon dissociative events, generated with a similar dependence of the differential cross section as 7.2 and with an effective slope $b \sim 6.8 \text{ GeV}^2$.

7.1.2   Radiative MC for elastic ρ^0 production

The measured ρ^0 cross section $ep \to e\rho^0 p$ contains, in addition to the one-photon-exchange reaction pictured in figure 2.1, contributions from higher order QED processes in which an electron radiates a real photon before (ISR, i.e. initial state radiation) or after (FSR, i.e. final state radiation) emitting the virtual photon responsible for the interaction, as well as from virtual corrections. The real photons are usually not detected and the measured (radiative) cross section can be related to the non-radiative cross section by

$$\sigma^{rad} = \sigma^{non-rad}(1 + \delta^{rad}) \tag{7.5}$$

where δ^{rad} is called the radiative correction.

A sample of elastic ρ^0 MC [75] events with radiative corrections calculated by the HER-ACLES [67] program was used to evaluate the impact of δ^{rad} in the BPC measurements. The Q^2, W_{γ^*p} and t dependences of the (non-radiative) γ^*p cross section were parameterized according to preliminary BPC ρ^0 results (similar to those presented for JETSET), and the ratio of longitudinal to transverse ρ^0 production was parameterized according to equation 7.1. For more information on this simulation, the reader is referred to [75].

7.2   Results of the MC simulation

Figure 7.1 displays the comparison of distributions between the data and the sample of elastic ρ^0 MC events, after all selection cuts (except the cut on the variable shown) are applied. In general, the agreement is good.

The shape of the p_T of the positive track, with two peaks, arises from the angular decay distributions, to which this variable is very sensitive. Figure 7.2 shows correlations between $\cos\theta_h$, Ψ_h and p_T: events with helicity 0 (i.e. $\cos\theta_h = \pm 1 \Longleftrightarrow \theta_h = 0 \vee \theta_h = \pi$ where θ_h is the polar angle of the positive pion in the ρ^0 rest frame), have a pion emitted along the direction of the ρ^0 while the other pion is almost at rest in the γ^*p center-of-mass, and this effect is reflected in the p_T spectrum in the LAB frame. After the reweighting of the MC angular decay distributions, performed according to SCHC and optimized to describe the $\cos\theta_h$ and Ψ_h distributions in data, the general features of the p_T distributions are reasonably well reproduced.

The disagreement in the $|t|$ distribution between elastic MC and data for high values of $|t|$ arises from the fact that the data are contaminated by proton dissociative ρ^0 background events, which have a shallower dependence on this variable.
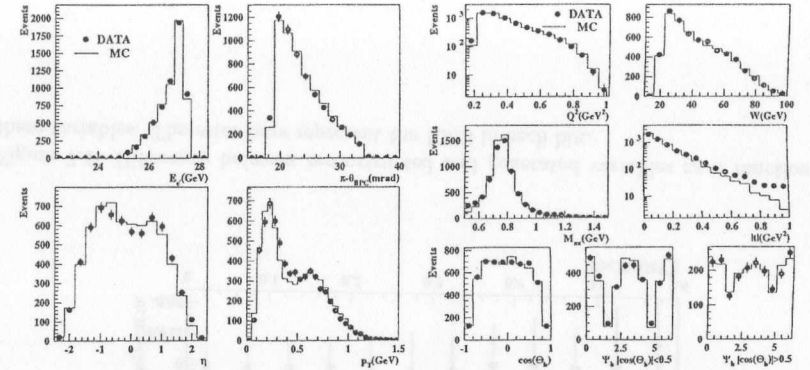
Figure 7.1: Comparison of distributions in data and MC simulation, after detector smearing: *i)* electron scattering angle, pseudorapidity and transverse momentum of positive track; *ii)* Q^2, W_{γ^*p}, $M_{\pi\pi}$, $|t|$, $\cos\theta_h$ and Ψ_h (in two bins of $\cos\theta_h$).
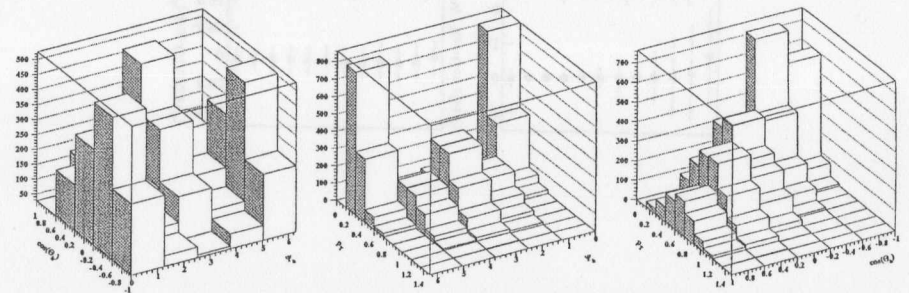
Figure 7.2: Correlations between decay angles and p_T: *i)* $\cos\theta_h$ versus Ψ_h; *ii)* p_T of positive track versus Ψ_h; *iii)* p_T of positive track versus $\cos\theta_h$. These are well described in the MC assuming SCHC
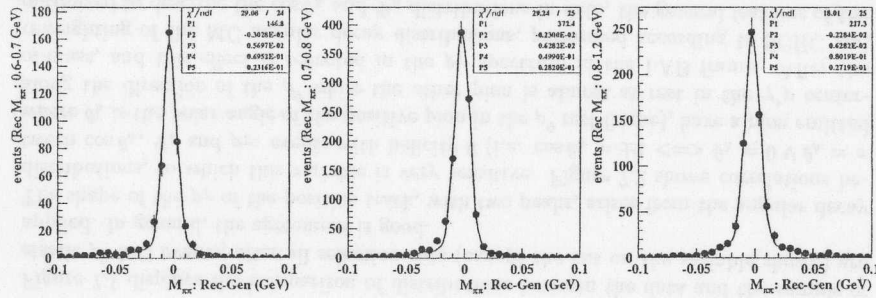
Figure 7.3: Difference between reconstructed and generated mass, determined via MC simulation, for different mass regions (0.6-0.7 GeV, 0.7-0.8 GeV, 0.8-1.2 GeV). The result of a fit with a double Gaussian is superimposed.

The MC simulation allowed the study of the smearing of the kinematical variables and decay angles due to detector resolution and reconstruction methods, by comparing the generated and reconstructed values of a particular variable.

Figure 7.3 displays the resolution in the two pion invariant mass, i.e. the distribution of differences between generated and reconstructed quantity, for three bins of $M_{\pi\pi}$. This distribution, directly related to the CTD momentum resolution, can be well described by a double Gaussian of the form

$$M_{\pi\pi}^{rec} - M_{\pi\pi}^{gen} = P_1 \left(e^{-\frac{1}{2}\left[\frac{(M_{\pi\pi}^{rec} - M_{\pi\pi}^{gen}) - P_2}{P_3}\right]^2} + P_4 e^{-\frac{1}{2}\left[\frac{(M_{\pi\pi}^{rec} - M_{\pi\pi}^{gen}) - P_2}{P_5}\right]^2} \right), \qquad (7.6)$$

and the results of fits to expression 7.6 show similar results for all the mass bins: the reconstructed mass is shifted by ~ -2 MeV with respect to the generated one, and the width of the dominant Gaussian (P_3) is ~ 6 MeV.

Figure 7.4 shows the difference between reconstructed and generated variables for Q^2, $W_{\gamma^* p}$, $\cos\theta_h$ Ψ_h and $|t|$ as a function of these same variables. The error bars represent the RMS in each bin (resolution). A good correlation between generated and reconstructed quantities is seen, and no significant bias are observed. The resolution in each variable, together with statistics considerations, constrains the size of the bins used in the analysis.

Figure 7.5 shows the purity Pur in the Q^2 and $W_{\gamma^* p}$ bins used in the analysis. For a bin i, this quantity is defined as

$$Pur_i = \frac{\text{Events generated and reconstructed in bin } i}{\text{Events generated in bin } i} \qquad (7.7)$$

The high purity in the bins used in the analysis reflects the small migrations between bins.
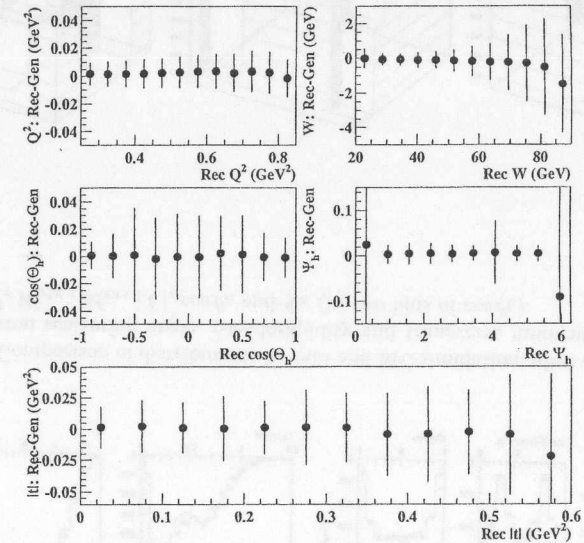
Figure 7.4: Difference between reconstructed and generated variables as a function of these variables. The error bars represent the RMS in each bin.
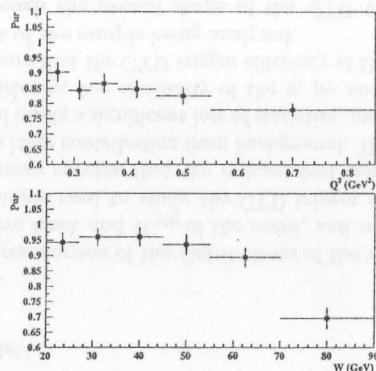
Figure 7.5: Purity for the reconstruction of the variables Q^2 and W_{γ^*p} in the bins used in the analysis.

7.3 The acceptance calculation

The generalized acceptance Acc for elastic ρ^0 events was calculated in a bin i as

$$Acc_i = \frac{\text{Events reconstructed in bin } i_{rec}}{\text{Events generated in bin } i_{gen}} \qquad (7.8)$$

where i_{rec} and i_{gen} stand for bins in the reconstructed and generated variable(s), respectively. This quantity, calculated bin-by-bin, accounts not only for the purely geometrical acceptance of the detector, but also for trigger and selection cuts efficiencies [1]. Although it considers only the net migration of events from other bins due to finite detector resolution or reconstruction methods which smear the distributions, this approach is validated if there is a good agreement between the reconstructed distributions of data and MC and a high purity in the chosen bins, as in the present case.

In the present analysis it is useful to distinguish different contributions to the generalized acceptance:

$$Acc = \epsilon_{Sel\ cuts} \cdot \epsilon_{Migrat} \cdot \epsilon_{FLT_{CTD}} \cdot \epsilon_{FLT_{BPC}} \cdot \epsilon_{SLT} \cdot \epsilon_{TLT} \qquad (7.9)$$

corresponding to the efficiency of the offline selection cuts and migrations (listed in section 6.2), the efficiency of the First Level Trigger (which, in turn, can be divided into requirements on BPC and the requirements on the CTD), the efficiency of the Second Level Trigger (requirements only on the CTD) and the efficiency of the Third Level Trigger (requirements only on the CTD).

---

[1] For details on the Z vertex treatment, see below.
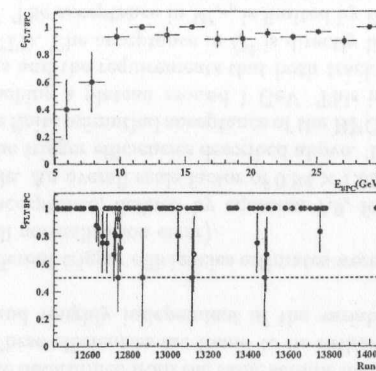
Figure 7.6: BPC trigger efficiency, determined with an independently triggered sample, versus $i)$ electron energy and $ii)$ run number. The inefficiency seen in some runs is due to a hardware fault. Runs with BPC FLT efficiency lower than 0.5 have been excluded from the analysis.

7.3.1 Selection efficiency and effect of migration

The efficiency of the selection cuts and impact of migrations was determined bin-by-bin with the elastic ρ^0 MC sample, for each variable under study [2].

7.3.2 Trigger efficiencies

The BPC FLT was not simulated in the Monte Carlo. As mentioned in section 6.1, the requirement on BPC at FLT corresponded to a minimum energy deposition in this detector. The threshold was set to roughly 6 GeV, far below the energy cut performed offline in this analysis (20 GeV) and, in general, the BPC trigger efficiency was very high, $\sim 100\%$. However, during some runs in the 1995 data taking period a hardware fault in a discriminator used in the trigger logic caused some good events to be lost at the FLT level. The runs where such problem caused a serious decrease in the BPC FLT rate have been excluded from the elastic ρ^0 sample; however, the problem was present, at a smaller level, in some of the runs used in the analysis. This was accounted for through an overall BPC FLT efficiency correction, determined with the help of an independently triggered sample (photoproduction ρ^0 sample), triggered by track candidates and an energy deposit in the main ZEUS calorimeter), taken in the same runs used in this analysis, where there are no cuts imposed at FLT to any quantity measured with the BPC

---

[2] For the cross section measurements, obtained via fits to the mass spectra in different Q^2 and W_{γ^*p} ranges, as described in section 9.4, the generalized acceptance is determined in a multidimensional space, corresponding to the mass, Q^2 and W_{γ^*p} of the events

The efficiency of the BPC FLT $\epsilon_{FLT_{BPC}}$ is defined as

$$\epsilon_{FLT_{BPC}} = \frac{\text{Events with } E_{BPC} > 20 \text{ GeV which fire CTD FLT}}{\text{Events with } E_{BPC} > 20 \text{ GeV}} \qquad (7.10)$$

This quantity is found to be 0.94 ± 0.02, independent of the energy of the candidate, as shown in figure 7.6.

The CTD FLT was simulated in the MC with the trigger simulation package ZGANA. However, the reliability of this simulation had to be investigated. This was done, as above, with the help of another independently triggered sample, this time a sample where no tracking requirements are made at any level of the online trigger. The sample used is the so called BPC F2 sample, collected through an inclusive trigger, which requires only an energy deposit in BPC and a minimum y_{JB} reconstructed at the trigger level using only calorimeter quantities (SLOT 52+DIS2+DIS17, in appendix B). Since the efficiency of the CTD trigger to recognize track candidates depends on the characteristics of the event (total number of reconstructed tracks, number of vertex tracks, angular distribution inside the tracking detector, etc.), a set of cuts was applied in order to study the trigger efficiency with a sample comparable to the one under analysis. These cuts were:

- two opposite charge tracks, coming from a vertex.

- Z vertex position within ± 50 cm of nominal interaction point.

- For each track, $|\eta| < 1.75$.

- For each track, $p_T > 150$ MeV.

- $0.6 < M_{\pi\pi} < 1.2$ GeV ($M_{\pi\pi}$ is the invariant mass of the event, calculated assigning the pion mass to each track).

- $0.25 < Q^2 < 0.85$ GeV^2.

- $20 < W_{\gamma^*p} < 90$ GeV.

- $|t| < 0.6$ GeV^2.

Figure 7.7 *i)* shows the comparison of the distributions of the variables η of positive (left side) track, p_T of positive track and W_{γ^*p} of the event, and mass, between the BPC ρ^0 data sample and the sample used to study the CTD trigger efficiency. It is clear from the comparison of the mass spectra that the independent sample, although containing primarily ρ events, has a large contribution from background. However, a tighter rejection of this background would imply a significant loss of statistics, making it hard to investigate dependencies of the efficiency; the similarity of the η, p_T and W_{γ^*p} distributions after selection cuts should ensure that the CTD trigger efficiency of the independently triggered sample is similar to that of the sample being analyzed.

It was found that although the overall shape of the CTD trigger efficiency was well reproduced in the simulation, the normalization was underestimated. It was decided to use the MC FLT simulation in order to take properly into account the shapes of the efficiency, but to correct the resulting MC acceptance by a factor 1.05 ± 0.05. Figure 7.7
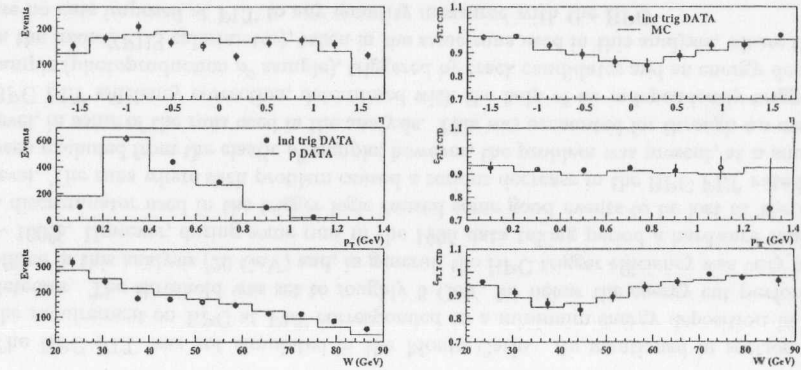
Figure 7.7: *i)* Comparison of the pseudorapidity and transverse momentum of the positive track, and W_{γ^*p} distributions between the analysis sample and the independently triggered sample used in CTD trigger studies; *ii)* CTD FLT trigger efficiency versus pseudorapidity and transverse momentum of the positive track, and W_{γ^*p} as determined with the independently triggered data sample and in the MC simulation (after correction).

ii) shows the comparison of the trigger efficiency, defined in the same fashion as equation 7.10, in data (independent sample described above) and in the MC simulation, after correction, versus different variables.

The SLT and TLT requirements are limited to tracking quantities, as described in chapter 6. These quantities were not available in the MC sample used in this analysis. Therefore, the efficiencies were determined from the same sample used in the investigation of the CTD FLT efficiency. These efficiencies are found to be rather high (SLT: 0.980 ± 0.010, TLT: 0.990 ± 0.005), and roughly independent of the variables in study, as shown in figure 7.8.

The errors from the different trigger efficiencies estimates were added in quadrature, and amount to 5.5% (overall normalization error).

Figure 7.9 shows the acceptance, defined by equation 7.9, for elastic ρ^0 production as given by the MC sample. An overall scale factor of $0.94 \times 1.05 \times 0.98 \times 0.99$ needs to be applied to correct for the trigger efficiencies described above. The small magnitude of the acceptance is due to the finite azimuthal acceptance of the BPC. The acceptance increases for increasing $M_{\pi\pi}$, reaching a plateau around 1 GeV. This is determined by the polar angle of the decay pions and the requirements that both tracks from the decay pions are well contained in the CTD. The acceptance in Q^2 is directly limited by the position and dimensions of the BPC. The acceptance in W_{γ^*p} is limited by the CTD acceptance, as for $\cos\theta_h$: for large values of $|\cos\theta_h|$ (and $\Psi = 0, \pi, 2\pi$ due to the correlations between these variables, see figure 7.2) one of the pions is outside the tracking system. The shape of the acceptance versus $|t|$ reflects the combination of the acceptance in p_T of the ρ (almost
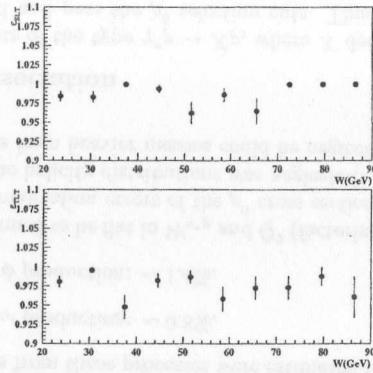
Figure 7.8: CTD second and third trigger levels efficiency as a function of W_{γ^*p} (from independently triggered data sample).

flat) with the narrow p_T range of positrons accepted by the BPC.

The analysis was restricted to the areas limited by the dashed lines, as a compromise between acceptance, statistics and contamination by backgrounds.

7.4 Background sources and estimates

Below are listed different sources of background which contribute to the data sample, and the means used to estimate their impact. It was found that the contribution from beam gas interactions was small, as was that of elastic production of ω and ϕ and γ dissociative events. Proton dissociative ρ^0 production, on the other hand, accounted for 23.3% of the selected events, and were subtracted statistically.

7.4.1 Non $e - p$ background: positron/proton beam gas interactions

Beam gas interactions cannot be distinguished from ep events if they occur close to the interaction point. The contributions from this kind of background were estimated using pilot bunches, i.e. unpaired electron or proton bunches where the RF-bucket of the counterpart particle is not filled. These types of bunches are distinguished from colliding ones by the bunch crossing number. In the total data sample, only 3 events originate from non-ep bunches (p-pilot bunches). One of these events, however, originates from a run with more bunches marked as p-pilot than the nominal number (9, instead of 6). If these 3 events are scaled by the ratio of the proton current in p colliding bunches to that of p-pilot bunches, which amounts to 30.7 ± 4.4, the maximum contribution from this
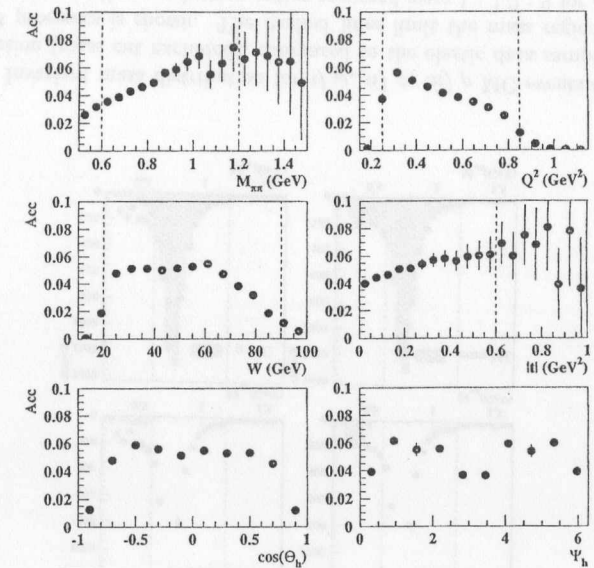
Figure 7.9: Generalized acceptance, determined by MC simulation, as a function of the variables $M_{\pi\pi}$, Q^2, W_{γ^*p}, $| t |$, $\cos\theta_h$ and Ψ_h. The normalization requires correction from FLT, SLT, and TLT efficiencies, as described in the text. The dashed lines limit the regions used in the analysis.

background is estimated to be 1.6%.

7.4.2 Other vector mesons

Since no particle identification was performed at the event selection and neutral particles can remain undetected in an event, other vector mesons can be misidentified as ρ^0's and constitute a background.

The production of ω and ϕ mesons thus was studied with MC samples of these mesons by submitting them to the analysis selection cuts. In these samples, all decay modes were simulated. In particular, those most likely to leave signatures similar to that of ρ^0 production are:

- $\omega \to \pi^+\pi^-\pi^0(\gamma\gamma)$ (Branching ratio:88.8%),

- $\omega \to \pi^+\pi^-$ (Branching ratio:2.2%),

- $\phi \to K^+K^-$ (Branching ratio:49.1%),

- $\phi \to \rho^0\pi^0 \to \pi^+\pi^-\pi^0(\gamma\gamma)$ (Branching ratio:12.9%),

- $\phi \to \pi^+\pi^-\pi^0(\gamma\gamma)$ (Branching ratio:2.4%).

Figure 7.10 shows the invariant mass of the two charged decay particles for ω, ϕ and ρ^0 MC samples, when the pion mass is assigned to each track, compared to that of the data. The normalizations was determined assuming the ratio of ω to ρ^0 production of 1/9 and using the measured cross section for ϕ production in a similar W_{γ^*p} and Q^2 region [50]. The dashed lines indicate the range used in the analysis, $0.6 < M_{\pi\pi} < 1.2$ GeV. It is clear that there is little overlap with the background processes: in fact, that was one of the reasons why events with invariant mass below 0.6 GeV were not considered. The background contributions from these processes were estimated to be

- Contribution from ω production: $\sim 0.8\%$.

- Contribution from ϕ production: $\sim 1.4\%$.

These contributions, assumed to be flat in W_{γ^*p} and Q^2 (factorization of the upper vertex) were included in the normalization errors of the ρ^0 cross sections. Since their magnitude is small, the impact in the helicity distributions was neglected. It was also assumed that background contributions from heavier mesons could be neglected in the analysis.

7.4.3 Photon dissociation

Photon dissociative events of the type $\gamma^*p \to Xp$, where X decays into hadrons, can be poorly reconstructed and and pass the ρ^0 selection cuts. This process was investigated with a sample of MC events (PYTHIA) generated in the W_{γ^*p} range 12-200 GeV, and passed through the analysis cuts. The background was found to be approximately flat in $M_{\pi\pi}$ in the signal region and up to ~ 1.4 GeV, falling to zero around 2 GeV. As the ratio of photon dissociative cross section to that of elastic ρ^0 production is not known,
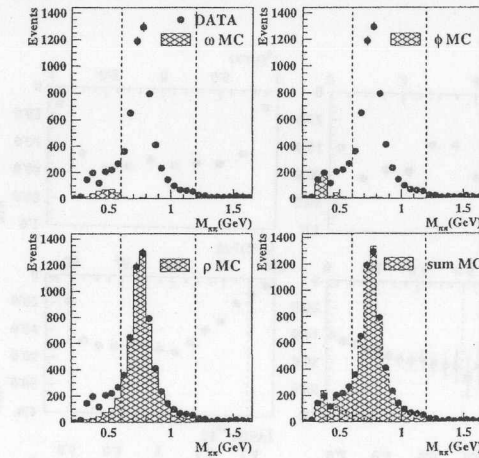
Figure 7.10: Invariant mass distribution for *i)* ω, *ii)* ϕ, *iii)* ρ MC events that pass the analysis selection (mass cut excluded), compared to the elastic data sample. In *iv)* the sum of the 3 processes is shown. The dashed lines limit the mass region used in the analysis. The cross section production ratios assumed were $1 : 1.2 : 9$ for $\omega : \phi : \rho$ (see text).
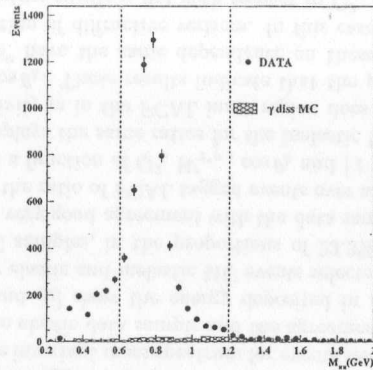
Figure 7.11: Invariant mass distribution for photon dissociative MC events that pass the analysis selection (mass cut excluded), compared to the elastic data sample. The normalization of the plot was done ascribing all events in the mass region 1.3-1.5 GeV to this background source, therefore establishing the maximum contamination from such process in the analysis sample. The dashed lines limit the mass region used in the analysis.

the maximum contamination due to this reaction was estimated ascribing all data events reconstructed between $1.3 - 1.5$ GeV to this process and assuming a flat mass dependence. A upper limit of 3% was found. This result is similar to that obtained if an extra (non-interfering) constant term is added to the function used for the mass fit according to the Söding model (see section 9.1), but the introduction of one more fit parameter increases significantly the uncertainties of the fit.

In principle, double dissociative events of the type $\gamma^* p \to XN$ can also constitute a background. However, not only is the acceptance for such events much smaller than that of γ dissociative ones, but the shape of the reconstructed $M_{\pi\pi}$ distribution is expected to be similar for both processes [99]. In that case, also this contribution is included in the above estimate.

7.4.4 Proton dissociation

The main source of background consists of inelastic ρ^0 production events, where the proton diffractively dissociates into hadrons $\gamma^* p \to \rho^0 N$. In some of these events the fragments of the outgoing nucleon deposit energy in the forward calorimeter or in the Proton Remnant Tagger of the ZEUS detector (see section 3), but a significant fraction escapes detection (events with diffractive masses below ~ 4 GeV), leaving a signature exactly like that of an elastic reaction.

The contribution from this process was studied in detail, with the help of an inelastic MC sample (PYTHIA) and subsamples of data events which were tagged as proton dissociative
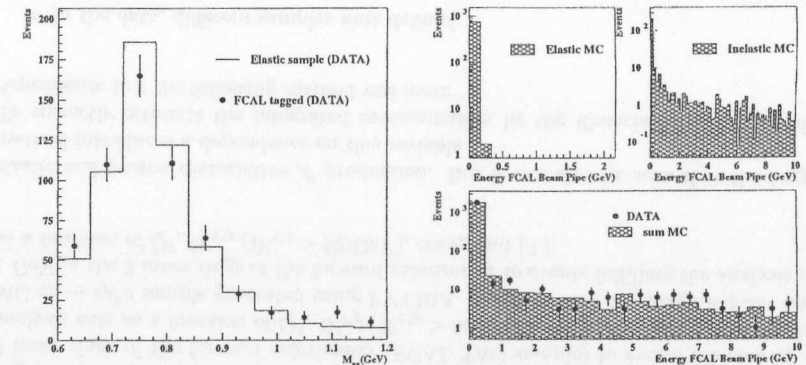
Figure 7.12: *i)* Invariant mass distribution for the FCAL tagged data sample compared to the elastic data sample. *ii)* Energy spectrum in the 2 inner rings of the forward calorimeter for an elastic MC sample, *iii)* and for an inelastic MC sample. *iv)* Comparison between a sum of the two MCs, in the ratios 23.3% inelastic events to 76.7% elastic events passing analysis selection, and the analysis sample (excluding requirement on unmatched energy around the beam pipe)

by an energy deposition in the forward region. Proton dissociative events were identified by one of the following conditions:

- **FCAL TAG**: the requirement of matching all calorimeter objects to tracks was removed for clusters around the FCAL beam pipe. An energy deposit of at least 1 GeV in the two FCAL inner rings surrounding the beam pipe was required. The acceptance of this tag starts at diffractive masses M_N around 2.5 GeV, reaches a maximum around 7.5 GeV and decreases until it vanishes around 17 GeV (this decrease is due to the rejection of events with energy depositions not associated with tracks in the outer part of FCAL). These events were selected in the range $W_{\gamma^*p} > 50$ GeV only. If the elasticity cuts around the beam pipe are relaxed for events with lower W_{γ^*p}, where the tracks tend to go in the forward direction, other processes (for example non-diffractive events with two tracks reconstructed at the ρ^0 mass) pass the selection cuts and the subsample obtained is no longer a pure proton dissociative one.

- **PRT2 TAG**: in addition to the selection cuts for elastic ρ^0 production, a signal of at least 1 MIP in both counters of one pair of PRT2 paddles is required ($E_{PRT2_1} > 5$ ADC counts and $E_{PRT2_2} > 2$ ADC counts for data, according to [29], $E_{PRT2_1} > 0.5$ ADC counts and $E_{PRT2_2} > 0.5$ ADC counts for MC). Due to the standard elasticity cuts, events with $M_N < 4$ GeV are rejected and the PRT2 acceptance covers only the small diffractive mass region.

However, it is known that also elastic events with $|t| \gtrsim 0.3$ GeV^2 can leave a signal in the PRT2 [71] due to the large distance of the counters to the interaction point, and their proximity to the beam line. In addition, the tagging efficiency of this component in the MC has not been tuned to match that of data. Therefore, the events tagged with PRT2 were only used to cross check assumptions made while estimating the background contribution using FCAL tagged events.

Figure 7.12 *i)* shows the invariant mass spectrum for events selected with the FCAL TAG, compared to that of the elastic data sample and the agreement is good.

Figures 7.12 *ii), iii)* and *iv)* show the energy deposited in the two inner rings of the forward calorimeter for elastic and inelastic MC events selected by the analysis cuts, and for a sum of both MC samples, in the proportions of 23.3% inelastic to 77.6% elastic events. The last shows very good agreement with the data sample also shown in the plot. Figure 7.13 *i)* displays the ratio of FCAL tagged events over all events passing the elastic ρ^0 selection in data, as a function of Q^2, W_{γ^*p}, $\cos\theta_h$ and $|t|$. The first three ratios are flat. Figure 7.13 *ii)* displays the same ratios for the inelastic MC sample and shows that the requirement of activity in in the FCAL inner region does not distort the acceptance versus Q^2, W_{γ^*p} and $\cos\theta_h$. These results indicate that the proton dissociative and the elastic production of ρ^0 have the same dependence on these variables, supporting the hypothesis of factorization of diffractive vertices. In this case, the contamination of the data sample by dissociative events is flat with respect to Q^2, W_{γ^*p} ($W_{\gamma^*p} > 50$ GeV) and $\cos\theta_h$.

On the other hand, as a function of t, the ratio of inelastic events to events fulfilling the selection cuts in the data increases with t, as expected due to the different t slopes for
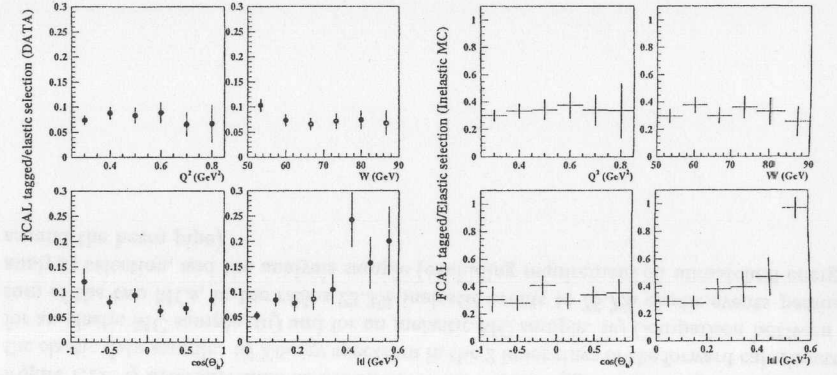
Figure 7.13: *i)* Ratio, for data, of events with an energy deposit above 1 GeV in the 2 inner rings of the forward calorimeter (FCAL TAG sample) to events selected by the analysis cuts as a function of Q^2, W_{γ^*p} ($W_{\gamma^*p} > 50$ GeV), $\cos\theta_h$ and $|t|$; *ii)* Ratio, for a MC $ep \to e\rho^0p$ sample generated using PYTHIA, of events with an energy deposit above 1 GeV in the 2 inner rings of the forward calorimeter to events fulfilling the analysis cuts as a function of Q^2, W_{γ^*p} ($W_{\gamma^*p} > 50$ GeV), $\cos\theta_h$ and $|t|$.

elastic and proton dissociative ρ^0 production. But it can also be seen that the tagging method introduces a dependence on this variable [3].

To correctly estimate the integrated contamination by the dissociative process and its dependence in t the following method was used:

- In the data, different samples were defined:

  -DATA$_{ANA}$, the usual analysis sample, selected via the cuts described in the previous chapter. This sample consists mostly of elastic events, but contains also the indistinguishable *residual* proton dissociative events, DATA$_{ANA}$ = DATA$_{ANA}^{el}$ + DATA$_{ANA}^{inel}$, where the indices *el* and *inel* refer to elastic ρ^0 production, and (inelastic) proton dissociative ρ^0 production events, respectively.

  -DATA$_{FCAL\ TAG}^{inel}$, the sample of events tagged in the FCAL, as described above, which is believed to contain only proton dissociative ρ^0's.

  In this notation, the contamination $C(t)$ of the data sample by proton dissociative background as a function of t can be written as

---

[3]Different tagging definitions with the forward calorimeter can be adopted that do not distort the shape of the observed events in t, as, for example, the one described in [99]. The results from different approaches have been compared and give consistent results.

$$C^{inel}(t) = \frac{DATA_{ANA}^{inel}(t)}{DATA_{ANA}(t)} \qquad (7.11)$$

- Similar samples were defined in the proton dissociative MC:

  -MC_{ANA}^{inel}, inelastic events that fulfill the analysis cuts. This sample consists only of undetected residual proton dissociative events.

  -$MC_{FCAL\ TAG}^{inel}$, a sample of events tagged in the FCAL, as described above, which again contains only proton dissociative ρ^0's.

- It was assumed that

$$\frac{DATA_{ANA}^{inel}}{DATA_{FCAL\ TAG}^{inel}} = \frac{MC_{ANA}^{inel}}{MC_{FCAL\ TAG}^{inel}} \qquad (7.12)$$

In that case, equation 7.11 can be expressed as

$$C^{inel}(t) = \frac{MC_{ANA}^{inel}(t)}{MC_{FCAL\ TAG}^{inel}(t)} \frac{DATA_{FCAL\ TAG}^{inel}(t)}{DATA_{ANA}(t)} \qquad (7.13)$$

The contribution of proton dissociation integrated over t in the data sample estimated using this procedure is

$$C^{inel} = 23.3\% \pm 2.5\%(stat) \pm 7\%(sys) \ (for \ |t| < 0.6 \ GeV^2) \qquad (7.14)$$

where the systematic error was determined with the methods described in the following chapter, and corresponds to checks vi.1, vi.2, vi.3.

Assuming exponential shapes in t for elastic and inelastic events, tagged in FCAL or passing analysis requirements, expression 7.13 can be written as

$$C^{inel}(t) = \qquad (7.15)$$
$$\frac{A_1 e^{b_{ANA}^{inel}|t|}}{A_2 e^{b_{FCAL\ TAG}^{inel}|t|}} \frac{A_3 e^{b_{FCAL\ TAG}^{inel}|t|}}{A_4 e^{b_{ANA}^{el}|t|} + \frac{A_1 A_3}{A_2} e^{b_{ANA}^{inel}|t|}} =$$
$$\frac{\frac{A_1 A_3}{A_2} e^{b_{ANA}^{inel}|t|}}{A_4 e^{b_{ANA}^{el}|t|} + \frac{A_1 A_3}{A_2} e^{b_{ANA}^{inel}|t|}} =$$
$$\frac{1}{K e^{b_{ANA}^{diff}|t|} + 1}$$

where b_{ANA}^{diff} is the observed difference in slopes for elastic and inelastic events submitted to the analysis cuts.

In the present kinematic range expression 7.15 can be approximated via the Taylor expansion of the exponential functions by

$$C^{inel}(t) \simeq \alpha(K, b_{ANA}^{diff}) + \beta(K, b_{ANA}^{diff})|t| \qquad (7.16)$$
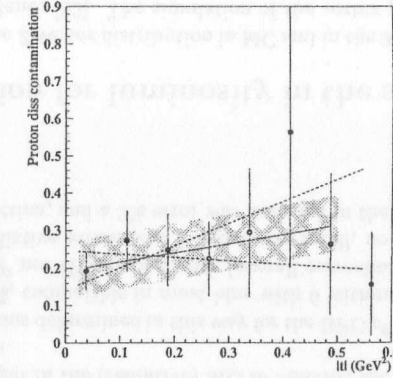
Figure 7.14: Proton dissociative contamination in the analysis sample versus $|t|$

where α and β are constants related to K and b_{ANA}^{diff}. To determine the contamination as a function of t, a fit of $C(t)$ (equation 7.13) to 7.16 was performed, constrained to give a total contamination of 23.3% (see above).

$$\beta = 0.25 \pm 0.29(stat) \pm 0.18(sys) \qquad (7.17)$$

corresponding [4] to $b_{ANA}^{diff} \sim 1.7 \ GeV^{-2}$. The systematic error was determined with the methods described in the following chapter, and corresponds to checks vi.4.

The result of this fit can be seen in figure 7.14. The solid line represents the result presented above, and the shaded area displays 7.4% statistical and systematic uncertainty in the integrated contamination (normalization). The dashed lines represent the extreme slopes obtained from the error on this parameter (statistical and systematic errors added in quadrature), for a fixed normalization.

Next it is shown that the above measurements can be extended to $W_{\gamma^* p} < 50 \ GeV$. The ratio of events tagged with PRT2 to all events fulfilling the analysis cuts is presented in figure 7.15 i) for data, as a function of $W_{\gamma^* p}$. It is flat also below 50 GeV. It is shown in ii) that also for the dissociative MC, this ratio does not depend on $W_{\gamma^* p}$, and therefore, the requirement in data of a PRT2 hit does not distort the acceptance in this variable. These results validate the use of the same expression for the contamination in the whole $W_{\gamma^* p}$ region under study.

The correction for proton dissociation background was done by assigning a weight $w(t) = 1 - C^{inel}(t)$ to each event in the data sample according to their t value.

---

[4] This value is an observed difference in slope, significantly affected by the fact that the acceptance for analysis cuts for elastic events as a function of t is, in this analysis, different of from that of inelastic events.
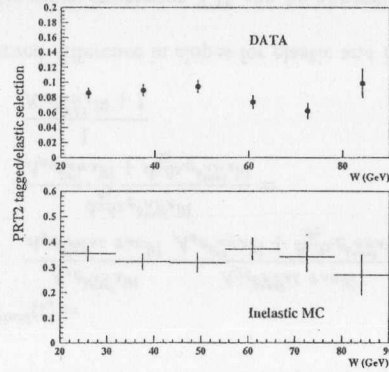
Figure 7.15: *i)* Ratio, for data, of events with an energy deposit in the PRT2 (PRT2 tagged sample, see text) to events selected by the analysis cuts as a function of W_{γ^*p} ; *ii)* ratio, for PYTHIA, of events with an energy deposit in the PRT2 to events selected by the analysis cuts as a function of W_{γ^*p} . While the overall tagging efficiency depends on the details of the PRT2 simulation, the fact that both these distributions are flat as a function of W_{γ^*p} allows the extrapolation of the inelastic contamination determined using FCAL tagged events for $W_{\gamma^*p} > 50$ GeV to all the W_{γ^*p} range in the analysis.

7.4.5 Non-resonant $\pi\pi$ production

Another background process to ρ^0 production is the diffractive non-resonant $\pi^+\pi^-$ production, $\gamma^*p \rightarrow \pi^+\pi^-$. In the cross section measurements presented in this thesis this background has been accounted for in the framework of the Söding model, as described in detail in section 9.1. For the study of the distribution of $d\sigma/d|t|$ and the decay angles, this background was not accounted for, and the results presented are for $\pi^+\pi^-$ production in the two-pion invariant mass range 0.6-1.2 GeV, where ρ^0 production dominates. Some implications are discussed together with the results.

7.5 Radiative corrections

The value of the radiative corrections δ^{rad} (see expression 7.5) depends on the:

W_{γ^*p} and Q^2 dependence of the ρ^0 production cross section.

Efficiency of the detection of the real photons radiated from the in- and outgoing electron.

Reconstruction method for the kinematical variables.

Selection cuts applied in the analysis (for example, requirements on the measured scattered electron energy.)

Final state radiation does not affect the kinematical reconstruction used here, but may influence slightly the acceptance of the selection cuts.

Initial state radiation, however, may introduce both an overall correction to the measured cross sections, and a distortion of their shapes. It can be seen from expressions 6.5, 6.6 and 6.7 that, when the constrained method is used to reconstruct the kinematic variables, ISR leads to migration of events along lines of constant W_{γ^*p}, and towards higher Q^2, due to an overestimated energy of the incoming electron, E_e.

The impact of both ISR and FSR on the results was estimated using the radiative elastic ρ^0 MC sample, at generator level, in the following way: the radiative cross section (see equation 7.5) in a bin i in Q^2 and W_{γ^*p}, σ_i^{rad} can be expressed as

$$\sigma_i^{rad} = \sigma_{tot}^{rad} \frac{N_i}{N_{tot}}, \tag{7.18}$$

where σ_{tot}^{rad} is the total radiative cross section in the generated range, corresponding to the total number N_{tot} of events in the MC sample, and N_i is the number of events in bin i where the radiative corrections are being calculated. This number of events takes into account the Q^2 and W_{γ^*p} cuts, where Q^2 and W_{γ^*p} have been reconstructed from the generated energies and momenta, using the constrained method, and also requiring the (generated) scattered electron energy to be larger than 20 GeV (this requirement, corresponding to the selection cut $E_{BPC} > 20$ GeV - see section 6.2.3 - reduces significantly the contamination of the data by events with a ISR photon of high energy, therefore diminishing considerably the radiative corrections).

Since σ_{tot}^{rad} is known (from HERACLES), σ_i^{rad} can be simply determined from N_i and N_{tot}. Once σ_i^{rad} has been determined, it can be compared to $\sigma_i^{non-rad}$ to extract the radiative correction δ_i^{rad} (see equation 7.5). $\sigma_i^{non-rad}$ is calculated from the non-radiative parameterizations used as input in the (radiative) MC to describe the Q^2 and W_{γ^*p} dependences of the ep cross section.

The radiative corrections determined in this way for the BPC ρ^0 analysis varied in different bins from -1% to +4%, compatible in most bins with 0 within the statistical limitations, and without a clear Q^2 nor W_{γ^*p} dependence (overall correction $2.0 \pm 0.5\%$ (stat)). Since the impact of the radiative events was found to be small, no correction was applied to the measured cross section, and a 2% error was included in the normalization uncertainty due to this effect.

7.6 Correction for luminosity in the satellite bunches

Figure 7.16*i)* shows the Z vertex distribution in MC and in the 95 data, from a sample with a flat Z vertex acceptance [83]. The simulation of the vertex position in the MC agrees well with that of data in the central region of the detector. However, the simulation of collisions coming from satellite bunches is not properly implemented. In order to calculate a correct acceptance from this MC sample, the following procedure were taken:
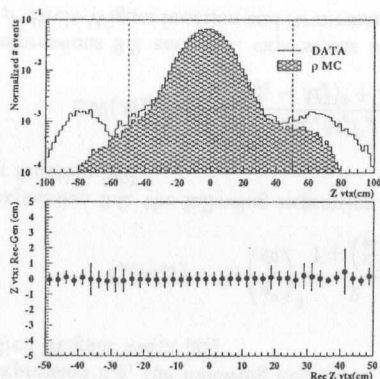
Figure 7.16: *i)* Vertex distribution in the MC simulation and in an unbiased 95 data sample. The dashed lines limit the region of agreement, in which the cross section was extracted (see text); *ii)* difference between reconstructed and generated vertex versus reconstructed vertex position (the error bars represent the RMS in each bin).

- The event selection, as described in the previous chapter, required that the reconstructed Z vertex is within ± 50 cm of the nominal interaction point.

- The acceptance was calculated for the *bin in Z vertex* where data and MC agree: that is, the acceptance was defined as the ratio of events that pass all selection cuts, including the cut on reconstructed vertex position, regardless of the generated vertex, to those events generated in $-50 < Z$ vertex generated < 50 cm.

- The luminosity considered for cross section extraction corresponded to the fraction of the total luminosity for the runs used within the vertex cut calculated with the unbiased Z vertex distribution from the data.

This method was chosen since it allowed the use of the MC sample before the true Z vertex distribution for the 95 data taking period was fully understood. When this distribution became available, a simple additional correction, corresponding to a re-scaling of the luminosity was introduced: $\mathcal{L}_{eff} = 0.954\mathcal{L}$, where $\mathcal{L} = 3.82$ pb^{-1}

The migrations in Z vertex are not sensitive to the exact shape of the vertex distribution outside ± 50 cm, as the resolution in this variable is of the order of 5 mm, as shown in figure 7.16 *ii)*.

Chapter 8
Estimate of systematic uncertainties

This chapter discusses the methods used to estimate the systematic uncertainties associated with the results of this analysis and summarizes the main error sources.

8.1   Systematic errors

The contribution to the total systematic error due to a certain effect or uncertainty was determined, in most cases, by changing the cuts applied in the selection of the data and/or MC samples, or by changing reweighting factors in the simulations and repeating all the analysis steps. The systematic checks performed have been grouped into classes, described below:

i. Systematic checks related to the tracks

   i.1 Cut on the minimum transverse momentum of the track was varied, in the data and MC, from $p_T > 150$ MeV to $p_T > 200$ MeV, and to $p_T > 100$ MeV.

   i.2 Cut on the maximum η of each track was varied from $|\eta| < 1.75$ to $|\eta| < 2$.

   i.3 The presence of tracks not associated with the vertex was allowed, both in the data and MC.

ii. Systematic checks related to the BPC

   ii.1 The BPC fiducial volume was reduced from
   $5.17 < BPC_X < 9.97$ cm and $-2.82 < BPC_Y < 3.18$ cm to
   $5.37 < BPC_X < 9.17$ cm and $-2.22 < BPC_Y < 2.58$ cm
   in the data and MC.

   ii.2 The cut on the energy deposited in the BPC was varied, in the data and MC, from 20 GeV to 18 and 22 GeV. This cut reflects the sensitivity to ISR.

   ii.3 The BPC energy scale was changed in the data by 0.5%.

   ii.4 The absolute position of the BPC was varied by ± 0.5 cm along X in the data.

ii.5 The requirement on the relative energy of first and second BPC strip was dropped in the data and MC.

iii. Systematic checks related to the selection of elastic events (matching)

iii.1 In the matching of tracks to CAL objects, the criteria to define an unmatched energy cluster was tightened, changing the matching probability cut from 1/1000 to 1/100 in the data and MC.

iii.2 An alternative matching algorithm [99] was applied in both data and MC. It extrapolates the tracks into the calorimeter modules, and requires that the energy of every cell outside a circle of diameter 40 cm (EMC section) and 55 cm (HAC section) around the pion impact point does not exceed 200 MeV.

iv. Systematic checks related to the extraction of the signal

A. Checks for cross section extraction in the framework of Söding model, using the parameterizations of equations 9.1, 9.2 and 9.3:

iv.1. The mass range used in the analysis was enlarged to 0.55-1.25 GeV in the data and MC.

iv.2. The mass binning was varied.

iv.3. The ρ^0 mass and width were *i)* fixed to the PDG values *ii)* released in the fits to extract cross sections.

B. Alternative cross section extraction (only the impact in the overall normalization was investigated):

iv.1. Instead of expression 9.3, the following expression was used to describe the relativistic Breit-Wigner width [99]

$$\Gamma_\rho(M_{\pi\pi}) = \Gamma_0 \left(\frac{q^*}{q_0}\right)^3 \frac{2}{1 + \left(\frac{q^*}{q_0}\right)^2} \tag{8.1}$$

iv.2. Instead of expression 9.2, the following expression was used to describe the Breit-Wigner function [99]

$$\mathrm{BW}(M_{\pi\pi}) = \frac{1}{q^*} \frac{M_{\pi\pi} M_\rho \Gamma_\rho}{(M_{\pi\pi}^2 - M_\rho^2)^2 + M_\rho^2 \Gamma_\rho^2}. \tag{8.2}$$

iv.3. Instead of expressions 9.2 and 9.3, expressions 8.2 and 8.1 were used to describe the ρ^0 Breit-Wigner function and its momentum dependent width [99]

iv.4. The Ross-Stodolsky model was used to extract the cross section, integrating expression 9.5 over the same region as in the nominal analysis (see discussion on the ρ^0 mass shape).

iv.5. The prescription adopted by the E665 experiment [37] was used to extract the cross section. Given that the data sample contains very little background (other than, eventually, the indistinguishable non-resonant $\pi\pi$ events suggested by the Söding model described in section 9.1), the events in the two pion invariant mass region 0.57-0.97 GeV are assumed to be ρ^0's, and to account for 87.6% of the total resonance.

v. Systematic checks related to the elastic MC event simulation

v.1 The Q^2 dependence of the cross section was varied in the MC simulation: the value of n in $\sigma \propto \frac{1}{1 + \frac{Q^2}{M_\rho^2}}^n$ was changed from $n = 1.75$ to $n = 2$.

v.2 The $W_{\gamma^* p}$ dependence of the cross section was varied in the MC simulation: the value of δ in $\sigma \propto W_{\gamma^* p}^{\ \delta}$ was changed from $\delta = 0.12$ to $\delta = 0.2$

v.3 The ratio R of longitudinal to transverse cross sections was changed in the MC simulation from R=0.5*Q^2 to R=0.3*Q^2.

vi. Systematic checks related to the estimation of contamination by proton dissociative events

vi.1 Different definitions of tagged proton dissociative events were used, and the contamination by proton dissociative events was reevaluated:

a. the requirement of a minimum energy deposit of 1 GeV in the FCAL inner rings was changed to 0.4 and 1.6 GeV.

b. the requirement of no energy deposit in the FCAL other than in the two inner rings or associated with a track was removed.

vi.2 The diffractive mass spectra of proton dissociative events in the inelastic MC simulation was varied, and the contribution from this background source reestimated: the value of β in $\frac{d\sigma}{dM_N^2} \propto 1/M_N^\beta$ was changed from 2.2 to 2.0 and 2.4.

vi.3 The efficiency for tagging proton dissociative events with the nominal FCAL energy cuts was estimated using a different MC simulation (EPSOFT [65]), and its impact on the contamination calculated.

As the contamination by proton dissociative events, integrated over the t range under study, was found to be independent of $W_{\gamma^* p}$ and Q^2 the checks in this class affect only the overall normalization of the cross sections determined as a function of these variables.

vi.4 For the study of the shape of the differential cross section $d\sigma/d|t|$, the additional check was also performed:

a. The t dependence of the proton dissociative contamination was varied, keeping the integrated contamination fixed, i.e., the slope parameter in expression 7.16 was changed from its nominal value 0.25 by its statistical error ±0.29.

vii. Other error sources In addition to the errors estimated with the checks above, other factors contribute to the systematic error of the measurements:

Uncertainty on the subtraction of background sources other than proton dissociative events (see section 7.4).

Uncertainty on trigger efficiencies (see section 7.3.2).

Uncertainty of photon flux determination (see section 9.4).

Uncertainty on radiative corrections (see section 7.1.2).

Uncertainty on the luminosity measurement.

All these effects have been considered to be independent of the variables under study, and contribute therefore to an overall normalization error.

In the following chapter, whenever a result was obtained from a fit, it should be understood that the corresponding systematic uncertainty was determined repeating the fit after each systematic check and adding in quadrature the deviations from the nominal values corresponding to all relevant error sources.

Chapter 9

Results and discussion

In this chapter the results obtained in the analysis are presented and discussed. First, the ρ^0 mass shape and the shape of the differential distribution $d\sigma^{\gamma^*p\rightarrow\pi^+\pi^-p}/d|t|$ are shown. Evidences of shrinkage in the data are investigated. Then the results on angular decay distributions are discussed and, finally, the $\gamma^*p \rightarrow \rho^0p$ production cross section is presented, as a function of Q^2 and W_{γ^*p} .

9.1   The shape of the $M_{\pi\pi}$ spectrum

At the Q^2 values covered in this analysis the $\pi^+\pi^-$ mass distribution in the region of the ρ^0 meson shows a distortion when compared to a relativistic Breit-Wigner function, with an enhancement of low masses and a suppression of high masses (see, for example, figure 9.2). This was previously observed in photoproduction [99, 9] and is often referred to as *skewing*. Several different parameterizations have been suggested to describe this shape. In the present analysis, the following models have been investigated:

- Söding model:

Söding [93] has proposed a model to describe the $\pi^+\pi^-$ mass spectrum. It assumes that the observed shape results from the interfering sum of a relativistic p-wave Breit-Wigner function, corresponding to ρ^0 production, with a non-resonant $\pi^+\pi^-$ background [36, 31] (known as the Drell-Hiida-Deck background), as pictured in the diagrams of figure 9.1. It is the interference between this two type of processes that is responsible for the distortion of the mass shape.

Two implementations of this model were studied:

- Simple Söding parameterization:

In this case, a real, non-resonant background B, constant in mass [1], was added to the pure ρ^0 term in the expression for $\pi^+\pi^-$ production amplitude:

---

[1] An alternative parameterization of the background as a first order polynomial in $M_{\pi\pi}$ was also investigated, and the result was consistent with a flat distribution.
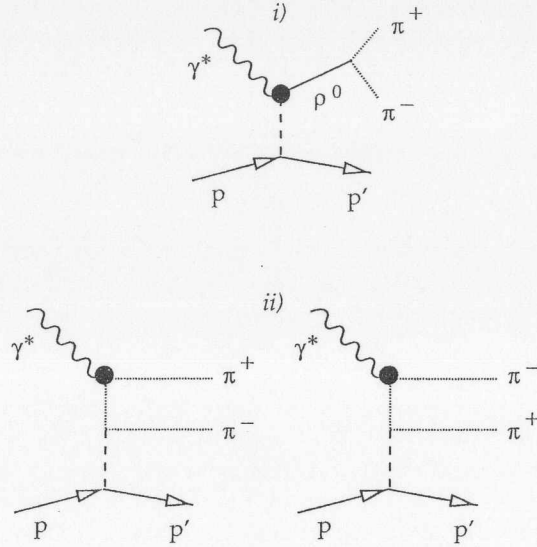
Figure 9.1: Processes in the Söding model: *i)* ρ^0 production and *ii)* non-resonant pion production.

$$dN_{corr}/dM_{\pi\pi} = \left| A\left(\frac{\sqrt{M_{\pi\pi}M_\rho\Gamma_\rho}}{M_{\pi\pi}^2 - M_\rho^2 + iM_\rho\Gamma_\rho} + \frac{B}{A} \right) \right|, \qquad (9.1)$$

with the resonant contribution described by a relativistic Breit-Wigner BW:

$$BW(M_{\pi\pi}) = \frac{M_{\pi\pi}M_\rho\Gamma_\rho}{(M_{\pi\pi}^2 - M_\rho^2)^2 + M_\rho^2\Gamma_\rho^2}. \qquad (9.2)$$

This expression is a function of the nominal ρ^0 mass M_ρ and and its momentum dependent width,

$$\Gamma_\rho(M_{\pi\pi}) = \Gamma_0 \left(\frac{q^*}{q_0} \right)^3 \frac{M_\rho}{M_{\pi\pi}} \qquad (9.3)$$

where Γ_0 is the width of the ρ^0, q^* is the momentum of the pions in the $\pi^+\pi^-$ system rest frame, and q_0 is the value of of q^* at the nominal ρ^0 mass M_ρ.

This description of the mass shape was used to extract the nominal ρ^0 cross sections, as described later in this chapter.

– Spital and Yennie parameterization:

In the framework of the Söding model, Spital and Yennie have presented [95] their own prescription for the ρ^0 line shape:

$$dN/dM_{\pi\pi} = A^2 \, BW \left[1 + C_1 \left(1 - \frac{M_\rho}{M_{\pi\pi}} \right) + C_2 \left(1 - \frac{M_\rho}{M_{\pi\pi}} \right)^2 \right] \qquad (9.4)$$

where expression 9.2 was used to describe the relativistic Breit-Wigner function. This parameterization of the $\pi^+\pi^-$ mass spectrum is based on the assumption that the contributions of the non-resonant two pion production and its interference with ρ^0 production can be approximated, in the ρ^0 mass region, by the terms in C_1 (interference) and C_2 (non-resonant background). This approach has the caveat of treating the interference and non-resonant terms independently, therefore allowing non-physical solutions to equation 9.4.

● Ross and Stodolsky model:

Ross and Stodolsky [85] have presented an alternative to the Söding mechanism, which ignores the interference from non-resonant $\pi^+\pi^-$ pairs. In this approach, the skewing of the $\pi^+\pi^-$ mass distribution is interpreted as an extra mass dependence in the ρ^0 production amplitude itself. In photoproduction, for $t = 0$, this model yields

$$dN/dM_{\pi\pi} = A^2 \, BW \left(\frac{M_\rho^2}{M_{\pi\pi}^2} \right)^2. \qquad (9.5)$$

where A is a constant and BW is the relativistic Breit-Wigner in expression 9.2. However, the mass shape is expected to depend on t and on Q^2 (in electroproduction), therefore it is usual to parameterize the ρ^0 mass shape by a modified version of expression 9.5,

$$dN/dM_{\pi\pi} = A^2 \, BW \left(\frac{M_\rho^2}{M_{\pi\pi}^2} \right)^n. \qquad (9.6)$$

The acceptance corrected mass spectrum was fitted, in the range $0.6 < M_{\pi\pi} < 1.2$ GeV (50 MeV bins) according to the expressions above. Table 9.1 summarizes the results of these fits for the overall data sample ($0.25 < Q^2 < 0.85$ GeV^2, $20 < W_{\gamma^*p} < 0.85$ GeV, $|t| < 0.6$ GeV^2).

The fits according to the Söding and Ross-Stodolsky parameterizations, where the mass and width of the ρ^0 were left as free parameters, show a satisfactory χ^2/ndf.

The fitted values for the ρ^0 mass are in agreement with the PDG values ($M_\rho = 768.5 \pm 0.6$ MeV), whereas as the ρ^0 width, are slightly overestimated with respect to the PDG value ($\Gamma_\rho = 150.7 \pm 1.2$ MeV). The non-resonant background determined using the Söding parameterization amounts to $\sim 12\%$ of the events collected in the mass range 0.6-1.2 GeV. If an extra (non-interfering) constant term is added to expression 9.1, the result is compatible to the estimated background from photon dissociative and double dissociative events (3%, see section 7.4) but the introduction of one more parameter increases significantly the uncertainties of the fit.

The fit according to the Spital-Yennie parameterization was first performed with the mass and width of the ρ^0 as free parameters. This fit presents a very small χ^2/ndf and yields

Söding parameterization				
A	B/A	M_ρ (MeV)	Γ_0 (GeV)	χ^2/ndf
1363.0 ± 14.5	-0.471 ± 0.054	769.3 ± 4.1	159.2 ± 7.6	$6.1/8$

Spital-Yennie parameterization					
A	C_1	C_2	M_ρ(MeV)	Γ_0(GeV)	χ^2/ndf
1367.0 ± 20.0	-4.36 ± 0.50	6.97 ± 1.76	776.0 ± 5.0	154.5 ± 6.6	$1.1/7$
1376.8 ± 20.0	-3.64 ± 0.91	4.69 ± 0.35	768.1 (fixed)	155.3 ± 5.0	$3.9/8$

Ross-Stodolsky model				
A	n	M_ρ (MeV)	Γ_0 (GeV)	χ^2/ndf
1382.2 ± 15.2	3.61 ± 0.33	770.4 ± 4.1	158.5 ± 6.8	$5.2/8$

Table 9.1: Results of mass fits to all selected events, using different techniques (statistical errors only).

a ρ^0 mass higher than expected. With the ρ^0 mass fixed to that of the PDG, the fit gives a more reasonable χ^2/ndf. In both cases the width is compatible with the PDG values. The $\pi^+\pi^-$ mass fits were repeated in bins of Q^2, t and W_{γ^*p}, where the mass and width were fixed to the corresponding values for the overall sample, given in table 9.1 (in the Spital-Yennie fit the mass was fixed to the PDG value).

The results are shown in table 9.2, with the corresponding kinematic averages indicated in table 9.3.

The values of $-B/A$ (Söding fit) and n (Ross-Stodolsky fit), measurements of the amount of skewing in a sample, are shown in figures 9.2 and 9.3 as a function of Q^2 (only statistical errors are shown). The results of this analysis are compared to other results obtained at a similar average t value, $0.09 \lesssim \langle t \rangle \lesssim 0.12 \, \text{GeV}^2$, clearly showing that the mass distribution becomes more similar to a relativistic Breit-Wigner function as Q^2 increases.

Due to the small number of events collected at high $|t|$, a detailed study of the skewing as a function of this variable could not be performed. However, the results obtained for B/A and n in three t bins are shown in figures 9.4 and 9.5, and are compatible with a decrease of the skewing as the momentum transfer increase, as already observed in ρ^0 photoproduction at low energies and at HERA (see [99] and references therein).

As in previous analyses, no significant W_{γ^*p} dependence of the mass shape was observed in this data sample (see figure 9.6). This is further supported by the good agreement between the skewing parameter n obtained at low energies (E665,$\langle W_{\gamma^*p} \rangle \sim 18$ GeV) and at HERA ($\langle W_{\gamma^*p} \rangle \sim 50 - 70$ GeV) seen in figure 9.3.

Söding parameterization				
Q^2 (GeV^2)	W_{γ^*p} (GeV)	$|t|$ (GeV^2)	B/A	χ^2/ndf
0.25-0.85	20-90	0-0.6	-0.471 ± 0.054	6.1/8
0.25-0.45	20-90	0-0.6	-0.497 ± 0.033	7.6/10
0.45-0.85			-0.443 ± 0.039	5.1/10
0.25-0.85	20-35	0-0.6	-0.504 ± 0.034	8.0/10
	35-55		-0.448 ± 0.043	8.9/10
	55-90		-0.453 ± 0.048	6.0/10
0.25-0.85	20-90	0-0.1	-0.544 ± 0.035	6.2/10
		0.1-0.3	-0.440 ± 0.036	4.7/10
		0.3-0.6	-0.380 ± 0.039	9.7/10

Spital-Yennie model					
Q^2 (GeV^2)	W_{γ^*p} (GeV)	$|t|$ (GeV^2)	C_1	C_2	χ^2/ndf
0.25-0.85	20-90	0-0.6	-3.64 ± 0.91	4.69 ± 0.35	3.9/8
0.25-0.45	20-90	0-0.6	-3.77 ± 0.11	4.89 ± 0.42	4.4/10
0.45-0.85			-3.47 ± 0.16	4.37 ± 0.58	4.7/10
0.25-0.85	20-35	0-0.6	-3.65 ± 0.12	3.98 ± 0.46	5.3/10
	35-55		-3.68 ± 0.17	5.50 ± 0.65	7.3/10
	55-90		-3.54 ± 0.20	4.60 ± 0.76	3.9/10
0.25-0.85	20-90	0-0.1	-4.13 ± 0.11	5.75 ± 0.43	3.9/10
		0.1-0.3	-3.23 ± 0.15	3.20 ± 0.58	3.5/10
		0.3-0.6	-3.00 ± 0.19	3.59 ± 0.69	9.3/10

Ross-Stodolsky parameterization				
Q^2 (GeV^2)	W_{γ^*p} (GeV)	$|t|$ (GeV^2)	n	χ^2/ndf
0.25-0.85	20-90	0-0.6	3.61 ± 0.33	5.2/8
0.25-0.45	20-90	0-0.6	3.78 ± 0.20	6.6/10
0.45-0.85			3.42 ± 0.29	5.1/10
0.25-0.85	20-35	0-0.6	3.79 ± 0.23	7.8/10
	35-55		3.49 ± 0.33	8.8/10
	55-90		3.47 ± 0.34	5.9/10
0.25-0.85	20-90	0-0.1	4.10 ± 0.23	5.5/10
		0.1-0.3	3.36 ± 0.26	4.1/10
		0.3-0.6	2.95 ± 0.30	10.2/10

Table 9.2: Results of the mass shape parameters using different subsamples (statistical errors only).
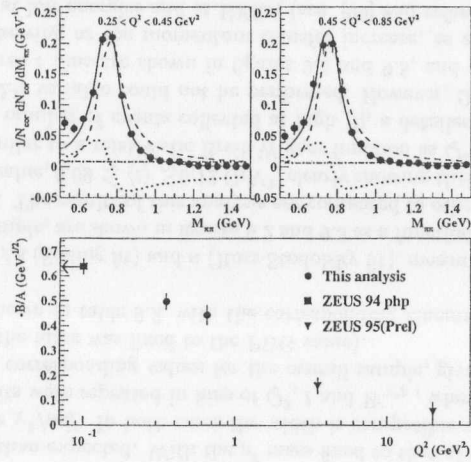
Figure 9.2: Söding fit and B/A for different Q^2 values (statistical errors only). The mass spectrum is shown beyond the fit range of 0.6-1.2 GeV. The other samples compared, [99] (photoproduction point indicated by an arrow) and results in preparation by the ZEUS collaboration, have similar average t.
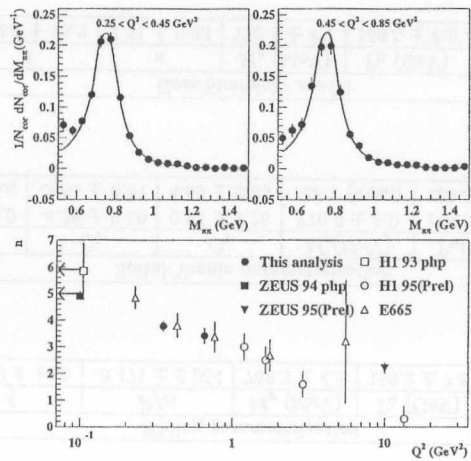
Figure 9.3: Ross-Stodolsky fit and n for different Q^2 values (statistical errors only). The mass spectrum is shown beyond the fit range of 0.6-1.2 GeV. The other samples compared, [99], [53] (photoproduction points indicated by an arrow), [37], [56], and [10] have similar
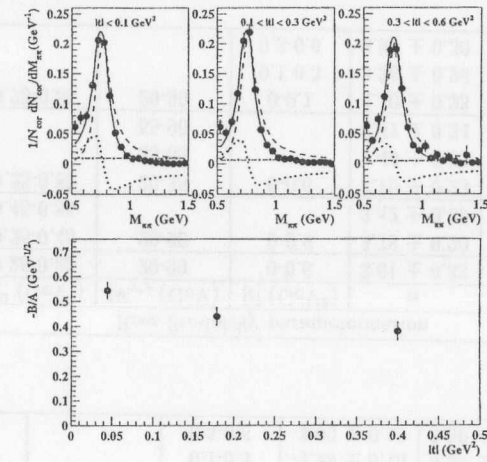
Figure 9.4: Söding fit and B/A for different $|t|$ values (statistical errors only). The mass spectrum is shown beyond the fit range of 0.6-1.2 GeV.
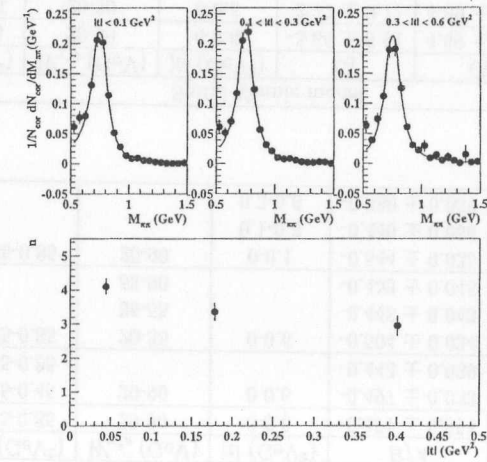
Figure 9.5: Ross-Stodolsky fit and n for different $|t|$ values (statistical errors only). The mass spectrum is shown beyond the fit range of 0.6-1.2 GeV.

Q^2 (GeV^2)	$\langle Q^2 \rangle$ (GeV^2)
0.25-0.85 (full range)	0.45
0.25-0.45	0.33
0.45-0.85	0.62

W_{γ^*p} (GeV)	$\langle W_{\gamma^*p} \rangle$ (GeV)
20-90 (full range)	47
20-35	27
35-55	45
55-90	71

$|t|$ (GeV^2)	$\langle |t| \rangle$ (GeV^2)
0-0.6 (full range)	0.12
0-0.1	0.04
0.1-0.3	0.18
0.3-0.6	0.40

Table 9.3: Binning used in mass fits.
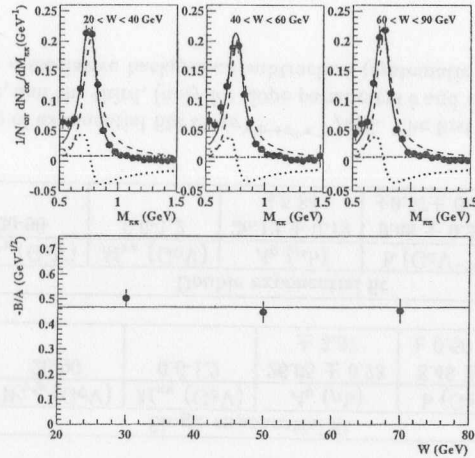
Figure 9.6: Söding fit and B/A for different W_{γ^*p} values (statistical errors only). The mass spectrum is shown beyond the fit range of 0.6-1.2 GeV.
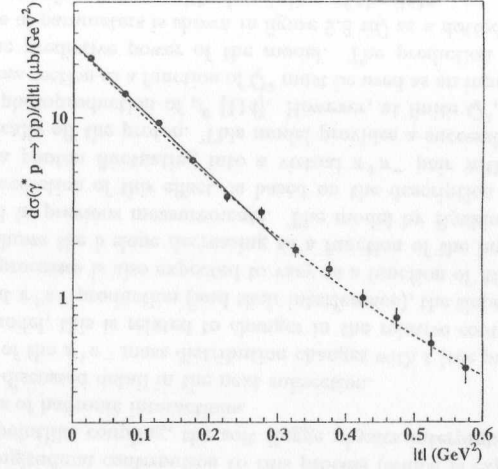
Figure 9.7: The $d\sigma^{\gamma^*p \to \pi^+\pi^-p}/d|t|$ distribution (statistical errors only), with superimposed results of fits to a single exponential function for $|t| < 0.3$ GeV^2 (solid line) and to a double exponential function for $|t| < 0.6$ GeV^2 (dashed line).

9.2 The $|t|$ distribution

The differential distribution $d\sigma^{\gamma^*p \to \pi^+\pi^-p}/d|t|$ was studied for events produced in the ρ^0 mass region ($0.6 < M_{\pi\pi} < 1.2$ GeV) and for $|t| < 0.6$ GeV^{-2} (limited by statistics).

This distribution, displayed in figure 9.7 for the full data set, exhibits an exponential shape, with a forward peak characteristic of diffractive processes. However, as observed in previous ρ^0 production measurements, it cannot be fitted over all the t range by a single exponential function.

In this analysis, two fits to the $d\sigma^{\gamma^*p \to \pi^+\pi^-p}/d|t|$ were performed:

- a single exponential fit, limited to the range $|t| < 0.3$ GeV^{-2}

$$\frac{d\sigma^{\gamma^*p \to \pi^+\pi^-p}}{d|t|} = A_0 e^{-b|t|}, \tag{9.7}$$

- a double exponential *ansatz*, for $|t| < 0.6$ GeV^{-2}

$$\frac{d\sigma^{\gamma^*p \to \pi^+\pi^-p}}{d|t|} = A_0 e^{-b|t|+ct^2}, \tag{9.8}$$

Single exponential fit					
Q^2 (GeV^2)	W_{γ^*p} (GeV)	$M_{\pi\pi}$ (GeV)	A_0 (μb)	b (GeV^{-2})	χ^2/ndf
0.25-0.85	20-90	0.6-1.2	26.05 ± 0.78 ± 3.87	8.48 ± 0.24 ± 0.50 ±0.50	6.8/4

Double exponential fit						
Q^2 (GeV^2)	W_{γ^*p} (GeV)	$M_{\pi\pi}$ (GeV)	A_0 (μb)	b (GeV^{-2})	c (GeV^{-4})	χ^2/ndf
0.25-0.85	20-90	0.6-1.2	26.12 ± 0.79 ±5.84	9.48 ± 0.34 ±0.57± 0.45	3.93 ± 0.73 ±0.81± 0.35	5.7/9

Table 9.4: Results of exponential fits to $d\sigma^{\gamma^*p\to\pi^+\pi^-p}/d|t|$. The first error is statistic, the second systematic, and the third, (only for slope parameters b and c) is due to uncertainties in the proton dissociative background subtraction (systematic checks of class VI in previous chapter).

Single exponential fit				
Q^2 (GeV^2)	W_{γ^*p} (GeV)	$M_{\pi\pi}$ (GeV)	b (GeV^{-2})	χ^2/ndf
0.25-0.85	20-90	0.6-1.2	8.48 ± 0.24 ± 0.50	6.8/4
0.25-0.85	20-30	0.6-1.2	7.64 ± 0.59 ± 0.82	3.8/4
	30-40		8.84 ± 0.76 ± 1.15	4.9/4
	40-60		8.76 ± 0.54 ± 0.43	0.9/4
	60-90		9.01 ± 0.60 ± 0.66	1.5/4
0.25-0.45	20-90	0.6-1.2	8.56 ± 0.37 ± 0.56	3.2/4
0.45-0.85			8.33 ± 0.58 ± 0.85	2.4/4
0.25-0.45	20-90	0.6-0.7	9.66 ± 0.69 ± 0.77	0.5/4
		0.7-0.8	8.54 ± 0.45 ± 0.55	4.9/4
		0.8-1.2	7.82 ± 0.55 ± 0.58	2.3/4

Table 9.5: Results of exponential fits to $d\sigma^{\gamma^*p\to\pi^+\pi^-p}/d|t|$ in bins of Q^2, W_{γ^*p} and $M_{\pi\pi}$. The first error is statistic and the second systematic. An extra error on the slope parameter b of ±0.5 GeV^{-2} due to uncertainties in the proton dissociative background subtraction is not included in the table (systematic checks of class VI in previous chapter).

Q^2 (GeV^2)	$\langle Q^2 \rangle$ (GeV^2)
0.25-0.85 (full range)	0.45
0.25-0.45	0.33
0.45-0.85	0.62

W_{γ^*p} (GeV)	$\langle W_{\gamma^*p} \rangle$ (GeV)
20-90 (full range)	47
20-30	25
30-40	35
40-60	50
60-90	74

Table 9.6: Binning used in $d\sigma^{\gamma^*p\to\pi^+\pi^-p}/d|t|$ fits.

The results of these fits to the full data sample are presented in table 9.4.

The single exponential fits to $d\sigma^{\gamma^*p\to\pi^+\pi^-p}/d|t|$ for $|t| < 0.3$ GeV^{-2} were repeated in bins of Q^2, W_{γ^*p} and $M_{\pi\pi}$. The results are presented in table 9.5 and the average values of the kinematic variables in the fitted subsamples are given in table 9.6.

Figure 9.8 i) shows the extracted b slope as a function of Q^2. These results, together with the photoproduction and higher Q^2 points displayed in the figure [2], give an indication that the slope parameter b, related to the size of the interaction, decreases with Q^2. This decrease is expected as pQCD becomes more applicable with increasing Q^2: while in pQCD the longitudinal contribution to this process (which is expected to dominate) proceeds via a pointlike coupling, the soft Regge physics interprets the photon proton collision in terms of hadronic interactions.

Figure 9.8 ii) is discussed detail in the next subsection.

Since the shape of the $\pi^+\pi^-$ mass distribution changes with t (see previous section) and, in the Söding model, this is related to changes in the relative contribution of resonant and non-resonant $\pi^+\pi^-$ production (and their interference), the slope parameter b for the sum of the two processes is also expected to vary as a function of $M_{\pi\pi}$.

Figure 9.8 iii) shows the b slope decreasing as a function of the invariant pion mass, a feature observed in previous measurements. The model by Ryskin and Shabelski [87], which gives a prediction of this effect, is based on the description of the non-resonant background as a photon fluctuating into a virtual $\pi^+\pi^-$ pair with one or both pions scattering elastically off the proton. This model provides a successful description of the data on elastic photoproduction of ρ^0 [114]. However, at finite Q^2, the behavior of the resonant (ρ^0) cross section as a function of Q^2 must be used as an input to the calculations and restricts the predictive power of the model. The prediction of this model for a particular choice of parameters is shown in figure 9.8 iii) as a dotted line (courtesy of A. Proskuryakov), and gives a reasonable description of the data.

---

[2]It should be emphasized that this kind of comparisons only makes sense for points extracted with the same functional form, for the same t range.

Error source	Uncertainty (GeV^{-2})
Tracking requirements	0.36
BPC requirements	0.15
Matching	0.27
Elastic MC parameterizations	0.13
Proton dissociative $\pi\pi$	0.50
Total uncertainty	$0.50 \oplus 0.50$(pdis)

Table 9.7: Overview of the systematic uncertainties of the slope parameter b for the single exponential fit to the full data sample. The contribution due to uncertainties in the proton dissociative background subtraction(systematic checks of class VI in previous chapter) is presented separately.

9.2.1 Shrinkage of the t distribution.

As described in section 2.5.2, in the framework of Regge models, the $d\sigma^{\gamma^* p \to \pi^+ \pi^- p}/d|t|$ distribution is expected to change with energy, with the forward peak getting sharper with the the logarithm of the energy. This *shrinkage* of the $d\sigma^{\gamma^* p \to \pi^+ \pi^- p}/d|t|$ distribution can be expressed in terms of the the slope of the Pomeron trajectory, α', as presented in expression 2.60.

On the other hand, pQCD calculations expect no dependence of b on $W_{\gamma^* p}$.

In the BPC analysis the evidence for shrinkage in $\pi^+ \pi^-$ production (without ρ^0 extraction) was investigated. The simplest way to study this is to fit the single exponential b slopes, determined at different energies, as a function of $W_{\gamma^* p}$:

$$b = b_0 + 4\ln(W_{\gamma^* p})\alpha', \tag{9.9}$$

where b_0 is a constant. The result of this fit is

$$\alpha' = 0.29 \pm 0.19 \pm 0.20 \text{GeV}^{-2} \tag{9.10}$$

As usual, the systematic error was determined repeating the fit to the b values determined for each of the systematic checks listed in the previous chapter, with the exception of error of class IV and VII (class IV refers to uncertainties in the extraction of the ρ^0 signal, while this study refers to $\pi^+ \pi^-$ events in the mass region 0.6-1.2 GeV; uncertainties of class VII affect only the normalization of the events, not the shapes of the distributions.).

The errors in this fit are too large to make conclusive statements, however, an alternative method was used, which better accounts for migrations between bins, providing more accurate results. The method consists of reweighting iteratively the energy ($W_{\gamma^* p}$) and t dependence of the generated Monte Carlo events according to

$$d\sigma^{\gamma^* p \to \pi^+ \pi^- p}/d|t| \propto e^{b_0|t|+c_0 t^2} \cdot (W_{\gamma^* p}/W_0)^{4[(\alpha(0)-1)-\alpha'|t_g|]}, \tag{9.11}$$

where t and $W_{\gamma^* p}$ are the generated variables, W_0 is an arbitrary constant and b_0, c_0, $\alpha(0)$ and α' are the parameters tuned until the best agreement of the simulated and measured distributions was achieved.

Figure 9.8: b slope as a function of $i)$ Q^2, $ii)$ $W_{\gamma^* p}$ and $iii)$ $M_{\pi\pi}$. The inner error bars represent statistical uncertainties; the outer error bars indicate the quadratic sum of statistical and systematic uncertainties. The shaded areas indicate additional normalization uncertainties due to the proton dissociation background subtraction. The BPC points are compared to those of [99] (photoproduction point indicated by an arrow), adapted using equivalent functional form, and to ZEUS high Q^2 results in preparation, fitted in the same t range. The solid line is the result of the bidimensional shrinkage fit described in the text. The dashed line indicates the predictions of a Söding model calculation (see text).

Bidimensional shrinkage fit		
$\alpha(0)$	α' (GeV^{-2})	χ^2/ndf
$1.055 \pm 0.016 \pm 0.019$	$0.194 \pm 0.088 \pm 0.090$	$34/32$

Table 9.8: Results of bidimensional shrinkage fits. The first error is statistical, the second systematic.

The difference between data and MC was minimized with respect to $b_0, c_0, \alpha(0)$ and α' using a χ^2 fit to 36 (t, W_{γ^*p}) bins, following the method described by [115]:

$$\chi^2 = \sum_\mu \frac{(d'_\mu - c_N m'_\mu(\lambda))^2}{\delta^2_\mu(\lambda)} \qquad (9.12)$$

where λ stands for the parameter(s) being fitted, d'_μ and m'_μ are the weighted sum of events in bin μ for data (background subtraction) and MC respectively, $c_N = \frac{\sum d'_\mu}{\sum m'_\mu}$ and

$$\delta^2_\mu = c_N m'_\mu \left(\frac{d'_\mu}{\tilde{d}'_\mu} + \frac{c_N m'_\mu}{\tilde{m}'_\mu} \right). \qquad (9.13)$$

Here $\tilde{d}'_\mu$ and $\tilde{m}'_\mu$ are the equivalent number of events.

Given that the number of events in each bin, for both data and MC, is always larger than 30, the use of a χ^2 fit (which assumes Gaussian rather than Poisson distributions) is justified. The minimization and corresponding errors on parameters were calculated using the MINUIT package [74].

Since the subtraction of proton dissociative background from the data sample was independent of W_{γ^*p}, this study is valid under the assumption of a similar shrinkage in the elastic and inelastic processes.

The systematic error was evaluated repeating the fit for the systematic checks listed for classes I, II, III and V. In addition, the bins in $|t|$ and W_{γ^*p} used in the fit were varied. The results were quite stable throughout most checks, with the largest uncertainties arising from changes in the tracking cuts and usage of different binning (see table 9.9.)

This fit is compatible with the observation of shrinkage within the a single experiment, and the results are in agreement with $\alpha(0) = 1.08$ and $\alpha' = 0.25$ obtained from fits to pp and $p\bar{p}$ data [35].

Figure 9.8 $ii)$ displays the fitted b slopes as a function of W_{γ^*p} for the sample in study (table 9.5). The result of a bidimensional fit, described above is overlayed.

Table 9.2.1 shows the pull between data and MC ($\chi = (d'_\mu - c_N m'_\mu)/\delta_\mu$) obtained in each bin for the MC reweighted according to the set of values to which the fit converged to. The magnitude and signs of the χ^2 are apparently randomly distributed, thus there is no evidence for systematic deviations. The only significant correlation observed is between parameters b_0 and c_0 which show a correlation parameter of 0.94.

Error source	Uncertainty in $\alpha(0)$	Uncertainty in α'
Tracking requirements	0.010	0.065
BPC requirements	0.004	0.017
Matching	0.007	0.014
Elastic MC parameterizations	0.004	0.008
Binning	0.014	0.058
Total uncertainty	0.019	0.090

Table 9.9: Overview of the systematic uncertainties on $\alpha_{\mathbb{P}}$ measurements.

	W_1	W_2	W_3	W_4	W_5	W_6
t_1	-0.10	-0.08	+0.66	-0.35	-0.08	-0.13
t_2	-0.18	+1.15	-0.69	+0.54	+1.67	-0.06
t_3	+1.88	-0.11	-0.82	+1.78	+0.20	+0.56
t_4	+0.92	-1.21	+0.37	-0.92	-0.89	-0.62
t_5	+0.64	-0.47	-0.03	+2.92	-0.94	-1.40
t_6	-0.49	+0.18	-1.20	+0.43	-0.42	+1.39

Table 9.10: Individual χ in each bin for the bidimensional fit to the energy dependence of the diffractive peak (shrinkage).

9.3   The ρ^0 polarization

As discussed in the section 2.7, the angular decay distribution of ρ^0's produced in the collision of unpolarized beams can be described by 15 spin density matrix elements, relating the three decay angles θ_h, Φ_h and ϕ_h. However, in this analysis, we present results under the assumption of SCHC. In that case, only three parameters are non-zero: r_{00}^{04}, r_{1-1}^1 and $\mathrm{Re}(r_{10}^5)$. These can be extracted by a two dimensional fit to the uncorrected angular distributions in terms of the two independent angles θ_h and Ψ_h, using a similar method to the one described in the previous section.

To determine these non-zero matrix elements for $\pi^+\pi^-$ events in the ρ^0 mass region (0.6-1.2 GeV), the elastic ρ^0 MC sample was reweighted iteratively according to expression 2.74, while maximizing the likelihood function [115]

$$\ln L(\lambda) = \sum_\mu d'_\mu \ln(c_N m'_\mu) - c_N m'_\mu \qquad (9.14)$$

where λ stands for the parameter(s) being fitted, d'_μ and m'_μ are the events in bin μ for data and MC (m'_μ is a sum of weighted events) and $c_N = \sum \frac{d'_\mu}{m'_\mu}$.

The data and MC events were binned in 64 (θ_h, Ψ) bins, and the fit results and corresponding errors were calculated using the MINUIT package [74].

The results of these fits to the full data sample, and to subsamples in Q^2, W_{γ^*p} and $M_{\pi\pi}$ are presented in table 9.11 (the mean W_{γ^*p} and Q^2 in each bin can be found in table 9.6). The χ^2/ndf calculated from the final parameters of each fit are also given in table 9.11 and the pull, in each bin, between reconstructed data and MC reweighted to the fit results for the full sample is shown in table 9.3 in terms of $\chi = (d'_\mu - c_N m'_\mu)/\delta_\mu$ (where δ is defined in equation 9.13). The highest correlation parameter in the fit, between r_{00}^{04} $\mathrm{Re}(r_{10}^5)$ is 0.50. The comparison between the measured values of r_{1-1}^1 and those predicted from the measured r_{00}^{04} through expression 2.75, valid for a process where s-channel helicity is conserved and which proceeds by an exchange of particle(s) with natural parity (see section 2.7), reveals consistency with these assumptions (see table 9.11).

The discussion on the behavior of r_{00}^{04} with Q^2, W_{γ^*p} and $M_{\pi\pi}$ is postponed to the next section.

All the results listed in table 9.11 are in agreement with those obtained by simple one dimensional fits to the angular distributions integrated over one of the angles θ_h and Ψ_h, as can be seen, as an example, in figures 9.9 and 9.10.

Table 9.13 summarizes the impact of the different error sources on the measurements of the spin density matrix for the full data sample. The systematic error was evaluated repeating the fit for the systematic checks listed for classes I, II, III and V. In addition, the bins used in the fit were varied. The results were quite stable throughout most checks, with the largest uncertainties arising from changes in the MC parameterizations and usage of different binning (see table 9.9.)
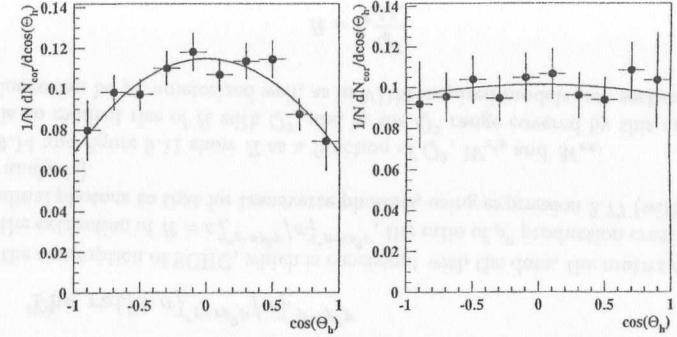

Figure 9.9: Acceptance corrected $\cos\theta_h$ distribution for two Q^2 bins (statistical errors only). Overlayed are the results of the bidimensional fit described in the text.
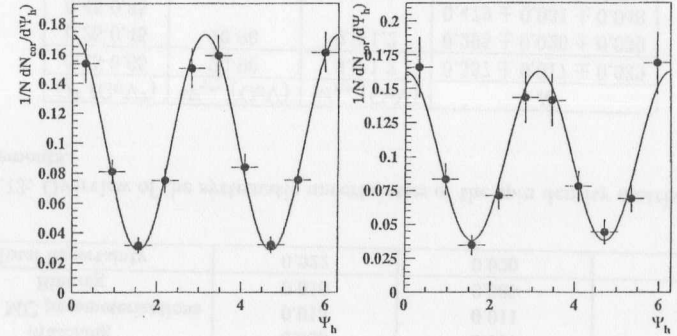

Figure 9.10: Acceptance corrected Ψ_h distribution for two Q^2 bins (statistical errors only). Overlayed are the results of the bidimensional fit described in the text.

Q^2 (GeV^2)	$W_{\gamma^* p}$ (GeV)	$M_{\pi\pi}$ (GeV)	r^{04}_{00}	r^1_{1-1}	Re(r^5_{10})	χ^2/ndf	Predicted r^1_{1-1}
0.25-0.85	20-90	0.6-1.2	0.263 ± 0.009 ± 0.021	0.340 ± 0.006 ± 0.020	0.140 ± 0.002 ± 0.009	69/61	0.368 ± 0.011
0.25-0.45	20-90	0.6-1.2	0.228 ± 0.012 ± 0.023	0.357 ± 0.009 ± 0.022	0.133 ± 0.004 ± 0.009	65/61	0.386 ± 0.013
0.45-0.85			0.324 ± 0.014 ± 0.022	0.311 ± 0.011 ± 0.030	0.156 ± 0.004 ± 0.010	49/61	0.338 ± 0.013
0.25-0.85	20-35	0.6-1.2	0.295 ± 0.017 ± 0.029	0.319 ± 0.011 ± 0.032	0.150 ± 0.005 ± 0.011	62/59	0.352 ± 0.017
	35-55		0.260 ± 0.015 ± 0.021	0.346 ± 0.014 ± 0.024	0.136 ± 0.004 ± 0.010	75/61	0.370 ± 0.013
	55-90		0.231 ± 0.018 ± 0.024	0.359 ± 0.013 ± 0.023	0.132 ± 0.005 ± 0.010	63/61	0.384 ± 0.015
0.25-0.85	20-90	0.6-0.7	0.329 ± 0.019 ± 0.026	0.294 ± 0.013 ± 0.025	0.155 ± 0.004 ± 0.010	59/61	0.335 ± 0.016
		0.7-0.8	0.270 ± 0.012 ± 0.024	0.345 ± 0.009 ± 0.024	0.151 ± 0.004 ± 0.012	95/61	0.365 ± 0.013
		0.8-1.2	0.211 ± 0.018 ± 0.025	0.366 ± 0.012 ± 0.031	0.110 ± 0.005 ± 0.011	50/61	0.394 ± 0.015

Table 9.11: ρ^0 spin density matrix elements measured assuming s-channel helicity conservation. The first error corresponds to the statistical and the second one to the systematic uncertainty. The last column shows the value of r^1_{1-1} calculated from r^{04}_{00} using expression 2.75. The mean values of $W_{\gamma^* p}$ and Q^2 in each bin are those of table 9.3.

	Ψ_1	Ψ_2	Ψ_3	Ψ_4	Ψ_5	Ψ_6	Ψ_7	Ψ_8
θ_1	+0.05	-2.08	-0.70	+1.27	+0.48	+0.66	-0.27	+0.86
θ_2	+0.80	+1.12	-1.28	+0.44	-1.18	-0.56	-0.92	-0.03
θ_3	+0.49	+1.58	-0.92	-1.48	-0.29	-0.14	-1.01	+1.50
θ_4	-0.08	+2.69	+0.45	+0.27	-2.10	+0.04	-0.78	+0.70
θ_5	-1.86	+0.84	+0.08	-1.24	+0.08	-0.33	+0.19	-0.28
θ_6	+1.35	+0.55	-0.74	+0.05	+0.88	+1.76	-0.44	+0.20
θ_7	+0.95	+1.85	-0.95	+0.51	+0.34	-0.22	-0.56	-0.15
θ_8	-1.03	-0.44	-0.84	-1.38	-0.21	+0.43	-1.95	+2.28

Table 9.12: Individual χ in each bin for the bidimensional fit to the angular distributions of the full data sample.

Error source	Uncertainty in r^{04}_{00}	Uncertainty in r^1_{1-1}	Uncertainty in Re(r^5_{10})
Tracking requirements	0.009	0.014	0.004
BPC requirements	0.005	0.005	0.002
Matching	0.008	0.007	0.005
Elastic MC parameterizations	0.015	0.011	0.006
Binning	0.010	0.005	0.004
Total uncertainty	0.022	0.020	0.009

Table 9.13: Overview of the systematic uncertainties of the spin density matrix elements measurements.

Q^2 (GeV^2)	$W_{\gamma^* p}$ (GeV)	$M_{\pi\pi}$ (GeV)	R
0.25-0.85	20-90	0.6-1.2	$0.357 \pm 0.017 \pm 0.039$
0.25-0.45	20-90	0.6-1.2	$0.295 \pm 0.020 \pm 0.039$
0.45-0.85			$0.479 \pm 0.031 \pm 0.048$
0.25-0.85	20-35	0.6-1.2	$0.418 \pm 0.034 \pm 0.058$
	35-55		$0.351 \pm 0.027 \pm 0.038$
	55-90		$0.300 \pm 0.030 \pm 0.041$
0.25-0.85	20-90	0.6-0.7	$0.490 \pm 0.042 \pm 0.057$
		0.7-0.8	$0.370 \pm 0.022 \pm 0.045$
		0.8-1.2	$0.267 \pm 0.029 \pm 0.040$

Table 9.14: R , measured assuming s-channel helicity conservation. The first error corresponds to the statistical and the second one to the systematic uncertainty.

9.3.1 The ratio $\sigma_L^{\gamma^* p \to \rho^0 p} / \sigma_T^{\gamma^* p \to \rho^0 p}$

Under the assumption of SCHC, which is consistent with the data, the matrix element r^{04}_{00} allows the extraction of $R = \sigma_L^{\gamma^* p \to \rho^0 p} / \sigma_T^{\gamma^* p \to \rho^0 p}$, the ratio of ρ^0 production cross section for longitudinal photons to that for transverse photons, using expression 2.77 (with $\varepsilon > 0.995$ in this analysis).
Table 9.14 and figure 9.11 show R as a function of Q^2, $W_{\gamma^* p}$ and $M_{\pi\pi}$.
There is an evident rise of R with Q^2, and in the Q^2 range covered by this analysis this dependence can be parameterized well, as in VDM inspired models (see section 2.5.1), by

$$R = \xi_\rho \frac{Q^2}{M_\rho} \tag{9.15}$$

The result of such a fit to the BPC points is given in table 9.15. The value of ξ_ρ measured in this way is compatible to that obtained by a bidimensional fit of the full data sample to equation 2.76, in which natural parity exchange is assumed, and R is parameterized as in expression 9.15. The results of this last fit are presented in table 9.16 (only statistical errors are shown), and shows that the transverse and longitudinal ρ^0 production
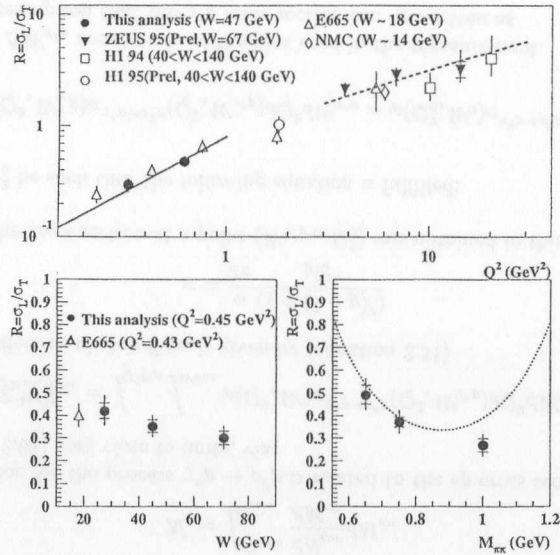
Figure 9.11: R as a function of $i)$ Q^2, $ii)$ $W_{\gamma^* p}$ and $iii)$ $M_{\pi\pi}$. The inner error bars represent statistical uncertainties; the outer error bars indicate the quadratic sum of statistical and systematic uncertainties. The BPC points are compared to those of other experiments [37], [76], [56], [54] and to ZEUS high Q^2 results in preparation. The solid line is the result of the fit of equation 9.15 to the BPC points. The dashed line is a prediction of the model by Martin, Ryskin and Teubner [73] using the ZEUS 94 NLO parameterization of the gluon density. The dotted line indicates the predictions of a Söding model calculation.

VDM fit	
ξ_ρ	χ^2/ndf
$0.48 \pm 0.03 \pm 0.03$	$1.4/1$

Table 9.15: Result of VDM fit to $R(Q^2)$, according to SCHC (expression 9.15).

SCHC and Natural Parity fit		
ξ_ρ	$\cos\delta$	χ^2/ndf
0.54 ± 0.05	0.94 ± 0.02	$77/61$

Table 9.16: Result of fit to the decay angular distributions according to SCHC and natural parity exchange (expression 2.76). Only statistical errors are shown.

amplitudes are almost in phase (i.e. $\cos\delta \sim 1$).

From figure 9.11 $i)$ it is clear that the linear dependence of R on Q^2 is much too steep to describe the data at higher Q^2. The pQCD calculations of Martin, Ryskin and Teubner (dashed line), which use a *parton-hadron duality* assumption to understand the (non-perturbative) transverse component of the cross section provide a description in this region (see [73], [10]).

Figure 9.11 $ii)$ shows R as a function of $W_{\gamma^* p}$, which is basically flat, with indications of a slight falloff. Although the pQCD model of Martin, Ryskin and Teubner predicts a slightly rising R with $W_{\gamma^* p}$, the errors of the data points are too large to draw conclusions. Variations of the spin matrix elements with $M_{\pi\pi}$ have been observed in low energy photoproduction [7], and have been ascribed to the non-resonant $\pi^+\pi^-$ production. In the calculations from Ryskin and Shabelsky for the Söding model in electroproduction (see section 9.2), a change of R with the two pion invariant mass is expected (see dotted line in figure 9.11 $iii)$). However, in the words of the authors of the model 'one must not take the predictions (...) too seriously for large $M_{\pi\pi}$. The interference with the next (heavier) resonances (...) was not taken into account (...) but at $M_{\pi\pi} > 1.1$ GeV their contribution can be significant' [87].

The pQCD model by Martin, Ryskin and Teubner also suggest a dependence of R on $M_{\pi\pi}$. However, all that can be stated so far is that the model predicts that R should be smaller for higher masses [10].

9.4 The extraction of the ρ^0 cross section

Due to the large width and complicated shape of the $\pi^+\pi^-$ mass distribution, the ρ^0 signal cannot be defined in an unambiguous way. In this analysis the ρ^0 production cross section was measured in the framework of the Söding model and systematic studies (listed in the previous chapter) were performed to investigate the change in the results had other approaches been used.

In this study, the elastic $ep \to e\rho^0 p$ cross section in a bin of Q^2 and $W_{\gamma^* p}$ was evaluated according to:

$$\sigma^{ep \to e\rho^0 p}_{Q2bin, Wbin} = \frac{\mathcal{N}_\rho}{\mathcal{L}} \tag{9.16}$$

where $\mathcal{L}$ is the effective integrated luminosity of the sample, and $\mathcal{N}_\rho$, described below, is the number of elastic ρ^0 events, corrected for the generalized acceptance Acc (see section 7.3, in bins of mass, Q^2 and $W_{\gamma^* p}$, and for proton dissociative background, as described in chapter 7.

$\mathcal{N}_\rho$ is obtained by fitting the corrected ρ^0 mass shape to a simplified prescription, according to the Söding model (equation 9.1), and integrating the Relativistic Breit-Wigner function, multiplied by its normalization factor, from the ρ^0 production kinematical threshold $M_{min} = 2M_\pi$ to $M_{max} = M_\rho + 5\Gamma_\rho$ (with the mass and width of the ρ^0 as given in [80]):

$$\mathcal{N}_\rho = \int_{M_{min}}^{M_{max}} \frac{dN_{cor}}{dM_{\pi\pi}} dM_{\pi\pi} \tag{9.17}$$

The cross section for the process $\gamma^* p \to \rho^0 p$ is related to the ep cross section, for values of ε (equation 2.68) very close to unity, via

$$\sigma^{ep \to e\rho^0 p}_{Q2bin, Wbin} = \int_{Q^2 bin} \int_{Wbin} \varphi(Q^2, W) \sigma^{\gamma^* p \to \rho^0 p}(Q^2, W_{\gamma^* p}) dQ^2 dW_{\gamma^* p} \tag{9.18}$$

where φ, the effective photon flux, is given by (equation 2.31)

$$\varphi = \frac{\alpha}{2\pi} \frac{(1 + (1-y)^2)}{yQ^2} \tag{9.19}$$

The value of the cross section at a point $(W_{\gamma^* p\,0}, Q_0^2)$ was obtained in this analysis in the following way:

Let W_0 and Q_0^2 be such that the following equation is fulfilled:

$$\int_{Q^2 bin} \int_{Wbin} \varphi(Q^2, W_\gamma^* p) \sigma^{\gamma^* p \to \rho^0 p}(Q^2, W_{\gamma^* p}) dQ^2 dW_{\gamma^* p} = \varphi(Q_0^2, W_0) \sigma^{\gamma^* p \to \rho^0 p}(Q_0^2, W_0) \Delta Q^2 \Delta W_{\gamma^* p} \tag{9.20}$$

and ΔQ^2 and $\Delta W_{\gamma^* p}$ are the size of the bins used in the measurement.

Making the assumption that the $\gamma^* p$ cross section can be written as

$$\sigma^{\gamma^* p \to \rho^0 p}(Q^2, W_{\gamma^* p}) = \left(\frac{1}{1 + \frac{Q^2}{M_\rho^2}} \right)^2 W_{\gamma^* p}^\delta \tag{9.21}$$

and using, as the initial guess [3], n=2 and $\delta = 0.2$, the values of W_0 and Q_0^2 can be determined, and the γ^* cross section at that point extracted from equation 9.20. Once the cross section is determined at different values of Q^2 and $W_{\gamma^* p}$, its dependence on these variables can be fitted, and the results used in equation 9.21 in an iterative process.

In this analysis the ρ^0 production cross section has been determined for $|t| < 0.6$ GeV^2.

---

[3]These particular values are inspired by the VDM model and the results obtained by Donnachie and Landshoff, addressed in sections 2.5.2
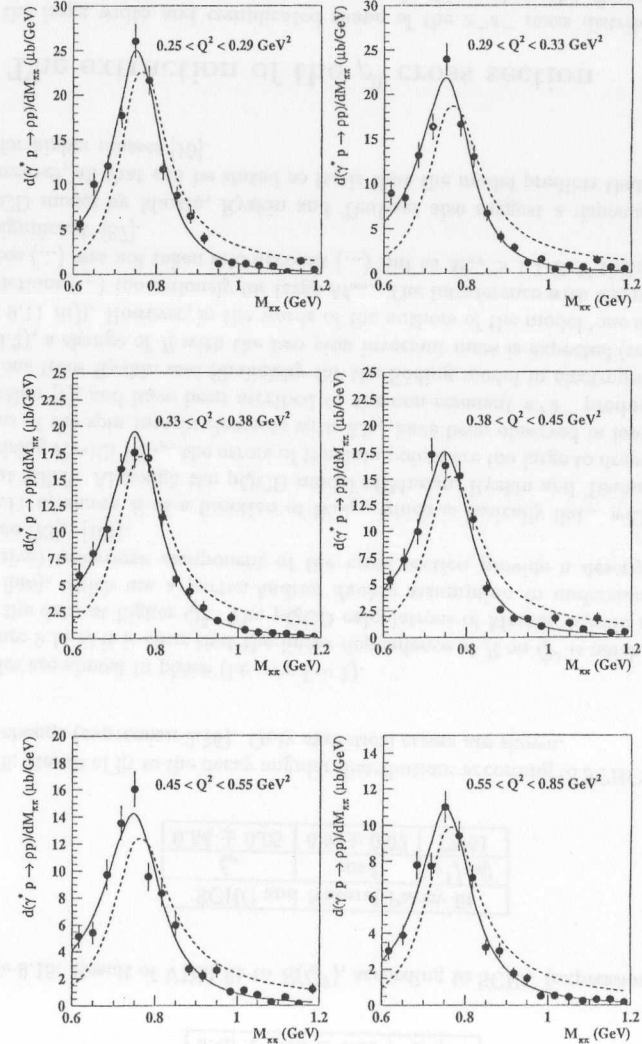
Figure 9.12: Mass distributions for cross section extraction (Q^2). (statistical errors only). The solid line is the result of the Söding fit, the dashed line is the corresponding Breit-Wigner function.

$W_{\gamma^* p}$ (GeV)	Q^2 (GeV)	events	W_0 (GeV)	Q_0^2 (GeV^2)	$\sigma^{ep \to e\rho^0 p}$ (nb)	$\sigma^{\gamma^* p \to \rho^0 p}$ (μb)
20-90	0.25-0.29	1074	51	0.27	4.99±0.15±0.47	5.07±0.15±0.48
	0.29-0.33	941		0.31	3.98±0.14±0.47	4.64±0.16±0.55
	0.33-0.38	857		0.35	3.88±0.13±0.33	4.14±0.14±0.36
	0.38-0.45	869		0.41	4.34±0.15±0.56	3.86±0.13±0.49
	0.45-0.55	784		0.50	4.55±0.16±0.49	3.41±0.12±0.37
	0.55-0.85	937		0.69	7.28±0.23±1.06	2.51±0.08±0.37

Table 9.17: Cross sections for different Q^2 values ($|t| < 0.6$ GeV^2). The ep cross section is given for the corresponding bin, the $\gamma^* p$ cross section is given at W_0 and Q_0^2.

9.4.1 The Q^2 dependence

The $d\sigma^{\gamma^* p \to \pi^+ \pi^- p}/dM_{\pi\pi}$ distributions in the Q^2 bins used to extract the ρ^0 cross section can be seen in figure 9.12.

The resulting cross sections (ep and $\gamma^* p$, using the extraction procedure described above) are listed in table 9.17 as a function of Q^2.

The Q^2 dependence of the ρ^0 cross section was parameterized according to the VDM prescription as

$$\sigma^{\gamma^* p \to \rho^0 p}(Q^2) = \sigma(0) \left(\frac{1 + \xi_\rho \frac{Q^2}{M_\rho^2}}{1 + \frac{Q^2}{M_\rho^2}} \right)^2 , \qquad (9.22)$$

where $\sigma(0)$ and ξ are the fit parameters. The result of this fit is given in table 9.18. The value of $\sigma(0)$ compares well to the ρ^0 photoproduction cross sections measured at HERA [114] [53] (ZEUS 94 result at $W_{\gamma^* p}$ 54.8 GeV: $10.90 \pm 0.21(\text{stat})^{+1.45}_{1.29}(\text{sys})\mu$b, H1 94 result: at $W_{\gamma^* p}$ 55.0 GeV: $9.1 \pm 0.9(\text{stat}) \pm 2.5(\text{sys})\mu$b, , but the extracted value of ξ_ρ is not compatible with that measured using the decay angular distributions described above. Such inconsistencies have been observed before and, furthermore, fits to equation 9.22 have, in some experiments, lead to unphysical results of ξ_ρ and, consequently, R [37]. It is believed [37] that, at high $W_{\gamma^* p}$ and low Q^2, ξ_ρ (and R) cannot be calculated from the above expression, and should be set to the value determined from the ρ^0 decay angular studies.

A VDM inspired alternative fit was performed:

$$\sigma^{\gamma^* p \to \rho^0 p}(Q^2) = \sigma(0) \left(\frac{1 + R(Q^2)}{1 + \frac{Q^2}{M_{eff}^2}} \right)^2 \qquad (9.23)$$

where $R(Q^2)$ follows expression 9.15, with ξ_ρ given in table 9.15 (from helicity analysis), and M_{eff} is a parameters of the fit (in the VDM picture, the virtual photon oscillates into hadrons, and it is not clear that the mass of the interacting state has to be that of a real ρ^0). The result of this fit is presented in table 9.19.

Another parameterization used to describe the dependence in Q^2 of the ρ^0 production was

Figure 9.13: Q^2 dependence of the elastic ρ^0 production cross section (statistical errors only). The solid line represents the result of a fit to expression 9.24, the dotted line, a fit to expression 9.23 and the dashed line a fit to 9.22.

$$\sigma^{\gamma^* p \to \rho^0 p}(Q^2) = \sigma(0) \left(\frac{1}{1 + \frac{Q^2}{M_\rho^2}} \right)^n \qquad (9.24)$$

yielding the results for $\sigma(0)$ and n shown in table 9.20.

Figure 9.13 shows the BPC cross section measurements with the results of the three fits described above superimposed. This picture is extended in Q^2 in figure 9.14, where other ρ^0 cross section measurements are shown. It can be seen that all the previous fits describe the BPC data, and extrapolate to values of the photoproduction cross sections that compare well with the measured ones. On the other hand, none of these cross section parameterizations can be extended to high Q^2, where they clearly overestimate the elastic ρ^0 production.

The summary of the error sources contributing to the systematic error on the cross section measurements, as well as in the parameter n which describes the cross section dependence according to equation 9.24 are presented in tables 9.23 and 9.24.

9.4.2 The $W_{\gamma^* p}$ dependence

The results of the cross section measurements in $W_{\gamma^* p}$ bins obtained from the mass fits shown in figure 9.15 are presented in table 9.21 and in figure 9.16.

VDM fit		
$\sigma(0)$ (μb)	ξ_ρ	χ^2/ndf
$9.97 \pm 0.48 \pm 0.92$	$0.16 \pm 0.07 \pm 0.19$	$1.4/4$

Table 9.18: Results of the fit of the Q^2 dependence of the cross section to equation 9.22.

Alternative VDM fit		
$\sigma(0)$ (μb)	$M_{eff}(GeV)$	χ^2/ndf
$10.97 \pm 1.33 \pm 1.77$	$0.66 \pm 0.05 \pm 0.10$	$1.6/4$

Table 9.19: Results of the fit of the Q^2 dependence of the cross section to equation 9.23.

Simplified fit		
$\sigma(0)$ (μb)	n	χ^2/ndf
$9.70 \pm 0.51 \pm 1.00$	$1.75 \pm 0.10 \pm 0.29$	$1.3/4$

Table 9.20: Results of the fit of the Q^2 dependence of the cross section to equation 9.24.

W_{γ^*p} (GeV)	Q^2 (GeV)	events	W_0 (GeV)	Q_0^2 (GeV²)	$\sigma^{ep \to e\rho^0 p}$ (nb)	$\sigma^{\gamma^*p \to \rho^0 p}$ (μb)
20-27	0.25-0.85	955	23	0.47	$5.52\pm0.18\pm0.64$	$3.16\pm0.10\pm0.37$
27-35		1024	31		$4.75\pm0.15\pm0.59$	$3.16\pm0.10\pm0.40$
35-45		994	40		$4.62\pm0.24\pm0.61$	$3.19\pm0.16\pm0.43$
45-55		897	50		$4.28\pm0.15\pm0.56$	$3.74\pm0.13\pm0.48$
55-70		1018	62		$4.89\pm0.15\pm0.50$	$3.61\pm0.11\pm0.38$
70-90		574	80		$4.72\pm0.20\pm0.56$	$3.44\pm0.14\pm0.40$

Table 9.21: Cross sections for different W_{γ^*p} values ($|t| < 0.6$ GeV²).

Figure 9.14: Q^2 dependence of the elastic ρ^0 production cross section over a wider Q^2 range. The error bars represent statistical and systematic errors added in quadrature. The overall normalization uncertainties are shown as shaded bands for the ZEUS data points. The solid line represents the extrapolation result of a fit of the BPC results to expression 9.24, the dotted line of a fit to expression 9.23 and the dashed line of a fit to 9.22. The BPC results are shown together with those of [114], [53] (photoproduction points indicated by an arrow), [56], [54] and results in preparation by the ZEUS collaboration.

Figure 9.15: Mass distribution for cross section extraction (W_{γ^*p}) (statistical errors only). The solid line is the result of the Söding fit, the dashed line is the corresponding Breit-Wigner function.
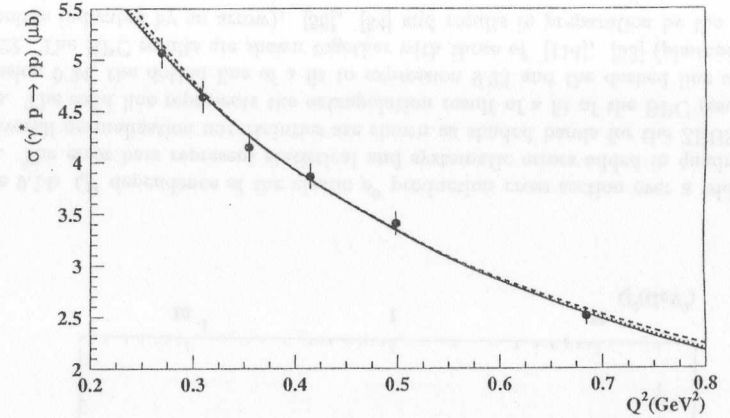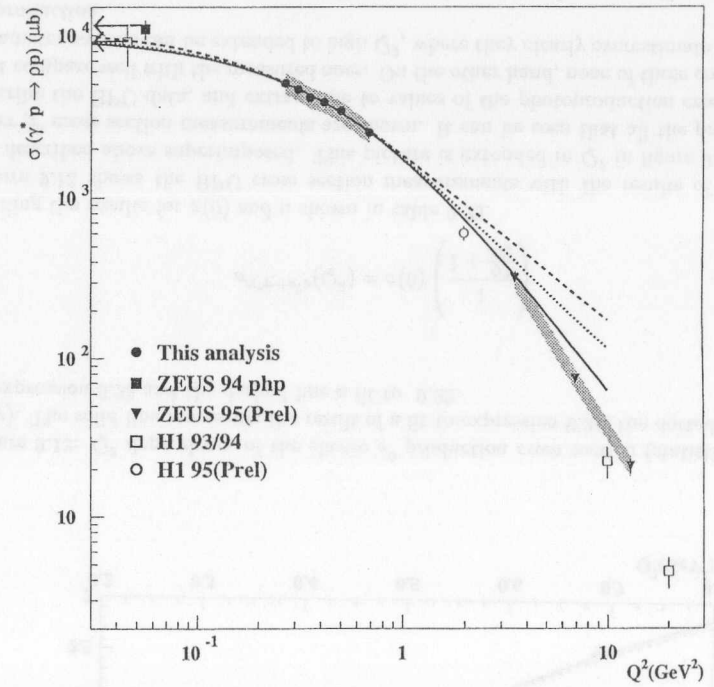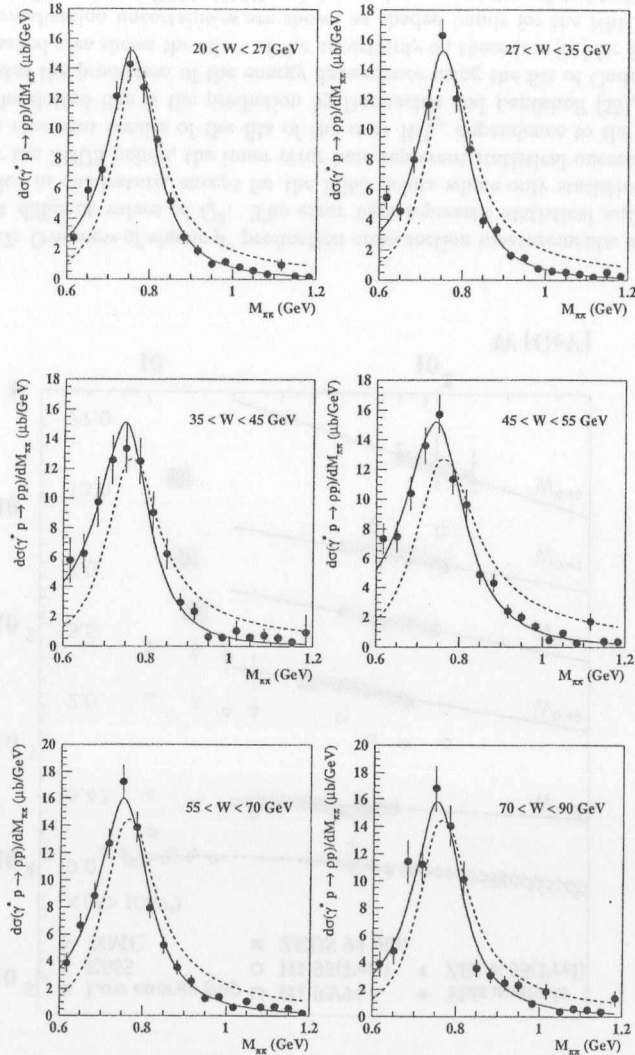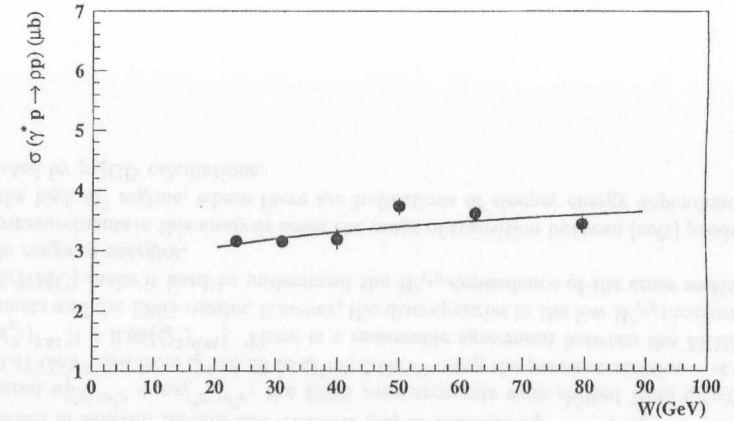

Figure 9.16: W_{γ^*p} dependence of the elastic ρ^0 production cross section (statistical errors only). The solid line represents the result of a fit to expression 9.25.

δ	χ^2/ndf
$0.12 \pm 0.03 \pm 0.08$	$9.2/4$

Table 9.22: Results of the fit of the W_{γ^*p} dependence of the cross section to equation 9.25.

These measurements have been fitted by an effective power dependence on the energy:

$$\sigma^{\gamma^*p \to \rho^0 p}(W_{\gamma^*p}) \propto W_{\gamma^*p}^\delta \qquad (9.25)$$

and the resulting exponent δ is given in table 9.22.

The cross section depends only weakly on the energy, as suggested in the framework of Regge phenomenology and VDM. For events which show a slope b of the t distribution shrinking with energy as $b = b_0 + 2\alpha' \ln(W_{\gamma^*p}^2/W_0^2)$, as discussed in the study of shrinkage in this analysis, the effective energy dependence of the cross section (after integrating over t) is found to be well described by $\delta \simeq 4(\alpha(0) - \alpha'/b - 1)$. Typical values of $b \sim 8$ GeV^{-2} lead to $\delta \sim 0.2$, in good agreement with the values determined in this analysis.

Figure 9.17 shows a compilation of results on ρ^0 production as a function of W_{γ^*p} over a wide range of energies and photon virtualities Q^2 (low energy photoproduction data from [78, 7, 79, 39]). The original H1 [53, 56, 54], E665 [37] and NMC [76] data points were moved in Q^2, when necessary, to coincide with the ZEUS values. The interpolation

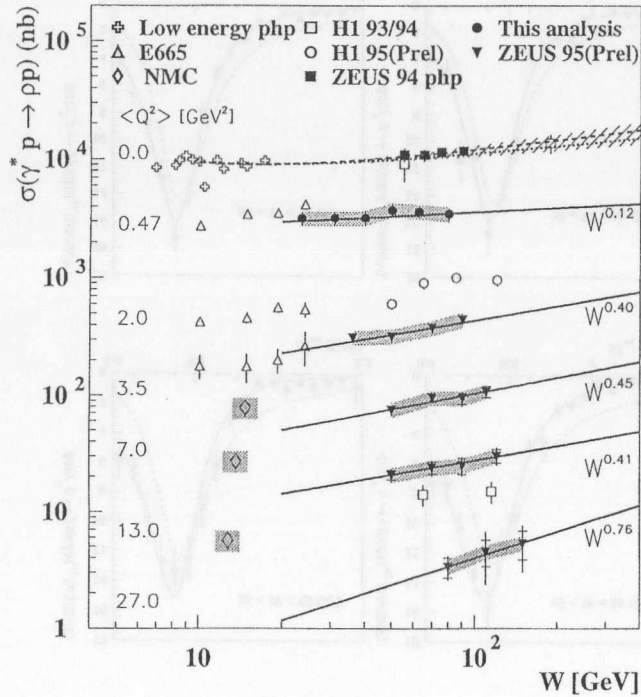Figure 9.17: Overview of elastic ρ^0 production cross section measurements. as a function of W_{γ^*p} at different values of Q^2. The error bars represent statistical and systematic errors added in quadrature, except for the E665 points where only statistical errors are given. For the ZEUS points, the inner error bars represent statistical uncertainties. The solid lines represent results of the fits of the $\sigma \propto W_{\gamma^*p}^\delta$ dependence to the ZEUS data points. The dotted line is the prediction by Donnachie and Landshoff [35], the dashed line indicates the prediction of the energy dependence using the fits of Cudell et al. [26] and the hashed area shows the effect of the uncertainty on these (see [51] for details). The overall normalization uncertainties are shown as shaded bands for the NMC and ZEUS data points. The original E665, NMC and data points were interpolated to the indicated Q^2 values (see text).

Error source	Typical uncertainty (%)	Comment
Tracking requirements	1-8	
BPC requirements	3-5	10% in lowest Q^2 bin
Matching	2-9	
Elastic MC parameterizations	$1 - 4$	
Extraction of ρ^0 signal	$0 - 4$	Nominal Söding parameterization
Extraction of ρ^0 signal	10	Other ρ^0 descriptions
Proton dissociative ρ^0	7	Normalization error
Elastic ω and ϕ production	1.6	Normalization error
Photon diffractive dissociation	3	Normalization error
Beam gas interactions	1.5	Normalization error
Trigger efficiency	5.5	Normalization error
Photon flux determination	1	Normalization error
Radiative corrections	2	Normalization error
Luminosity	1.1	Normalization error
Total uncertainty	9%-14% $\oplus$ 14% (norm)	

Table 9.23: Overview of the systematic uncertainties of the cross sections of bins in Q^2 and W_{γ^*p}, integrated over t ($|t| < 0.6$ GeV^2).

was done according to the Q^2 parameterizations of cross sections quoted for the respective datasets. The H1 points at Q^2=13 GeV^2 were obtained by moving from Q^2=10 GeV^2 and from Q^2=20 GeV^2, using the parameterization $\sigma \propto (1/Q^2)^{2.5}$, and taking a weighted average; the NMC points were moved from Q^2=6.9 to Q^2=7.0 GeV^2 and from Q^2=11.9 to Q^2=13 GeV^2 using the parameterization $\sigma \propto (1/Q^2)^{2.05}$ and R from the model of Martin, Ryskin and Teubner [73] to evaluate $\sigma_T^{\gamma^*p\to\rho^0 p} + \sigma_L^{\gamma^*p\to\rho^0 p}$ from the measured $\sigma_T^{\gamma^*p\to\rho^0 p} + \varepsilon\sigma_L^{\gamma^*p\to\rho^0 p}$; the E665 measurements were shifted from Q^2=0.61 to Q^2=0.47 GeV^2 and from Q^2=5.69 to Q^2=3.5 GeV^2 using the parameterization $\sigma \propto 1/(1 + Q^2/M_{\rho^0}^2)^{2.51}[1 + 0.66(Q^2)^{0.61}]$. There is a reasonable agreement between the ZEUS measurements and the E665 results, however, the discrepancies in the low W_{γ^*p} measurements (E665/NMC) make it hard to understand the W_{γ^*p} dependence of the cross section over a wide range of energies.

The measurements in this analysis cover the range of transition between (soft) production and the high Q^2 regime, where there are indications of steeper energy dependencies, as predicted by pQCD calculations.

Error source	Uncertainty in n	Uncertainty in δ
Tracking requirements	0.13	0.051
BPC requirements	0.22	0.005
Matching	0.10	0.057
Extraction of ρ^0 signal	0.07	0.019
Elastic MC parameterizations	0.06	0.030
Total uncertainty	0.29	0.084

Table 9.24: Overview of the systematic error on cross section parameterizations ($\sigma \propto 1/(1 + Q^2/M_\rho^2)^n$, $\sigma \propto W_{\gamma^*p}^\delta$).

Chapter 10

Conclusions

The elastic electroproduction of $\pi^+\pi^-$ pairs, $ep \to e\pi^+\pi^-p$ for $0.25 < Q^2 < 0.85$ GeV^2, $20 < W_{\gamma^*p} < 90$ GeV, $|t| < 0.6$ GeV^2, in the ρ^0 mass region $0.6 < M_{\pi\pi} < 1.2$ GeV, was studied for the first time at HERA.

For this study, a calorimeter was built and installed in ZEUS in the winter of 94/95. It has achieved a position resolution better than 1 mm for electron energies $E \gtrsim 10$ GeV, and an energy resolution $\sim \frac{17\%}{\sqrt{E}}$ GeV$^{-1/2}$ for electron scattered angles from 17 to 35 mrad. Its absolute energy scale and absolute position are know to 0.5% and 0.5 mm, respectively.

The observed $\pi^+\pi^-$ mass shape shows a deviation from the ρ^0 resonance shape given by a relativistic p-wave Breit-Wigner, and this distortion is well described by the Söding model, in terms of the interference between resonant and non-resonant $\pi^+\pi^-$ production. Together with photoproduction and high Q^2 measurements, these results confirm that the distortion of the mass shape decreases with Q^2.

The differential cross section $d\sigma^{\gamma^*p \to \pi^+\pi^-p}/d|t|$ distribution is well described by an exponential dependence $d\sigma^{\gamma^*p \to \pi^+\pi^-p}/d|t| \propto e^{-b|t|}$ for $|t| < 0.3$ GeV^2. There are indications that for higher $|t|$ values this distribution has a positive curvature. The parameters b measured here, combined with other ZEUS results, are consistent with a slight decrease of the diffractive slope with Q^2. There are indications of a decrease of b also with the two pion invariant mass. The measurements show some W_{γ^*p} dependence of the $|t|$ slope, which may be interpreted as shrinkage of the diffractive peak. The Pomeron trajectory obtained is consistent with that obtained by the Regge inspired fits performed by Donnachie and Landshoff to hadron-hadron data.

The values of the spin density matrix elements for $\pi^+\pi^-$ production in the ρ^0 mass region were measured under the assumption of s-channel helicity conservation. The results show consistency with this assumption, and also with that of natural parity exchange. The ratio of longitudinal and transverse cross sections, $R = \sigma_L^{\gamma^*p \to \rho^0 p}/\sigma_T^{\gamma^*p \to \rho^0 p}$, increases with Q^2. At low Q^2, R grows linearly with Q^2. It is known that the growth becomes less steep as the photon virtuality increases and can be well reproduced, for $Q^2 \gtrsim 3$ GeV, by the recent model of Martin, Ryskin and Teubner.

The cross section for the process $\gamma^* p \to \rho^0 p$ was studied in bins of Q^2 and $W_{\gamma^* p}$. The Q^2 dependence of this cross section can be described by VDM inspired parameterizations, as well as by the simplified parameterization $\sigma(Q^2) \propto 1/(1 + Q^2/M_\rho^2)^n$ with n=1.75±0.10(stat)±0.29(sys), However, a pure VDM approach results in inconsistencies with measurements from the $\pi^+ \pi^-$ helicity structure.

The $W_{\gamma^* p}$ dependence of the $\gamma^* p \to \rho^0 p$ cross section exhibits a slow rise with W at low values of Q^2, parameterized as $\sigma \propto W_{\gamma^* p \to \rho^0 p}^\delta$, with δ=0.12±0.03(stat)±0.08(syst) and consistent with the soft Pomeron picture.

The measurements show that ρ^0 production in the intermediate Q^2 range $0.25 < Q^2 < 0.85$ GeV^2 exhibits the features of a soft diffractive process, namely an exponential falloff of the cross section with t, s-channel helicity conservation, a weak energy dependence of the cross section and a Q^2 dependence similar to that predicted by VDM. These characteristics have also been observed in ρ^0 photoproduction at low $|t|$.

On the other hand, in comparison with the photoproduction and high Q^2 data, there are indications of the transitional character of this data set, such as the evolution with Q^2 of the $\pi^+\pi^-$ mass spectrum and of the slope b of the differential distribution $d\sigma^{\gamma^* p \to \pi^+ \pi^- p}/d|t|$.

The soft models that describe the BPC ρ^0 data, and which are consistent the measurements in photoproduction, cannot be extended far beyond the Q^2 of this analysis. The Q^2 dependence of the cross section in the BPC region is different from that observed at HERA at higher Q^2, and the data in the DIS regime indicate a steeper dependence of the cross section on $W_{\gamma^* p}$. Also the growth of R becomes less steep as the photon virtuality increases, and can be well reproduced by the pQCD model of Martin, Ryskin and Teubner.

This thesis has studied ρ^0 production in the regime of transition between the short distance QCD, where perturbative calculations are valid, and long distance QCD, which is as yet uncalculable. At this stage, the interpretation of this data can only be phenomenological. However, ultimately, the successful phenomenology of Regge and VDM is hoped to be interpreted in terms of QCD, the theory of strong interaction.

Appendix A

Online timing and vertex monitoring with the BPC

The Beam Pipe Calorimeter is used for the online determination of the electron-proton interaction vertex. This quantity is calculated using the different arrival times of background form the electron and the proton beam. In the present configuration of the ZEUS detector, the BPC is the only detector that can provide such information.

The data acquisition system used for this task is totally independent from the main ZEUS data acquisition system and is active during the injection of the beams, allowing feedback to the HERA operators, for the optimization of the useful luminosity.
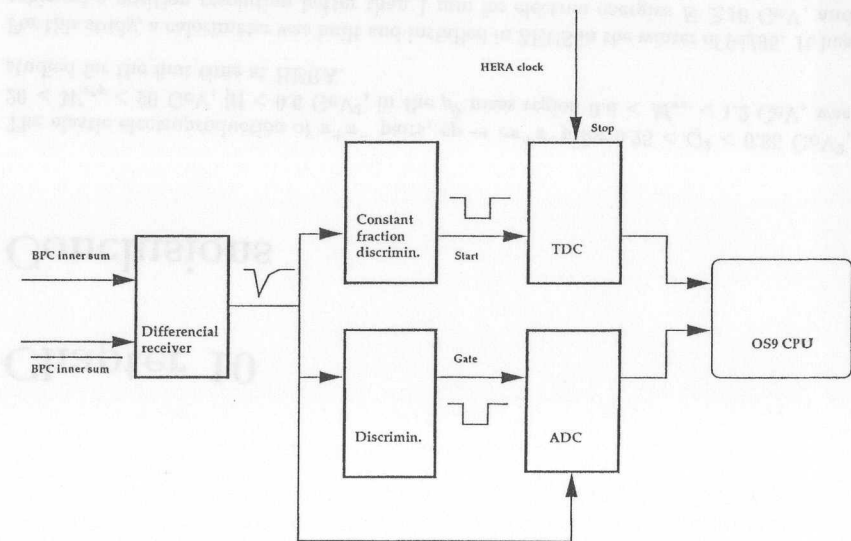

Figure A.1: Schematic view of the BPC online timing electronics.

Since the BPC modules are so close to the beam pipe they can be used to measure the rates and times, with respect to the HERA clock, of halo or spray particles in the proton and electron beams.

This information is obtained from the signal of the innermost vertical strips of the BPC (North or South Inner sum, as described in section 4.2.8), using CAMAC ADC (LeCroy 22249A) and TDC (LeCroy 2228A) modules, located in the *Rucksack*[1], as shown schematically in figure A.1.

The data acquisition is done by a VME-based OS9 system, and the TDC and ADC data are read and cleared approximately hundred times per second and stored as histograms. Some of available histograms are reset and read, automatically, at the beginning and end of each physics run, respectively, others can be cleared and retrieved at any given moment by the ZEUS shift crew.

Figure A.2 *i)* shows an example of the measured timing distribution of the electron (narrower peak) and proton (wider peak) beams with respect to the HERA clock. The histogram has been filled requiring a minimum pulse height of the signal, via a cut from the ADC measurement.

---

[1]Main electronics housing of the ZEUS detector, outside the limited access area of the detector.
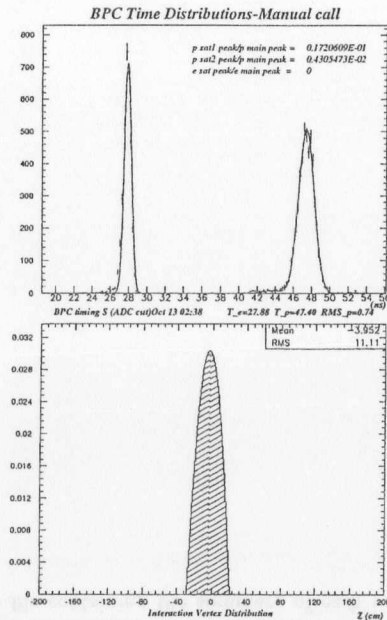

Figure A.2: BPC online timing and vertex distributions.

Due to the implementation of the *start* and *stop* inputs to the TDC, the proton peaks appears at later time values than the electron peak.

To extract the relevant information from the previous histogram, the electron timing distribution is fitted by a simple Gaussian function, while the proton one is fitted by a Gaussian function with a width corresponding to the sum, in quadrature, of the BPC timing resolution and the proton bunch length (the BPC timing resolution is ~ 0.5 ns, see section 5.4.3).

The distance between the two observed peaks is related to the Z coordinate of the interaction vertex through the equation

$$Z_{vtx} = \frac{(t_{proton} - t_{electron}) \times c}{2} + Z_0^{BPC} \qquad (A.1)$$

where Z_{vtx} is the interaction Z vertex, in the ZEUS coordinate system, t_{proton} and $t_{electron}$ are the mean proton and electron times resulting from the fits to the online timing distribution, c is the speed of light, and Z_0^{BPC} is the BPC position in ZEUS, in the Z direction (section 4.2.6).

The resulting vertex distribution for a particular run is shown in figure A.2 *ii)*. Studies of systematic errors have shown that the online vertex position cannot be determined to better than ~ 2 cm, corresponding to ~ 0.12 ns. The TDC has been calibrated using the vertex reconstructed offline, from the ZEUS Central Tracking Detector information, and the agreement of the two measurements is regularly checked.

This time measurement also gives information about the magnitude of the proton and electron satellite bunches, the beam particles separated from the main bunch by a distance corresponding to the radio frequency (RF) of the accelerating cavities. The electron satellite bunches differ from the primary electron bunch by multiples of 8 ns, corresponding to the 125 MHz frequency of the 450 MeV pre-accelerator PIA, while the proton satellite bunches are separated by ~ 5 ns, corresponding to a frequency of 208 MHz from the proton RF system.

The BPC online timing information allows the ZEUS shift crew to check:

- That the estimated Z position of the interaction is close to the origin of the ZEUS coordinate system (nominal interaction position), maximizing the detector acceptance.

- That the clock of the ZEUS trigger system is stable with respect to the HERA clock. Since both the BPC time and the trigger time are measured relative to the accelerator clock, shifts in the beam timing affect efficiency of the trigger timing cuts. The trigger time can be corrected for these relative shifts online.

- That the magnitude of any existing satellite bunch is small when compared to the primary bunch (The luminosity from satellite bunches cannot be resolved by the ZEUS luminosity monitor, so it is included in the integrated luminosity measurement. However, since these events are displaced in space and time, they have a different trigger efficiency and acceptance.).

Any anomalies are reported to the HERA operators.

The online electron and proton times, vertex and satellite bunch information is automatically appended to the file containing the summary of each run taken with the ZEUS detector.
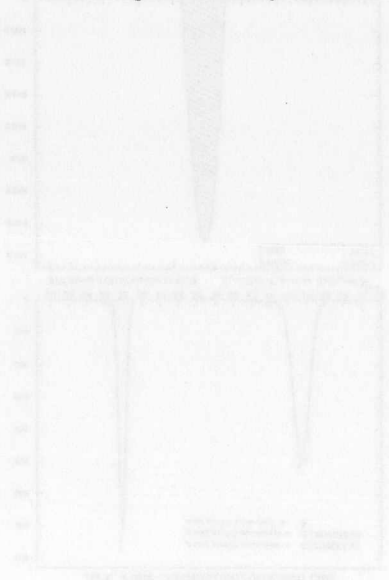
Appendix B

1995 BPC trigger configurations
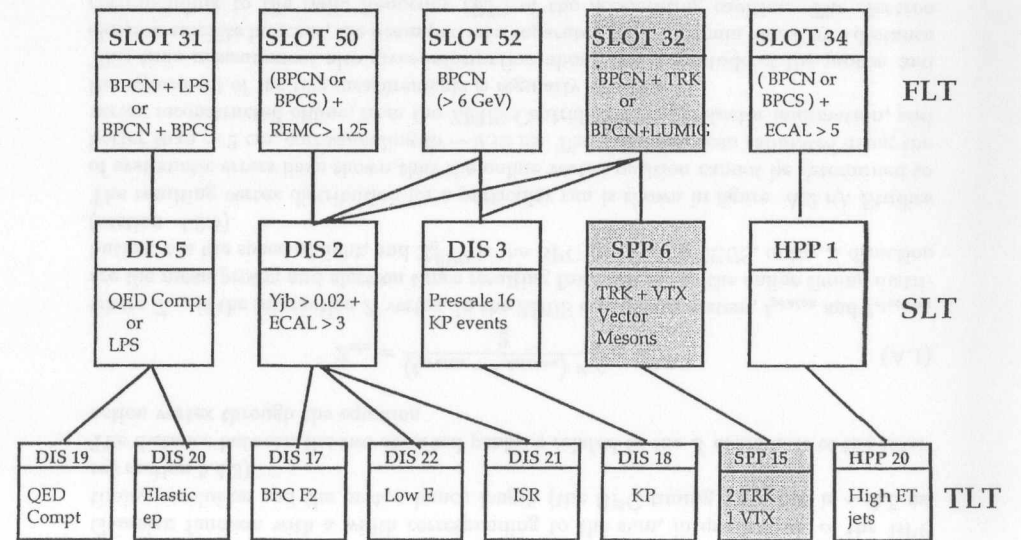
Figure B.1: 1995 trigger configurations using BPC.

SLOT 31	SLOT 50	SLOT 52	SLOT 32	SLOT 34	
BPCN + LPS or BPCN + BPCS	(BPCN or BPCS) + REMC> 1.25	BPCN (> 6 GeV)	BPCN + TRK or BPCN+LUMIG	(BPCN or BPCS) + ECAL > 5	**FLT**

DIS 5	DIS 2	DIS 3	SPP 6	HPP 1	
QED Compt or LPS	Yjb > 0.02 + ECAL > 3	Prescale 16 KP events	TRK + VTX Vector Mesons		**SLT**

DIS 19	DIS 20	DIS 17	DIS 22	DIS 21	DIS 18	SPP 15	HPP 20	
QED Compt	Elastic ep	BPC F2	Low E	ISR	KP	2 TRK 1 VTX	High ET jets	**TLT**

Bibliography

[1] G.A. Akopdjanov et al.: *Nucl. Inst. Meth.* 140 (1977) 441.

[2] C. Alvisi at al.: *Nucl. Inst. Meth.* A305 (1991) 30.

[3] U. Amaldi: *Physica Scripta* 23 (1981) 409.

[4] A. Andresen et al.: *Nucl. Inst. Meth.* A309 (1991) 101; A. Bernstein et al.: *Nucl. Inst. Meth.* A336 (1993) 23; M. Derrick et al.: *Nucl. Inst. Meth.* A309 (1991) 77.

[5] J. Andruszków et al.: DESY 92-066 (1992).

[6] T. Awes et al.: *Nucl. Inst. Meth.* A311 (1992) 130.

[7] J. Ballam et al.: *Phys. Rev.* D7 (1973) 3150.

[8] J. Bartels *et al.*: *Phys Lett.* B375 (1996) 301.

[9] T.H. Bauer, R.D. Spital, D.R. Yennie: *Rev. Mod. Phys.* 50 (1978) 261; Erratum ibid. 51 (1979) 407 and references therein.

[10] H. Beier: PhD. thesis, Univ. of Hamburg, DESY-F35D-97-06 (1997).

[11] H. Beier, A. Caldwell: ZEUS-Note 95-040 (Internal report, 1995); H. Beier: ZEUS-Note 96-107 (Internal report, 1996);

[12] M. Bengtsson, T. Sjöstrand: *Comp. Phys. Comm.* 39 (1986) 347; T. Sjöstrand, M. Bengtsson: *Comp. Phys. Comm.* 43 (1987) 367.

[13] H. Bethe, W. Heitler: *Proc. Roy. Soc.* A146 (1934) 83;

[14] B. Bock et al.: *Nucl. Inst. Meth.* A344 (1994) 335.

[15] G. Briskin: PhD. thesis in preparation, Univ. of Tel-Aviv.

[16] S.J. Brodsky et al.: *Phys. Rev.* D50 (1994) 3134.

[17] H. Brückmann et al.: DESY 87-064 (1987).

[18] CDF Collab., F. Abe et al: *Phys. Rev.* D50 (1994) 5535.

[19] CHIO collab., W.Shambroom et al.: *Phys. Rev.* D26 (1982) 1.

[20] A. Caldwell et at.: *Nucl. Inst. Meth.* A 321 (1992) 356.

[21] A. Caldwell et at.: ZEUS-Note 94-129 (Internal report, 1994).

[22] P.D.B. Collins: An introduction to Regge theory and high energy physics. Cambridge University Press, Cambridge (1977).

[23] P.D.B.Collins, A.D. Martin: Hadron interactions. Graduate student series in physics, Adam Hilger Ltd, Bristol (1984).

[24] J.A.Crittenden: Exclusive Production of Neutral Vector Mesons. Springer Tracts in Modern Physics, Volume 140 (Springer, Berlin, Heidelberg,1997)

[25] J.R. Cudell: *Nucl. Phys* B336 (1990) 1.

[26] J.R. Cudell et al.: HEP-PH/9601336 (1996); J.R. Cudell et al.: HEP-PH/9701312 (1997).

[27] A. Dannemann: PhD. thesis, Univ. of Hamburg (1996), DESY-F35D-96-06 (1996).

[28] K. Desler, U. Schneekloth: ZEUS-Note 95-061 (Internal report, 1995).

[29] K. Desler: How to use the PRT in 1995. <url: http://www-zeus.desy.de/ desler/PRT95.html> (April 29, 1997).

[30] DESY Annual report (1994).

[31] R.T. Deck: *Phys. Rev. Lett.* 13 (1964) 169.

[32] A. Donnachie, G. Shaw: Generalized Vector Dominance. Electromagnetic Interactions of Hadrons. (ed. by A. Donnachie and G. Shaw), Plenum Press, New York, 2 (1978).

[33] A.Donnachie, P.V. Landshoff: *Nucl. Phys.* B231 (1984) 189; A.Donnachie, P. Landshoff: *Nucl. Phys.* B267 (1986) 690.

[34] A. Donnachie, P.V. Landshoff: *Phys. Lett.* B185 (1987) 403; A. Donnachie, P.V. Landshoff: HEP-PH/9411368 (1994).

[35] A. Donnachie, P.V. Landshoff: *Phys. Lett.* B296 (1992) 227.

[36] S. Drell: *Phys. Rev. Lett.* 5 (1960) 278.

[37] E665 Collab., M.R. Adams et al.: *Z. Phys.* C74 (1997) 237.

[38] EMC Collab., J. Ashman et al.: *Z. Phys.* C39 (1988) 169.

[39] R.M. Egloff et al: Phys. Rev. Lett. 43 (1979) 657.

[40] C. Fabjan: CERN-EP/85-54 (1985).

[41] R. Fernow: Introduction to experimental particle physics. Cambridge University Press, Cambridge (1986).

[42] J.R. Forshaw, M.G. Ryskin.: *Z. Phys.* C68 (1995) 137.

[43] B. Foster et al.: *Nucl. Inst. Meth.* A 338 (1994) 254.

[44] L. Frankfurt, W. Koepf, M. Strikman: HEP-PH/9509311 (1995).

[45] C. Geich-Gimbel: *Int. Journal of Mod. Phys.* A 4 (1989) 1527.

[46] K. Goulianos: *Phys. Rep.* 101 (1983) 169.

[47] GEANT: detector description and simulation tool. CERN Program Library Long Writeup W5013 (1994).

[48] F.J. Gilman: *Phy. Rev.* 167 (1968) 1365.

[49] M. Gospic, H. Groenstege: ETR 94-11 (NIKHEF department of electronic technology).

[50] M. Groll: Diploma thesis, Univ. of Hamburg, DESY-THESIS-1998-008 (1998).

[51] J.Grosse-Knetter: PhD. thesis, Univ. of Hamburg, DESY-F35D-97-02 (1997).

[52] H1 Collab., S.Aid et al.: *Phys. Lett.* B338 (1994) 507.

[53] H1 Collab., S.Aid et al.: *Nucl. Phys.* B463 (1996) 3.

[54] H1 Collab., S.Aid et al.: *Nucl. Phys.* B468 (1996) 3.

[55] H1 Collab., S.Aid et al.: *Nucl. Phys.* B472 (1996) 3.

[56] H1 Collab., S.Aid et al.: Elastic electroproduction of ρ and Φ mesons for $1 < Q^2 < 5$ GeV^2 at HERA; Paper submitted to the *29th International Conference on High Energy Physics, Jerusalem, Israel* (1997).

[57] H1 Collab., C. Adloff et al.: *Z.Phys.* C75 (1997) 607.

[58] L.N. Hand: *Phy. Rev.* 129 (1963) 1834.

[59] G.F. Hartner et al.: ZEUS-Note 95-004 (Internal report, 1995).

[60] M. van der Horst: PhD. thesis, Univ. of Amsterdam (1990).

[61] M. Inuzuka: Diploma thesis, Univ. of Tokyo (1996).

[62] C. Itzykson, J.B.Zuber: Quantum field theory. International series in pure and applied physics, McGraw-Hill, (1980).

[63] F. Jacquet, A. Blondel: Proceedings of the study of an *ep* facility for Europe. DESY 79-48 (1979) 391.

[64] P. Joos et al.: *Nucl. Phys.* B113 (1976) 53.

[65] M. Kasprzak: PhD. thesis, Univ. of Warsaw, DESY-F35D-96-16 (1996).

[66] B. Krebs: PhD. thesis, Univ. of Hamburg (1992), DESY-F35D-92-03 (1992).

[67] A. Kwiatkowski, H. Spiesberger, H.J. Moehring: Proceedings of the workshop on physics at HERA. (ed. by W. Buchmüller and G. Ingelmann) DESY Hamburg 1991, 1294.

[68] Landholt-Börnstein handbook: Total Cross-Sections for Reactions of High Energy Physics. New Series, 12B (1987).

[69] P.V. Landshoff, O. Nachtmann: *Z. Phys* C35 (1987) 405.

[70] D.W.G.S. Leith: High-Energy photoproduction: Diffractive Processes. Electromagnetic Interactions of Hadrons. (ed. by A. Donnachie and G. Shaw), Plenum Press, New York, 1 (1978) 345.

[71] E. Lohrmann, K. Desler: private communication.

[72] G. Marchesini et al: *Comp. Phys. Comm.* 67 (1992) 465;
B. R. Webber: Proceedings of the workshop on physics at HERA. (ed. by W. Buchmüller and G. Ingelmann) DESY Hamburg 1991, 1354;
L. Stanco, ibid., 1363.

[73] A.D. Martin, M.G.Ryskin, T. Teubner: *Phys. Rev.* D55 (1997) 4329.

[74] MINUIT: Function minimization and error analysis. Program Library Long Writeup D506 (1992).

[75] K. Muchorowski: ZEUS-Note 97-014 (Internal report, 1997);
K. Muchorowski: PhD. thesis, Univ. of Warsaw (1998).

[76] NMC Collab., M.Arneodo et al.: *Nucl. Phys.* B429 (1994) 503.

[77] W.R. Nelson, H. Hirayama, D.W. Rogers: The EGS4 Code System. SLAC-265 (1985)

[78] OMEGA Collab., D. Aston et al. *Nucl. Phys.* B209 (1982) 56.

[79] J. Park et al.: *Nucl. Phys.* B36 (1972) 404.

[80] Particle data group: Review of Particle Physics. *Phys. Rev.* D50 (1994).

[81] D.H. Perkins: Introduction to high energy physics. 2nd ed., Addison-Wesley, (1982).

[82] A. Quadt: PhD. thesis, Univ. of Oxford (1997), DESY-THESIS-1998-007 (1998).

[83] A. Quadt, O. Ruske: The Vertex Distribution Page.
<url: http://www-zeus.desy.de/ ruske/ZEUS_ONLY/fsigma/tools/vtxweight/vtxweight.html>
(February 20, 1998).

[84] S. Ritz: private communication.

[85] M. Ross, L. Stodolsky: *Phys. Rev.* 149 (1966) 1172.

[86] M.G. Ryskin: *Z. Phys* C57 (1993) 89; M.G. Ryskin et al.: HEP-PH/9511228(1995)

[87] M.G. Ryskin, Yu.M. Shableski: HEP-PH 9701407 (1997);
    M.G. Ryskin, Yu.M. Shableski: HEP-PH 9704279 (1997).

[88] J.J. Sakurai: *Ann. Phys.* 11 (1960) 1.

[89] J.J. Sakurai: *Phys. Rev. Lett.* 22 (1969) 981.

[90] K. Schilling, G. Wolf: *Nucl. Phys.* B61 (1973) 381.

[91] G.A. Schuler, T. Sjöstrand: *Nucl. Phys.* B407 (1993) 539

[92] T. Sjöstrand: *Z. Phys.* C42 (1989) 301.

[93] P. Söding: *Phys. Lett.* 19 (1966) 702.

[94] A.A. Sokolov, I.N. Ternov: *Soviet Physics Doklady* 12 (1964) 1203.

[95] R. Spital, D.R. Yennie: *Phys. Rev.* D9 (1974) 126.

[96] B. Surrow: PhD. thesis, Univ. of Hamburg, DESY-THESIS-1998-004 (1998).

[97] J. Tickner: PhD. thesis, Univ. of Oxford (1997).

[98] S. Wang: ZEUS-Note 96-121 (Internal report, 1996).

[99] D. Westphal: PhD. thesis, Univ. of Hamburg, DESY-F35D-97-11 (1997).

[100] D. Westphal: Diploma thesis, Univ. of Hamburg, DESY-F35D-93-04 (1993).

[101] G. Wolf: HERA: physics, machine and experiments. Lectures given at *Advanced study
    inst. on techniques and concepts of High Energy Physics*, St. Croix, Virgin Islands, Jun
    19-30 1986 DESY 86-089 (1986).

[102] D.R. Yennie: The hadronic properties of the photon. Cargèse lectures on physics (ed. by
    M.Levy) 7 (1972) 331.

[103] ZEUS Collab.: The ZEUS detector: Status report, Hamburg, February 1993.

[104] ZEUS Collab., M.Derrick et al.: *Phys. Lett.* B 350 (1995) 120.

[105] ZEUS Collab., M.Derrick et al.: *Phys. Lett* B356 (1995) 601.

[106] ZEUS Collab., M.Derrick et al.: *Z. Phys.* C69 (1995) 39.

[107] ZEUS Collab., M.Derrick et al. *Phys. Lett.* B 377 (1996) 259.

[108] ZEUS Collab., M.Derrick et al.: *Phys. Lett.* B380 (1996) 220.

[109] ZEUS Collab., M.Derrick et al.: *Z. Phys.* C73 (1996) 73.

[110] ZEUS Collab., J.Breitweg et al.: *Z. Phy.* C75 (1997) 215.

[111] ZEUS Collab., J. Breitweg et al.: Study of vector meson production at large | t | at HERA;
    Paper submitted to the *29th International Conference on High Energy Physics, Jerusalem,
    Israel* (1997).

[112] ZEUS Collab., J. Breitweg et al.: Exclusive vector meson production in deep inelastic
    scattering at HERA; Paper submitted to the *29th International Conference on High Energy
    Physics, Jerusalem, Israel* (1997).

[113] ZEUS Collab., J.Breitweg et al.: *Phys. Lett.* B 407 (1997) 432.

[114] ZEUS Collab, J.Breitweg et al.: *Europ. Phys. Jour.* C2 (1998) 247.

[115] G. Zech: DESY 95-113 (1995).

Acknowledgments

Working within the ZEUS collaboration at DESY, among colleagues from all over the world, has been a wonderful and fulfilling experience, both professionally and personally. The friendly and yet challenging environment made my stay in Hamburg very pleasant and contributed to the success of this work.

I want to express my gratitude to Prof. Erich Lohrmann who was the first to encourage me to join the ZEUS collaboration, and from whose advise I have greatly profited, especially during the editorial process of our paper. Not only do I admire his insight in physics, but also the way he interacts with his colleagues and students.

I want to thank my supervisor, Prof. Robert Klanner, for all his guidance, support and wisdom. Furthermore, I would like to thank him for all the trust he placed in my work (even at moments when I wasn't sure I deserved it), for the contagious enthusiasm he radiates, and for his sense of humor, which made me enjoy our working relationship so much.

Working within the BPC group was always a pleasure. With the help of Qiang Zhu, Uli Kötz, Bernd Surrow (my fellow slave of the BPC), Jan Hauschildt, James Tickner, Masahide Inuzuka, Dorian Kcira, Ulli Fricke and Antonio Pellegrino, to name a few, our little detector was born, and is now a top performer in ZEUS.

The help of Johnny Ng, Dave Gilkinson and Chris Youngman in setting up hardware and software was crucial during my first days at DESY.

Sasha Proskuryakov introduced me to vector mesons and to the analysis techniques, and has since been a patient listener to all my doubts. I have learned a lot from him, and would like to give him a very special thank you. Michele Arneodo, I thank not only for the frank and enlightening discussions we had but also for his days as a coordinator of the Soft Photoproduction/Diffractive working group. This thanks extends also to Elisabetta Gallo and Halina Abramowicz, and to Krzysztof Piotrzkowski, whose dedication to vector mesons is inspiring.

I profited from many lively discussions with other members of the vector meson crew, including Jörn Grosse-Knetter, Heiko Beier, Laura Ianotti, Songming Wang, Marcus Groll and especially Jim Crittenden and Dirk Westphal, two of my biggest right-to-the-point critics.

In addition, during my PhD and, in particular, during the preparation of both the vector meson paper and this thesis, I have learned a great deal from Allen Caldwell, Tony Doyle and Aharon Levy.

Many of the above have also contributed to ease the long working days at DESY, as have the Hamburg students, in particular Martin Löwe (thank you, Martin), Olaf Deppe, Kirstin Hebbel, Marguerita Milite, Michael Sievers, Florian Goebel, and Kai Desler.

It was a wonder that my social life did never collapse, and that was due to the company of, among others, Wouter Verkerke (by now an old friend), Aldus Whitfield, Jon Labs, Doug Hasell, Cathy Farrow, Tony Vaiciulis, Richard Cross, Alex Prinias, Katerina Tzamariudaki, Yorgos Tsipolitis, Pat Saull, Laurel Sinclair and Stefan Schlenstedt, who also helped me with the German version of my abstract.

I want to acknowledge the financial support I have received from the Portuguese *Fundação para a Ciência e Tecnologia (Sub-Programa Ciência e Tecnologia do 2° Quadro Comunitário de Apoio)* throughout my PhD work, and the opportunities I was given by the DESY directorate to participate in scientific schools and conferences during this period. My interest for High Energy Physics would not have grown had I not been given the opportunity to join the LIP-Lisbon group as an undergraduate student. I want to thank all the members and friends of the lab, who played an important role in my education, in particular José Mariano Gago, Paula Bordalo, Peter Sonderegger, João Varela, Sérgio Ramos, Conceição Abreu, Mário Pimenta, Amélia Maio and Gaspar Barreira.

Last, but not least, I have to thank Rik Yoshida, who has done a little of all the things listed above. But more important than that, he has made me smile all along the way.

Esta tese não é só minha: é também da Ana, do Josué... e da Dona Lucinda!

174

175